Reviews in Mineralogy & Geochemistry
Vol. 60, pp. 519-596, 2006

Cratering History and Lunar Chronology

Dieter Stöffler
Institut für Mineralogie, Museum für Naturkunde
Humboldt Universität zu Berlin
Invalidenstrasse 43, 10099 Berlin, Germany
e-mail: Dieter.Stoeffler@MUSEUM.HU-Berlin.de

Graham Ryder
Lunar and Planetary Institute
3600 Bay Area Blvd., Houston, Texas 77058, U.S.A.

Boris A. Ivanov and Natalia A. Artemieva
Institute for Dynamics of Geospheres
Leninsky Prospect, 38, Bldg. 1, 119334 Moscow, Russia

Mark J. Cintala
NASA Johnson Space Center
SN2, Houston, Texas, 77058, U.S.A.

Richard A. F. Grieve
Natural Resources Canada
588 Booth Street, Ottawa, Ontario, K1A 0Y7, Canada

1. INTRODUCTION

The Moon is exceptional and important because it is the only planetary body besides the Earth for which we have both a detailed stratigraphic history and datable rock samples that can be related to specific geomorphologic units (Fig. 5.1). The Moon has preserved much of its magmatic and impact record of at least the last 4 billion years. While its endogenic history is of great interest for the fundamentals of planetary interiors and surfaces, the Moon has become a calibration plate for the cratering record of the Earth-Moon system, and by extrapolation, of the entire inner solar system if one assumes a heliocentric origin for impactor populations. These populations range from asteroids through long and short period comets to interplanetary dust, and cover a size range from hundreds of kilometers to micrometers.

This chapter reviews the presently available data sets in support of this paradigmatic assumption, as follows: (1) the phenomenology of lunar impact craters, (2) the terrestrial record of the impact cratering process and the interpretation of terrestrial impactites as far as this "ground truth" is relevant for the interpretation of lunar impact craters and datable lunar impact breccias and melt rocks, (3) the theory and numerical simulation of the cratering process and the characteristics of the Earth-Moon crossing population of impactors (asteroids and comets), (4) the principles of relative age dating of lunar surface units and the general lunar stratigraphy, (5) the stratigraphic significance and ages of lunar samples (impactites and basalts) and, based on this data set, the absolute ages of lunar surface units, (6) the cratering rate of the Moon as a function of time, and (7) the time calibration of this cratering rate based on the most recent data for the ages of multiring basins, mare basalt surfaces, and post-

1529-6466/06/0060-0005$10.00 DOI: 10.2138/rmg.2006.60.05

Figure 5.1. Telescopic view of the nearside of the Earth's Moon with landing sites of the Apollo and Luna missions.

Eratosthenian impact craters such as Copernicus, Tycho, North Ray, Cone, and South Ray. The present state of the art confirms the concept of an early heavy bombardment of the Moon before about 3.7 Ga and a more or less constant cratering flux since then, which is compatible with the relatively restricted terrestrial cratering record and with astronomical observations. It does, however, not allow firm conclusions about the existence of a terminal lunar cataclysm. In fact, there are serious but not yet final arguments against this concept. A major obstacle to solve this question is the lack of absolute ages for heavily cratered highland regions older than about 4 Ga. Future sample return missions are required to clarify this issue, which is fundamental to understanding the collisional history of the inner solar system.

2. THE IMPACT CRATERING PROCESS: OBSERVATION AND MODELING

2.1. Morphology and morphometry of lunar impact craters

2.1.1. Morphology. Lunar impact craters exhibit a spectrum of size-dependent morphologies (e.g., Smith and Sanchez 1973; Howard 1974; Head 1976; Schultz 1976; Wilhelms et al. 1987). The basic morphologic subdivisions of lunar impact craters with increasing rim diameter are (1) simple craters, (2) complex craters, and (3) impact basins. As there can be variations in morphology even within restricted size ranges (e.g., Smith and Sanchez 1973; Howard 1974, Cintala et al. 1977), it can be difficult to choose a "typical" member of a given size class of lunar craters. A detailed discussion and classification of lunar crater morphologies can be found in Schultz (1976).

Simple craters. The classic "bowl shape" of a simple crater is typified by the 10 km diameter (D) crater Alfraganus C (Fig. 5.2). Fresh bowl-shaped craters are actually trapezoidal

in profile, with walls possessing nearly constant slopes and small, essentially flat floors (Ravine and Grieve 1986). Wall failure is generally limited to small units commonly associated with the floor hummocks and to scree emplaced after solidification of the thin impact melt deposits on the crater floor. Hummocks and blocks are common on the floors of these craters, but central peaks do not emerge until diameters >10 km (Smith and Sanchez 1973; Howard 1974; Head 1976).

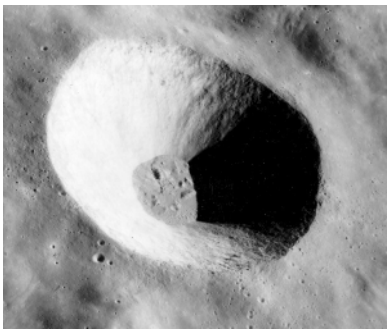

Figure 5.2. Alfraganus C (10 km in diameter) in the lunar central highlands. This crater is representative of the class of lunar simple craters, which are characterized by smooth walls, relatively flat floors, and large depth/diameter ratios. This view is to the north-east (portion of Apollo 16 Panoramic Camera Frame 4615).

Complex craters. Complex craters are highly modified with respect to simple crater morphology. When viewed in the context of the full spectrum of crater morphologies, the transition from simple to complex craters is abrupt (e.g., Pike 1974). Inspection of the individual transitional craters, however, reveals that the changes in morphology are more gradual and less than systematic (e.g., Smith and Sanchez 1973; Howard 1974; Head 1976). For example, Lalande (D = 25 km) displays features that are similar to those in the smaller, simple craters, but also includes precursors of structures and units that are better developed in complex craters. Portions of Lalande's wall show only minor evidence of slumping. Overall, however, Lalande exhibits scalloped walls that begin to exhibit the complexity of the more intricately terraced complex craters. Its central peaks, on the other hand, are only emerging from the floor and are not the major topographic features that are characteristic of larger complex craters. Floor hummocks are more imposing and widespread than those in the simple craters.

Uplift of the crater floor and wall failure are well established in craters the size of Tycho (D = 85 km, Fig. 5.3). Terraced walls in the rim area are the rule, as are abundant floor hummocks. A crater of Tycho's size, or larger, typically exhibits a massive central peak or a cluster of peaks (Hale and Head 1979). The relative heights and volumes (Hale and Head 1979; Pike 1980a,b; Hale and Grieve 1982) of these peaks increase as a function of size until diameters of ~80 km, after which both values begin to decrease. Roughly simultaneous with this change, a ring of roughening on the floor, composed of hummocks arranged quasi-concentrically with the central structure, begins to appear (Croft 1981a,b; Hale and Grieve 1982). This represents the transition to impact *basins*.

Peak-ring basins. Central-peak basins, such as Compton (D = 75 km) are relatively small basins with a fragmentary ring of peaks surrounding a central peak. They are transitional to peak-ring basins. Peak-ring basins, which have a well-developed ring but lack a central peak, are found in the 175–450 km size range.

Relatively undegraded peak-ring basins on the Moon are rare, with the freshest example being the 320 km Schrödinger basin (Fig. 5.4). The interpretation of the interior morphologies of such basins is usually complicated by impact erosion, subsequent volcanic activity, or both. Nevertheless, the relevant observations can be made by inspecting a number of examples (Wilhelms et al. 1987). Additional descriptions of Schrödinger can be found in Hartmann and Wood (1971), Schultz (1976), and Spudis (1993).

Peak-ring basins are relatively shallow features for their size. Although their depths can be decreased by erosion or infilling, the fact that details of many interior features are visible (e.g., the peak ring and floor hummocks in Schrödinger) indicates that the relative shallowness is a

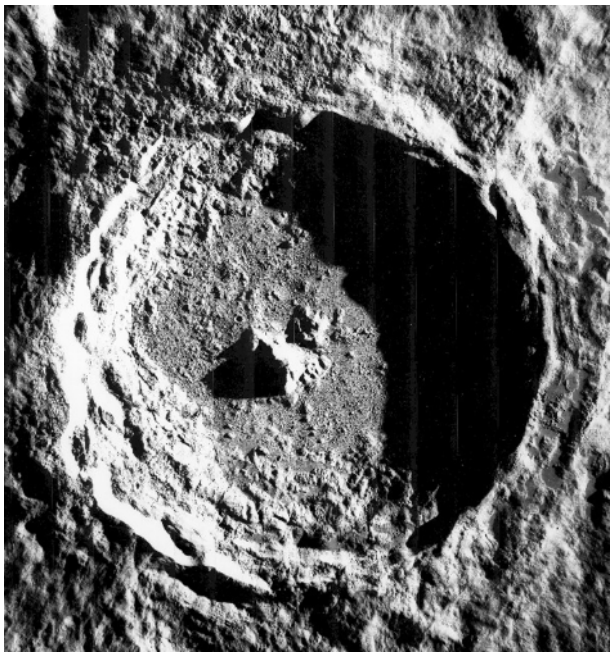

Figure 5.3. Tycho (85 km in diameter) in the southern lunar highlands. This is a classic complex lunar crater, with central-peak cluster, extensive wall terracing. North is toward the top of the frame (Lunar Orbiter V 125M).

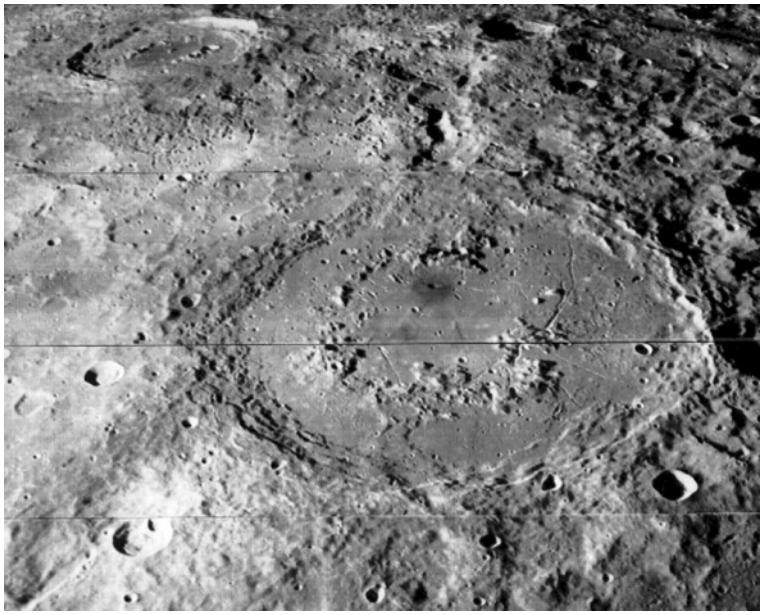

Figure 5.4. The peak-ring basin Schrödinger (320 km in diameter) near the lunar south pole. Note the fractured floor and the dark-haloed volcanic vent inside the peak ring, which indicates that even this relatively fresh basin has undergone some modification from a variety of sources. This view is to the east-southeast. Antoniadi (140 km in diameter) is the peak-ring basin with the small central peak near the top left corner of the frame (Lunar Orbiter IV 9M).

primary characteristic. Wall terraces in the rim area are highly developed, and the ratio of floor diameter to rim-crest diameter is somewhat greater than in complex craters (Pike 1980a).

Multiring basins. The largest basins are multiring basins. Some researchers find as many as six concentric rings in the largest basins (e.g., Spudis 1993). Multiring basins are generally more than 400 km in diameter. The best example is the Orientale Basin, which has been only partly flooded by post-impact lavas. The definition of diameters for the various basin features varies among workers, depending on the exact criteria and data sets examined. A comprehensive treatment of lunar multiring basins can be found in Spudis (1993), which is also an excellent source of the primary literature on multiring basins. Wieczorek and Phillips (1999) pointed out that the definition of the crater diameter of multiring basins in the older literature (Wilhelms et al. 1987; Spudis 1993) is problematic and should no longer be used. The definition of the final "rim to rim" diameter of a multiring basins is difficult and continues to be a matter of dispute. Wieczorek and Phillips (1999) argue for smaller diameters than previously proposed. Their geophysical modeling demonstrates how gravity-field anomalies measured from satellites may help to improve the interpretation of multiple rings.

The most complete classification of lunar crater shapes is that of Wood and Andersson (1978), which is based on observations from Lunar Orbiter IV photographs and provides a compilation of morphologic and morphometric data for 11,462 craters. Crater shape classification is more detailed than that outlined above, and 18 different crater types are recognized. Some, however, represent rare variants. Disagreement exists as to whether all observable crater forms represent distinct morphologic types, whether some forms are transitional stages or erosional states between accepted end members (Ravine and Grieve 1986), or whether some forms are the result of effects of varying target properties on crater shape (Cintala et al. 1977).

The catalog of Wood and Andersson (1978) also includes criteria for the classification of progressively eroded and degraded impact structures. Estimates of "degradation" (extent of erosion) are based on such features as rim continuity, rim sharpness, and infilling of the crater cavity by mass wasting. Class 1 craters are the freshest and least eroded; class 5 craters are the most degraded and are only marginally recognizable as impact features. Degradational state becomes important when evaluating the relative formation ages of specific craters or crater populations (Soderblom 1970; Wilhelms 1984; Wilhelms et al. 1987; see discussion in Section 4).

2.1.2. Morphometry. Morphometry describes the fundamental diameter-dependent variations in crater topographic features, such as the statistical variation of crater depth with rim diameter. Detailed measurements of lunar imagery have made it possible to represent the different geometrical characteristics of lunar impact craters by equations of a power law form:

$$y = aD^b \tag{5.1}$$

where y is a given crater characteristic (e.g., depth, rim height), D is the diameter of the crater (measured from rim to rim), and a and b are constants. Specific morphometric relations for what are considered fresh lunar craters are summarized in Table 5.1. It should be noted that the definition of the rim diameter for multiring basins is still an unsolved problem and there is an ongoing debate on this issue (e.g., Wieczorek and Phillips 1999).

2.2. Terrestrial impact structures

2.2.1. Structural characteristics and comparison with lunar impact craters. As exemplified above, impact craters on the Moon are recognized by their characteristic morphology. The terrestrial record of impacts, however, has been severely modified by active geologic processes and most recognized terrestrial impact craters are far from pristine in appearance. In this regard, they are better referred to as impact structures as opposed to impact craters, which implies a specific morphology. Nevertheless, terrestrial impact structures provide the major observational

Table 5.1. Morphometric relations for fresh lunar impact craters.

Crater Characteristic	*D**, km	*N*	Exponent (*b*)	Coefficient (*a*)	Source
Simple Craterforms					
Depth	<15	171	1.010	0.196	(1)
Rim height	<15	124	1.014	0.036	(2)
Rim diameter	<15	117	1.011	0.257	(2)
Floor diameter	<20	38	1.765	0.031	(2)
Interior volume	<13	47	3.00	0.040	(3)
Complex Craterforms					
Depth	12-275	33	0.301	1.044	(1)
Rim height	15-375	38	0.399	0.236	(2)
Rim diameter	15-375	46	0.836	0.467	(2)
Floor diameter	20-125	53	1.249	0.187	(2)
Diameter (central peak)	17-175	175	1.05	0.016	(4)
Basal area central peak	17-136	19	2.19	0.09	(5)
Height central peak	17-51	15	1.969	0.589×10^{-3}	(5)
Central peak volume	17-51	15	5.078	0.987×10^{-7}	(5)
Central peak volume	80-136	4	3.599	0.387×10^{-5}	(5)
Interior volume	19-150	21	2.31	0.238	(3)
*Basins***					
Diameter ring in central peak and peak ring basins	140-435	12	1.125	0.245	(6)
Diameter inner ring in multi-ring basins	420-1160	13	0.943	0.708	(7)
Diameter intermediate ring in multi-ring basins	420-1160	13	0.970	0.845	(7)
Depth	200-630	7	0.15	2.03	(8)***

Notes: *Range of rim diameter values (*D*) used to establish relations for other topographic features. N is the number of craters. Volumes (central peaks, crater interiors, etc.) are in km^3 (from Heiken et al. 1991). ** Note that the "rim to rim diameter" of multi-ring basins is controversial as pointed out by Wieczorek and Phillips (1999) who propose smaller values. ***Power law in Pike's form. Original fit by Williams and Zuber (1998) is given as: $\log_{10}(\text{depth})=0.41*[\log_{10}(D)]^{0.57}$

Sources: (1) Pike 1974; (2) Pike 1977a; (3) Croft 1978; (4) Hale and Head 1979; (5) Hale and Grieve 1982; (6) Head 1977; (7) Pike and Spudis 1987; (8) Williams and Zuber 1998

constraints of the characteristics of natural impact craters, particularly with respect to the third dimension, i.e., subsurface characteristics, which are not evident in lunar imagery or sampling.

For example, studies at terrestrial impact structures indicate that, at simple craters, the rim consists of structurally uplifted target rocks and includes an overturned and inverted flap of near-surface target materials, which is in turn overlain by ejecta. The bowl-shaped depression observed in lunar images is only the surface manifestation of a simple crater. This bowl-shaped depression is sometimes referred to as the "apparent" crater. Terrestrial data indicate that it is actually the uppermost surface of an underlying allochthonous breccia lens, which is parabolic in cross-section and contained by fractured but allochthonous and parautochthonous target rocks (Fig. 5.5). The crater defined by the parautochthonous target rocks is referred to as the true crater.

At larger diameters, the crater structure evolves, as on the Moon, into complex structures, which consist of a structurally complex rim, a down-faulted annular trough, and a structurally uplifted central area (Fig. 5.6). As with simple structures, complex structures are partly filled by allochthonous material, such as breccias and impact-melt rocks, and an apparent and true crater can be defined (Fig. 5.6). The uplifted central area has initially the topographic form of a central peak, which rises above the floor of the structure and has a height that generally does

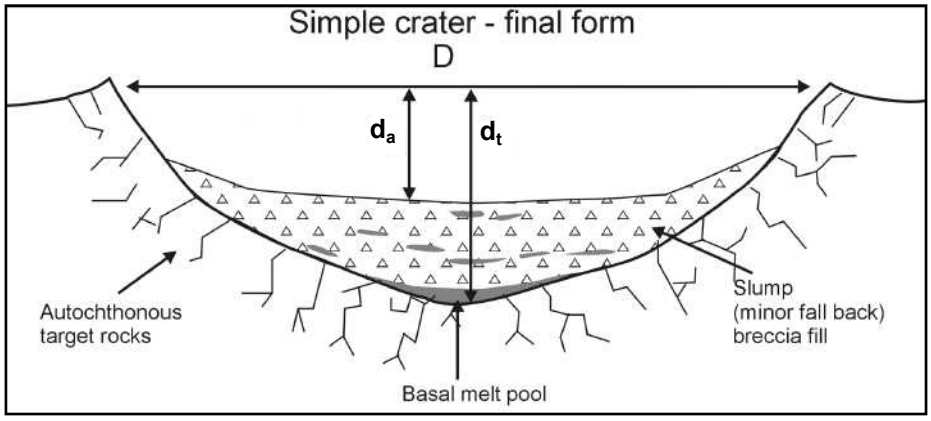

Figure 5.5. Schematic cross-section of a simple crater. D is the diameter and d_a and d_t are the depths of the apparent and true crater, respectively. See text for details.

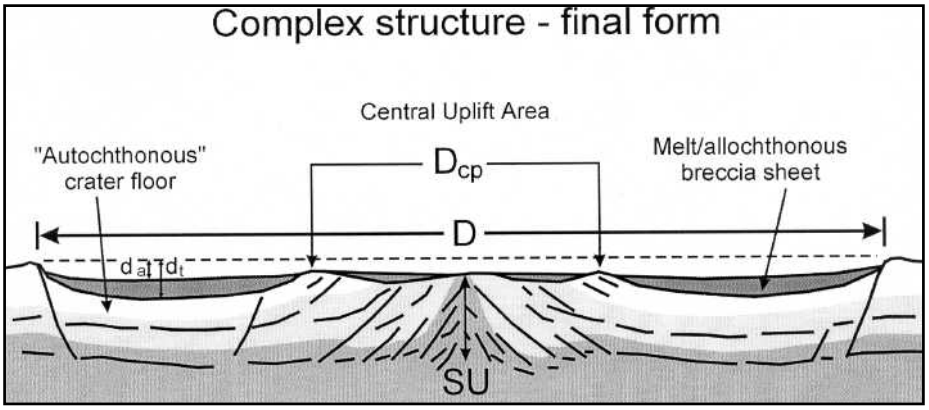

Figure 5.6. Schematic cross-section of a complex impact structure. Notation as in Figure 5.5 with SU corresponding to structural uplift and D_{cp} to the diameter of the central uplift. Note preservation of beds in outer annular trough of the structure with excavation limited to the central area. See text for details.

not exceed the depth from the rim to the floor (Fig. 5.6). With increasing diameter, the central peak is accompanied by a fragmentary ring (a central-peak basin).

Most large, terrestrial complex structures are eroded to varying degrees. There are, however, a number of complex impact structures, which were buried by post-impact sediments almost immediately after formation (e.g., Chicxulub, Mexico; Montagnais, Canada; Puchezh-Katunki, Russia; Ries, Germany), and presumably have a nearly pristine form. They can, however, only be delineated by drill-hole and geophysical data, thus the exact details of their morphologies are generally not well known except for the Ries, which was exhumed as late as Pleistocene. Only the largest terrestrial impact structures have the potential to be peak-ring basins or multiring basins. Unfortunately, the largest structures - Chicxulub, Mexico; Sudbury, Canada; and Vredefort, South Africa - are either buried, tectonically modified, or eroded. Their original detailed morphology cannot be defined with confidence, although they are assumed to represent multiple-ring or peak-ring basins (e.g., Sharpton et al. 1993; Stöffler et al. 1994; Hildebrand et al. 1995; Spray and Thompson 1995; Grieve and Therriault 2000). In the case

of Chicxulub, reflection seismic data have imaged a faulted rim area and a topographic peak ring. Closer to the center, however, there is a loss of coherent seismic reflections and structural details are not known (Morgan and Warner 1999).

There is a desire to compare terrestrial impact structures with lunar impact craters (e.g., Pike 1985), and to assume a greater equivalence in detailed morphology than the observational data may support. Planetary environments result in important differences. For example, secondary target effects on Earth include the transition from simple to complex forms at diameters of ~2 km and ~4 km, depending on whether the target rocks are sedimentary or crystalline, respectively. Some complex impact structures in mixed or largely sedimentary targets do not appear to develop topographically high central peaks. For example, Ries (Germany) and Haughton (Canada) are of similar size (D = ~25 km) and age, and have no emergent central peak. In contrast, Boltysh (Ukraine), which is of a similar size but in a crystalline target, has a central peak that is emergent from the surrounding ~300 m of impact lithologies filling the structure. All these structures have been affected by only minor erosion, and at this time, there is no clear explanation for this difference in their morphologies. However, there is some structural uplift of the central crater basement in all types of complex craters. Therefore, we must assume that the target properties control the morphological expression of this uplift.

Planetary gravity also has an effect on cratering mechanics and, thus, morphologies. The lower lunar gravity (1.62 m^2s^{-1}, or ~1/6 of the average terrestrial value for gravitational acceleration) results in deeper impact structures on the Moon compared with structures of an equivalent size on Earth because gravity acts against both the excavation of material and the formation of topography. The various forms of impact structures and their diameter ranges appear to be an inverse function of planetary gravity (Pike 1985). Moreover, although gravity is a variable in cratering mechanics; it is not a variable in determining the volume of target material melted in a specific impact event. Thus, an impact at a high velocity (e.g., 15 to 20 km s^{-1}) into crystalline target rocks generates ~2.5× more impact melt (relative to the total volume of displaced rocks) in a terrestrial than a lunar event resulting in an impact structure of equivalent size (Cintala and Grieve 1994, 1998). This additional melt, which in large part is retained within the impact structure, also has the effect of reducing observed topographic variations at terrestrial impact structures.

Owing to erosion, few terrestrial impact structures have sufficient topographic information to define morphometric relations. The most recent set of morphometric relations for terrestrial impact structures can be found in Grieve and Pilkington (1996). While erosion may be detrimental to establishing morphometries, it does result in terrestrial impact structures being exposed to different erosional levels. This, combined with on-site geologic investigations and drilling data, clearly indicate that the central peaks of complex craters are due to the uplift of deeper parautochthonous target lithologies. The amount of stratigraphic uplift at terrestrial complex impact structures is:

$$SU = 0.086D^{1.03} \quad (N = 24) \tag{5.2}$$

where N = 24 is the number of structures, with diameters ranging from 4 to 250 km, SU is the amount of stratigraphic uplift of the originally deepest lithology now exposed at the surface, and D is rim diameter, both in km (Grieve and Pilkington 1996).

Attempts to relate these terrestrial data to the lunar case have resulted in a minimum depth of stratigraphic uplift of:

$$SU = 0.022D^{1.45} \quad (N = 12) \tag{5.3}$$

This relation holds for a range of diameters from 17 to 136 km for the lunar case (Cintala and Grieve 1998). There are, however, a number of caveats and ambiguities, the resolution of which awaits better data. Nevertheless, the characteristic of sampling and bringing to the

surface originally deeper lithologies through uplift in complex structures has been used to provide some measure of compositional variation with depth, of the lunar highland crust (Tompkins and Pieters 1999).

2.2.2. Principal impact formations and their geologic setting.

Classification of impactites. Terrestrial impact craters are the only source for a complete data base on the effects of hypervelocity impact on rocks of planetary crusts since they allow us to relate these effects to the cratering process and the final geological setting of the impact-metamorphosed rocks (reviews of these phenomena are in French and Short 1968; Roddy et al. 1977; Stöffler et al. 1979, 1988a; Melosh 1989; Grieve 1987, 1991; and French 1998). In principle, the target rocks are affected by the passage of a shock wave which propagates in a spherical geometry from the point of impact. The material engulfed by the shock wave is not only compressed and heated on an extremely short time scale but also caused to flow behind the shock with supersonic velocity. Depending of the position relative to the point of impact, rocks undergo vaporization, melting, phase transformations in a quasi-solid state, and mechanical deformation before part of rock volume affected in this way is transported (ballistically or in a ground surge mode), mixed, and deposited inside and outside the crater cavity thereby forming proximal, distal, and global deposits. The occurrence, or not, of the latter depends on the size of the cratering event.

The products of impact processes and associated nomenclature are summarized in Table 5.2 and Figures 5.7–5.10. The systematic nomenclature has been derived by the "Subcommission on the Nomenclature and Classification of Metamorphic Rocks" of the International Union of Geological Sciences (IUGS), Subgroup on Impactites (Stöffler and Grieve 1994, 1996, 2006). The proposed Systematics of Impactites apply in principle to all planetary impact formations and form a basis also for the interpretation of shock-metamorphosed lunar rocks and lunar impact formations.

Types and characteristics of impact formations. Four basic textural types of breccias are observed in terrestrial impact craters. This observation generally holds independently of the

Table 5.2. Classification of impactites (recommended by IUGS; Stöffler and Grieve 2006; see also Chapter 1 of this volume).

I. CLASSIFICATION OF IMPACTITES FROM SINGLE IMPACTS
- **1. Shocked rocks**
- **2. Impact melt rocks***
  - 2.1. clast-rich
  - 2.2. clast-poor
  - 2.3. clast-free
- **3. Impact breccias**
  - 3.1. Monomict breccia
  - 3.2. Lithic breccia (clastic matrix breccia without melt particles)**
  - 3.3. Suevite (breccia with melt particles and particulate matrix)**

II. CLASSIFICATION OF IMPACTITES FROM MULTIPLE IMPACTS
- **1. Impact regolith***** (unconsolidated clastic debris)
- **2. Shock lithified impact regolith***** (consolidated clastic debris)
  - 2.1 Regolith breccias *** (breccia with *in situ* formed matrix melt and melt particles)
  - 2.2 Lithic breccias *** (breccia without matrix melt and melt particles)

* may be subclassified into glassy, hypocrystalline, and holocrystalline varieties
** generally polymict but can be monomict in a single lithology target
*** generally polymict but can be monomict in a single lithology target

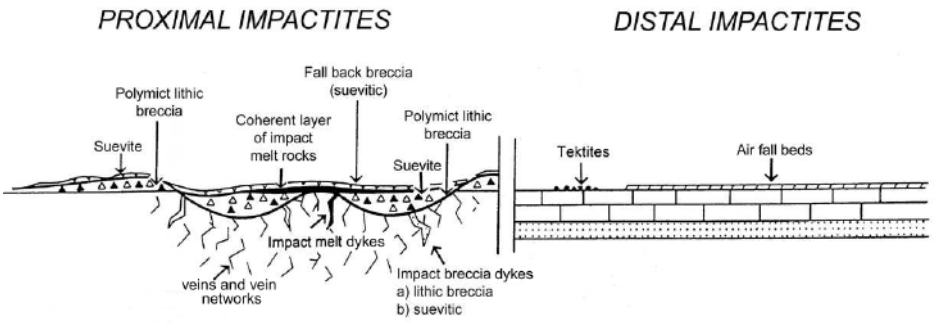

Figure 5.7. Simplified cross section of a complex terrestrial impact crater with proximal and various distal impact formations.

type of target rock and of the geological setting (Stöffler et al. 1979; Stöffler and Grieve 2006), although targets consisting exclusively of sedimentary rocks of high porosity or of evaporite composition lead to somewhat different impact formations. The four types are (Figs. 5.8–5.10; Stöffler and Grieve 2006):

1. Monomict breccias
2. Polymict breccias with particulate matrix and cogenetic melt particles ("suevite")
3. Polymict lithic (fragmental) breccias with clastic matrix (lacking melt inclusions)
4. Impact-melt rocks with variable contents of lithic and mineral clasts in a crystalline or glassy matrix (clast-laden types may be called impact-melt breccias)

These textural types occur in different geologic settings with respect to the parent crater. This is important for the correct interpretation of lunar impact breccias, which come with little or no definitive information concerning the parent crater or impact formation. Therefore, it is useful to discuss the definition of the types and characteristics of the different impact formations identified at terrestrial impact craters (Figs. 5.8 and 5.10) as context for lunar impact materials.

Impact formations may be divided into three structural subgroups:

I. Layered, allochthonous breccias

II. Autochthonous and parautochthonous breccias and shocked basement rocks

III. Breccia dikes (including melt veins and vein networks)

Following Pohl et al. (1977), we may distinguish between (1) *inner* and (2) *outer impact formations,* the latter comprising all deposits beyond the final crater rim. The outer impact formations are "layered" allochthonous breccias (Type I, which may contain Type III, mostly in large megablocks), whereas the inner impact formations include Types I, II, and III. "Layered"

Figure 5.8. *caption continued from facing page...*

Lappajärvi crater, Finland (sample La 41), white to gray lithic and mineral clasts in a dark gray aphanitic crystalline matrix, scale = cm; (f) clast-bearing lunar impact melt rock 14311 with aphanitic crystalline matrix (Apollo 14), scale = cm; (g) polymict lithic breccia with clastic matrix from the continuous ejecta blanket (Bunte breccia) of the Ries crater (Bschor quarry near Ronheim), Germany, scale = cm; (h) lunar polymict fragmental (lithic) breccia 67015 with clastic matrix from the rim of North ray crater (Apollo 16) with dark (impact melt) and light (anorthositic and granulitic rocks) clasts; scale = cm.

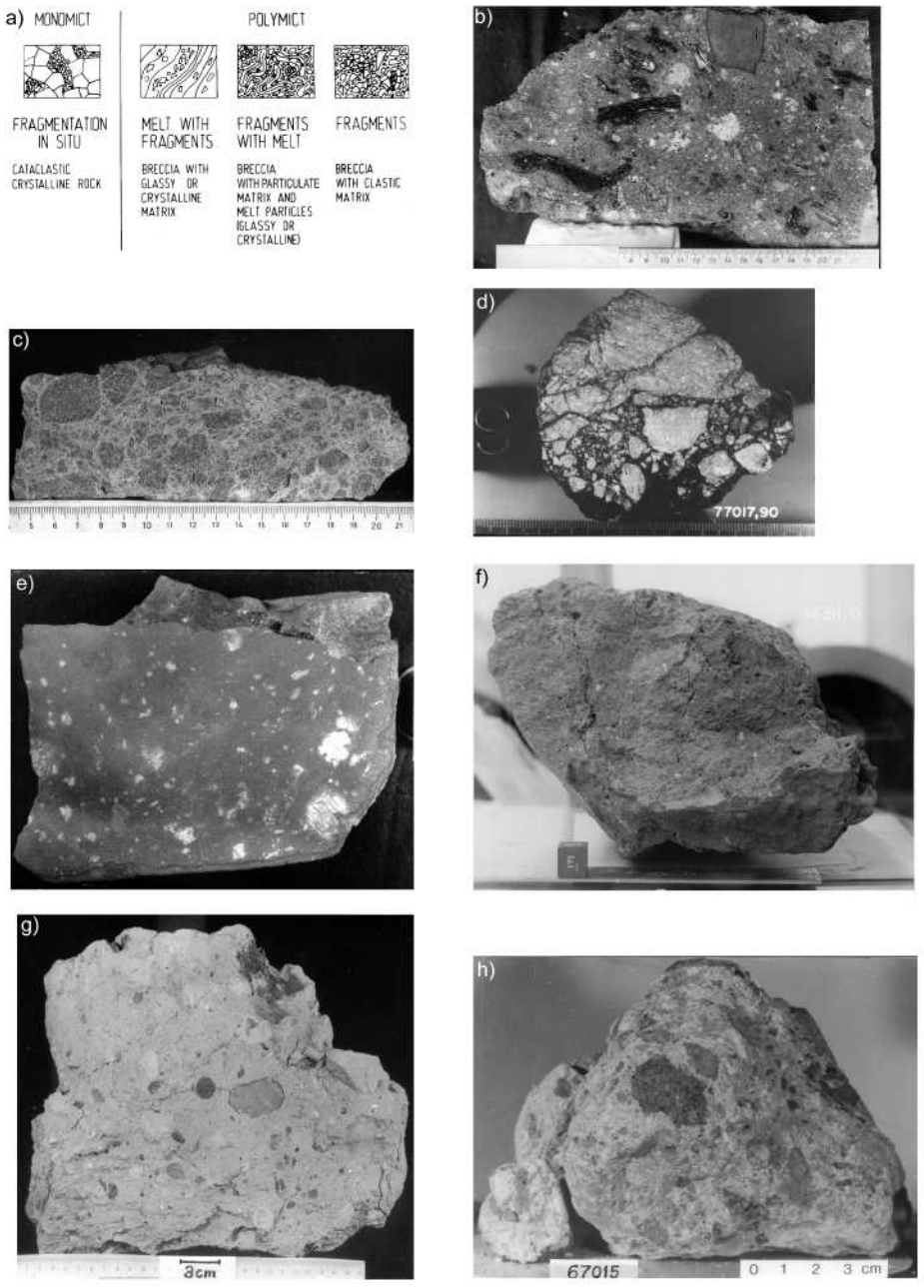

Figure 5.8. Basic types of impact breccia textures and macroscopic images of the main types of terrestrial and lunar breccias (in part from Stöffler et al. 1979); (a) sketches of textural types of impact breccias; (b) suevite breccia with particulate matrix and melt inclusions (black) and crystalline rock clasts (gray to white) from Mien crater, Sweden; scale = cm; (c) monomict granite breccia from Schmähingen, Ries crater, Germany; (d) lunar monomict anorthositic gabbro breccia 77017 (Apollo 17); lower part contains intruded impact melt (black), scale = 1 cm; (e) Clast-bearing impact melt rock from Kanta Ahveniemi, Kärnä island,

caption continued on facing page

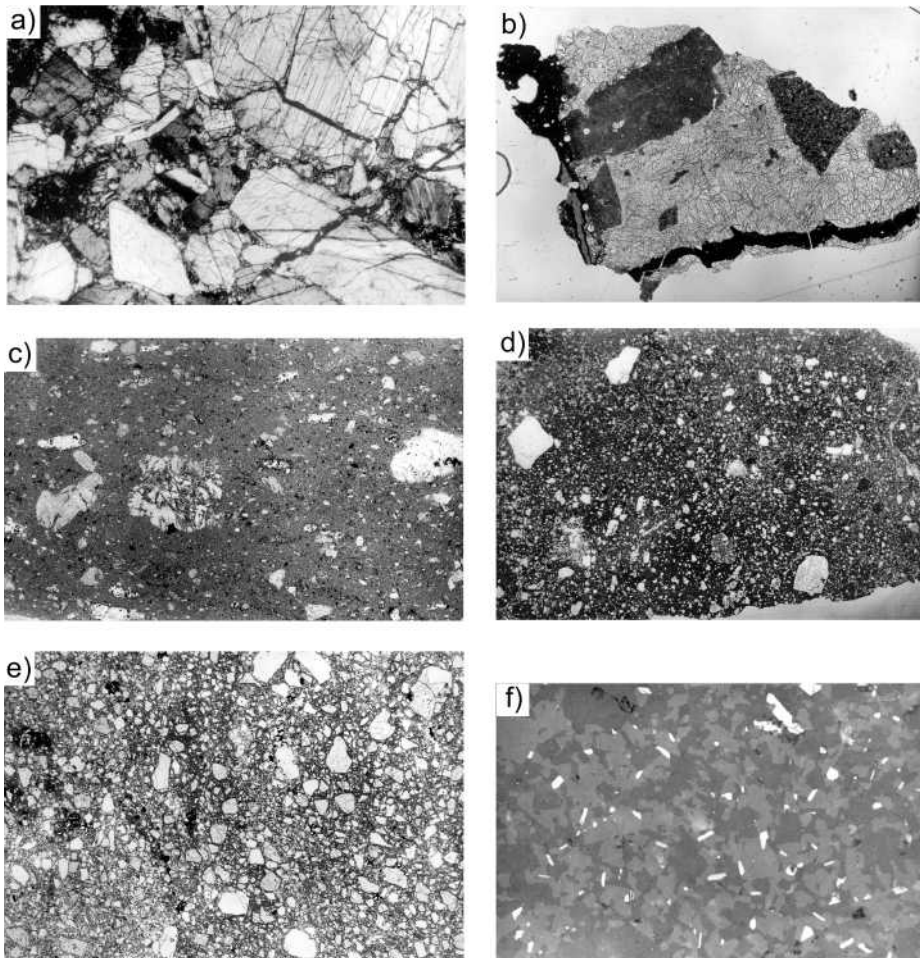

Figure 5.9. Microphotographs of typical textures of the main types of terrestrial and lunar impact breccias (in part from Stöffler et al. 1979); (a) monomict lunar anorthosite breccia 65015,16 (Apollo 16), photomicrograph using crossed polarizers, width of field is 0.25 mm, note intergranular brecciation; (b) lunar dike breccia consisting of gray intrusive impact melt with aphanitic crystalline matrix penetrating into monomictly brecciated anorthosite, younger "pseudotachylite" veins (black) occur on two sides of the sample, width of field = 1.25 mm; (c) clast-bearing impact melt rock with mineral clasts embedded in a fine-grained crystalline matrix from Lappajärvi crater, Finland (sample La 26), width of field = 33.7 mm; (d) clast-bearing lunar impact melt rock 72215,193 (Apollo 17) with lithic and mineral clasts in a fine-grained crystalline matrix, width of field = 15.1 mm; (e) lunar polymict lithic ("fragmental") breccia 76255,69 with clastic matrix consisting mainly of mineral clasts (mainly plagioclase); (f) matrix section of the lunar clast-bearing impact melt rock with crystalline matrix, thin section 14066,46, dark gray = plagioclase, light gray = pyroxene and olivine, white = ilmenite and iron, width of field = 0.23 mm, reflected light.

allochthonous impact formations occur at the top of the section, parautochthonous shocked and monomictly brecciated impact formations below the crater floor, and autochthonous impact formations (monomictly brecciated) at some depth in the crater basement, which in part may have been affected by structural uplifting. In addition, breccia dikes (Type III) occur in the parautochthonous and autochthonous crater basement. The allochthonous outer impact formations contain clasts of local substrate produced by the mechanism of "secondary mass

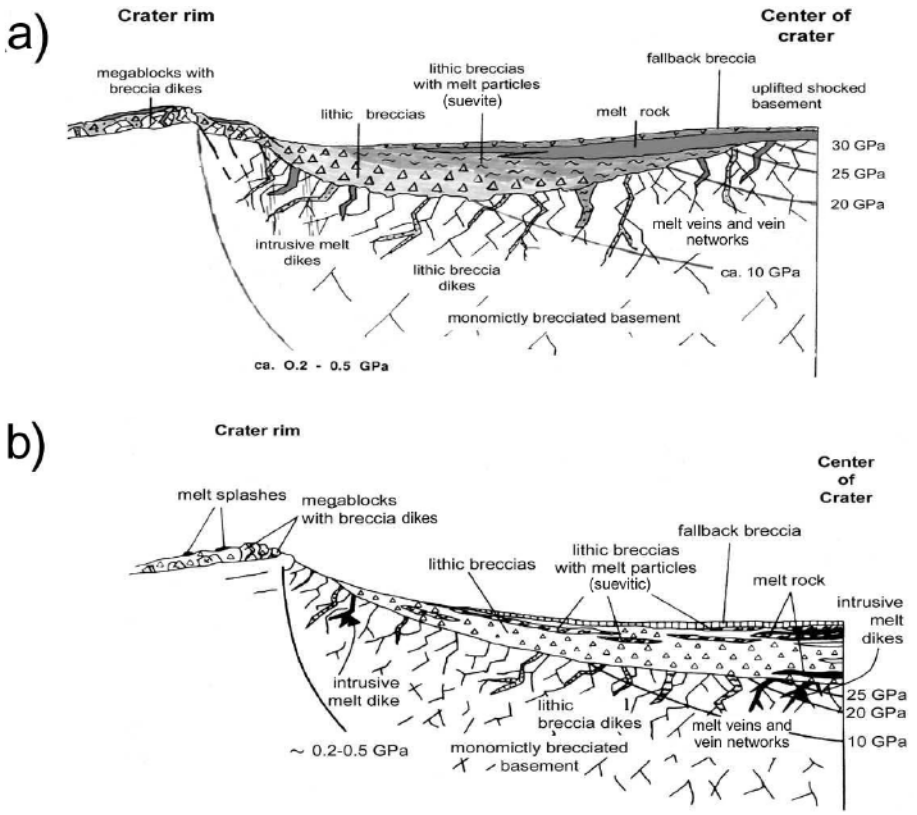

Figure 5.10. Geological setting of impact formations and types of breccias at a complex (a) and simple (b) terrestrial impact crater; note shock pressure isobars given in GPa.

wasting" (Oberbeck 1975) and whose fraction increases with radial distance from the crater rim (Hörz et al. 1983). This is important for the interpretation of lunar breccias taken from the ejecta blanket of multiring basins.

For lunar applications, it is important to distinguish between *proximal ejecta* and *distal ejecta* (Fig. 5.7; Stöffler and Grieve 2006). Proximal ejecta include the allochthonous inner impact formations and the *continuous ejecta blanket* as the innermost part of the outer impact formations. Distal ejecta comprise *global air fall beds* and *tektite glass,* which occur in strewn fields at some distance from the parent craters and represent exclusively shock fused melt from the very top section of the target (see Section 2.3) in contrast to the impact melt residing in melt sheets, suevite breccias, or as glass spherules in global airfall beds (Fig. 5.7). This melt is derived from the deep, inner melt zone of the crater, which develops in the compressed target some distance below the stagnation point of the projectile. Secondary craters—not really known from terrestrial craters—are the result of high velocity distal ejecta and are common around lunar craters, usually outside of the continuous ejecta blanket.

In conclusion, the material ejected from the crater (ejecta of the outer impact formations) forms successively: continuous deposits, discontinuous deposits, and rays (not observed so far at terrestrial craters) with increasing radial distance from a crater. Generally, the velocity of the ejecta decreases with increasing radial distance from the point of impact and with increasing

depth in the target. This leads to the following characteristics of the continuous ejecta blanket: the average size of the ejecta (rock fragments) decreases with increasing distances; the final range of the ejecta is inversely proportional to their original depth in the target (the deepest rocks excavated from the crater form the rim deposits); rock fragments from deeper sections of the target are deposited later than those from higher sections, leading to an *inverted stratigraphy* in the continuous deposits; beyond about 1.5–2 crater radii, the ejecta have velocities sufficient on landing to rework local rock strata and form a radial ground surge of material (secondary mass wasting, Oberbeck 1975) by which a large fraction (e.g., 70–90%) of local rock may be incorporated into the continuous deposits.

The principles outlined above, which have been documented at terrestrial impact structures (e.g., Pohl et al. 1977; Hörz et al. 1983), are key for any geologic exploration of the lunar surface (Shoemaker and Hackmann 1962; Gault et al. 1968; and many others). Firstly, most of the rock fragments in breccias of the distal part of the continuous deposits are from the local bedrock, which is essential for the interpretation of the Imbrium-basin-related Fra Mauro Formation (Apollo 14) and the Descartes Formation (Apollo 16) related to Nectaris basin (Deutsch and Stöffler 1987; Stöffler and Ryder 2001). Secondly, a series of craters, with increasingly larger diameters may thus be used to probe progressively deeper formations in a given geologic terrain, thus enabling reconstruction of first-order stratigraphic and structural relationships at depth from simple surface observations. Such considerations affect our current perception of the lithologic make-up of the lunar crust, based on samples and remotely sensed data (Spudis et al. 1984; Wilhelms 1984; Wilhelms et al. 1987).

Isotope dating of the age of impact events. Determining the absolute age of lunar impact craters and basins and their related ejecta formations is essential for lunar stratigraphy and chronology because of the lack of other datable stratigraphic boundaries. The message for lunar studies from isotope dating to derive the impact age of terrestrial craters is fundamentally important and provides two essential implications: (1) allochthonous impact formations contain rock fragments covering the complete age range from the age of the oldest displaced target rock to the actual age of the impact crater, (2) complete resetting of the ages of the target rocks is only achieved in impact events by vaporization and whole-rock melting. That is, impact-melt rocks from the parent crater (of whatever geologic setting) are the only type of impactite that can reliably be used to date the time of impact (Deutsch and Schärer 1994; Staudacher et al. 1982; Stephan and Jessberger 1992; Bogard et al. 1988). Even then, complications may arise from unequilibrated lithic and mineral clasts of the target rocks in the melt rocks (Bottomley et al. 1990). At large impact craters where impact melt lithologies have characteristically long cooling times, partial resetting of primary ages of the target rocks is commonly observed in lithic clasts included in "hot" impact formations, such as impact melt sheets, suevite layers (Staudacher et al. 1982; Bogard et al. 1988), and thermally annealed bedrock sections of these hot impact formations if the affected bedrock breccias are completely recrystallized (e.g., Footwall breccia at the Sudbury structure, Lakomy 1990). Thus, for lunar applications, impact-melt lithologies should be the first choice in any dating effort. This may result in the direct dating of a crater or in an indirect dating on the basis of the principle that the youngest clast in a polymict impact formation is closest to the actual age of the parent crater. For further details, see Sections 5 and 6.

2.2.3. Fundamentals of progressive shock metamorphism.

Shock metamorphism. Shock-metamorphic effects in rocks and minerals as observed in many lunar samples, particularly from the lunar highlands and the regolith, are well studied and described for terrestrial impact structures in papers in French and Short (1968), Roddy et al. (1977), Stöffler (1972, 1974, 1984), Bischoff and Stöffler (1992), Stöffler and Langenhorst (1994), Grieve et al. (1996), and French (1998). The degree of shock metamorphism produced by a given shock pressure depends on a material's behavior, the so-called equation of state, which relates such parameters as compressibility, specific energy, entropy, specific volume,

and phase changes. The transition from elastic to plastic behavior in dynamically loaded rocks and minerals occurs at relatively high stresses, typically on the order of 5–12 GPa. At pressures between roughly 10 and 60 GPa, mechanical deformation and transitions to high-pressure phases are typical for the common rock-forming minerals. Above about 40 to 100 GPa, thermal effects begin to dominate, and whole-rock melting begins (> ~60 GPa for felsic rocks and > ~80 GPa for mafic rocks, > ~40 GPa for porous siliceous rocks). Pressures exceeding 150 GPa cause vaporization, and ionization occurs at a few hundred GPa. The criteria for the definition of progressive stages of shock metamorphism of various rocks have been defined and classification schemes have been proposed first by papers in French and Short (1968) and later in Kieffer et al. (1976), Schaal and Hörz (1977 1980), Reimold and Stöffler 1978, Schaal et al. (1979), Snee and Ahrens (1975), Bauer (1979), Ostertag (1983), Stöffler (1984), Stöffler et al. (1986, 1988b, 1991), Bogard et al. (1987), Kitamura et al. (1977, 1992), Schmitt (2000), and Xie et al. (2001) for various terrestrial rocks (felsic rocks, basalt, dunite) and for planetary rocks and planetary analog materials such as basalt, dunite, anorthosite, lunar regolith, and chondrites (see also Bischoff and Stöffler 1992, Stöffler and Grieve 2006, and Chapter 1 of this volume).

For lunar crustal material, knowledge of residual shock effects is only essential for a few rock-forming minerals such as plagioclase, olivine, and pyroxene, and for some mafic and feldspathic igneous rocks such as basalt/gabbro/norite, dunite, and anorthosite, as well as regolith. The typical shock effects and the required formation shock pressures are summarized in Table 5.3, which is based on the specialized literature on these materials listed above and a summary in Chapter 1 of this volume.

Impact melt lithologies. Impact-melt rocks constitute a prominent rock type in the Apollo sample suite. Material identified as impact melt composes some 30–50% of all hand-specimen-sized rocks returned from highland landing sites and some 50% of all soil materials, including mare collections (Ryder 1981). Detailed studies of terrestrial impact melt sheets (e.g., Dence et al. 1977; Phinney and Simonds 1977; Whitehead et al. 2002; Dressler and Reimold 2001; and many others) show that the diverse melts derived from the various target rocks in an impact tend to be homogenized, and that the resulting glasses or crystalline rocks, depending on cooling rate, represent remarkably homogenized mixtures of the original target lithologies. In simple terms, impact melts are chemical mixtures of preexisting but now melted target rocks, although there are limitations to the degree of homogenization, particularly at the lower and upper end of the size range of impact craters (e.g., Kettrup et al. 2003). In many cases, the mixed compositions of impact melts have unique chemical characteristics that cannot be produced by conventional internal melting processes, which involve the partial melting of a compositionally restricted source rock.

The spectral composition of impact melts believed to be related to large lunar basins, therefore, has been used to make inferences regarding the composition of the lunar crust (e.g., Pieters et al. 2001). The terrestrial constraints regarding the nature of impact-melt rocks holds for craters up to the 100 km size range. It may not apply directly to the much larger lunar basins. There is an additional complication in the terrestrial environment; namely, the largest known terrestrial impact melt sheet, the Sudbury Igneous Complex at the 250 km diameter Sudbury structure, differentiated on cooling (Therriault et al. 2002). At this time, it is not known if this is a valid analog for the low gravitational environment of the Moon. The volume of impact melt normalized by the total volume of displaced rock masses does not increase linearly with crater diameter, it increases exponentially (e.g., Melosh 1989; Cintala and Grieve 1998). This is important for the interpretation of impact melt lithologies in the lunar highlands (see further discussion in Section 2.3.1)

Most impact-melt rocks contain lithic and mineral clasts from the target (e.g., Stähle 1972; references in Dressler and Reimold 2001; Figs. 5.8 and 5.9). These clasts frequently show distinct shock and thermal effects (Bischoff and Stöffler 1984). Partial digestion of clasts

Table 5.3. Shock effects in rock-forming minerals and whole rocks with shock pressure calibration.

Shock effect	Pressure (GPa)
Shock wave barometry for non-porous felsic rocks	
Kink bands in biotite	> 0.5–1
Shatter cones	> 2
Pf's in quartz: (000l) and $\{10\bar{1}1\}$	> 5–10
Pdf's in quartz: $\{10\bar{1}3\}$	> 10
Pdf's in quartz: $\{10\bar{1}2\}$	> 20
Stishovite	> 12–15
Coesite	> 30
Diaplectic plagioclase glass	28/34* to 45
Diaplectic quartz glass	34–50
Melting of feldspar	> 45
Whole rock melting	> 60
Shock wave barometry for mafic rocks and anorthosites	
Olivine, undulatory extinction	4–5 to 10–15
mosaicism	10–15 to 60–65
planar fractures	15–20 to 60–65
planar deformation features	35–40 to 60–65
melting and recrystallization	> 60–65
Plagioclase, undulatory extinction	5–10 to 10–12
mosaicism	10–12 to 28/34*
diaplectic glass	28/34* to 45
melting	> 45
Orthopyroxene, undulatory extinction	5–10 to 20–30
mechanical twinning	> 5
mosaicism	20–30 to 75–80
planar deformation features	30–35 to 75–80
incipient melting	> 75–80
Whole rock melting, basalt/gabbro	> 75–80
Whole rock melting, dunite	> 60–70
Whole rock melting, anorthosite	> 45–50

Notes: Pf's = planar fractures, Pdf's = planar deformation features; *increasing with increasing An-content

Data from: Müller and Hornemann 1969; Hornemann and Müller 1971; Stöffler and Hornemann 1972; Stöffler 1972, 1974; Snee and Ahrens 1975; Kieffer et al. 1976; Schaal and Hörz 1977; Stöffler and Reimold 1978; Schaal et al. 1979; Bauer 1979; Ostertag 1983; Stöffler et al. 1986, 1991; Bischoff and Stöffler 1992; Stöffler and Langenhorst 1994; Schmitt 2000; see also Chapter 1 of this volume

by the melt typically results in texturally heterogeneous glasses or fine-grained melt rocks. Better crystallized impact melts display an increased tendency to digest clastic material. In completely crystallized impact melts, clastic material may no longer be observed on the scales of thin section and even hand specimens (millimeter to centimeter), yet larger lithic clasts may be observed in the field (Phinney and Simonds 1977). Detailed studies of terrestrial impact-melt rocks have also demonstrated that the clast population in impact-melt rocks does not necessarily constrain the progenitor target rocks that were the source of the impact-melt rocks, as the clasts are acquired as the melt sweeps across the expanding crater cavity (McCormick et al. 1989). This observation has been used in attempts to constrain the source of certain Low-K Fra Mauro rocks in the lunar collection from Apollo 15 (Spudis et al. 1991).

2.3. Impact cratering mechanics

2.3.1. Empirical observations and basic physics of cratering. The basic phenomenology of impact cratering has been well known for decades. Gault et al. (1968) divided the process into three stages, an approach that remains useful and valid today (Fig. 5.11). When a projectile first contacts another object, shock waves are generated in both the impactor and the target, causing the material to flow behind the shock front with supersonic velocity. The material flow field depends on the velocity and angle of the projectile as well as the physical and chemical properties of projectile and target materials.

The earliest part of an impact event, *the compression stage*, encompasses the time from initial contact between the impactor and target to the time that the impactor is completely engulfed by the shock (Fig. 5.11). In a vertical or near-vertical impact, energy transfer from the projectile to the target ceases at that time, as the compressed impactor and target are traveling at essentially the same velocity. This stage, however, rapidly becomes more complex with increasingly oblique impacts, as impactor shearing and highly nonlinear effects become major considerations. The reader is referred to Schultz and Gault (1990), Schultz (1996), Sugita and Schultz (1999), Pierazzo and Melosh (2000a,b), and Ivanov and Artemieva (2002) for

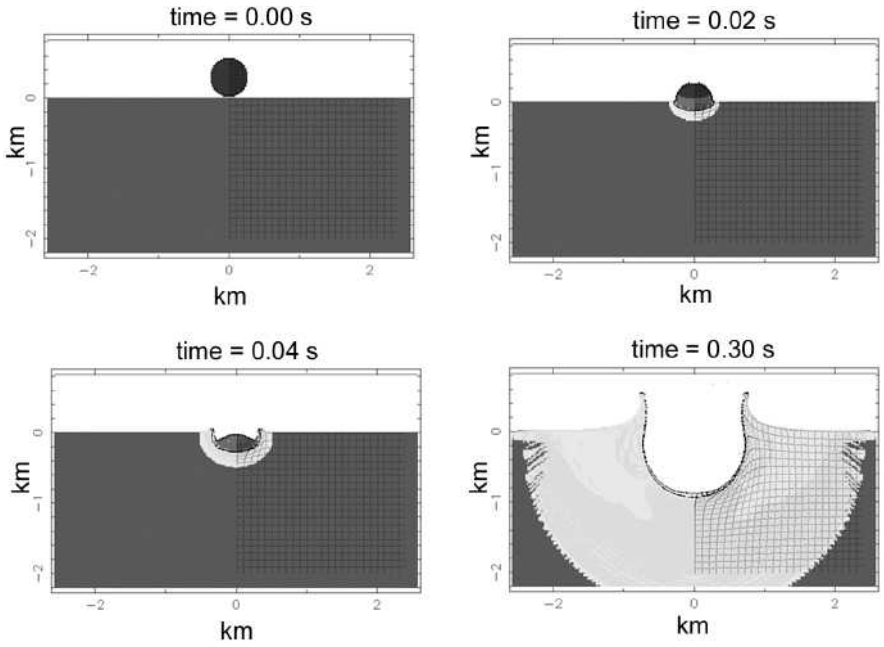

Figure 5.11. Initial stages of impact cratering, illustrated by a numerical model of a vertical impact of a granite impactor into a dunite target with an impact velocity of 15 km/s (granite and dunite are described with ANEOS—analytical equation of state—see Thomson and Lauson 1972). At $t = 0$ both the spherical projectile and the target are presented as intact brittle media. At $t = 0.02$ s, the projectile is partially penetrated into the target. Relatively less dense gray shading presents damaged zones. The progress of penetration is clearly seen at $t = 0.04$ s, the top of projectile is beneath the pre-impact surface and ejection of target material is just beginning. At these early moments the material failure occurs at the shock front. Later, at $t = 0.3$ s, the excavation stage is clearly seen. The projectile is smashed in a thin layer along the transient cavity surface. The shock wave is detached from the cratering flow area. Here the failure zone is far behind the shock front. Near the surface, the failure zone is growing as separated cracks. The mesh of dots in the target is constructed of massless Lagrangian tracers, which follow the material motion (only each 5th row and column are shown).

discussions of the effects of impact obliquity and for additional references regarding aspects of such impacts. The compression stage associated with impacts at interplanetary velocities (up to tens of km per second) is characterized by extreme stresses, rapid entropy generation, very high temperatures, and exceedingly short timescales (e.g., Ahrens and O'Keefe 1977; O'Keefe and Ahrens 1977; Melosh 1989). Pressure is so great that both the impact and target can be treated as strengthless fluids; fused or vaporized material jetted from the interface between the two can travel great distances or escape the target body completely (Kieffer 1977; Sugita and Schultz 1999). The first material ejected by the impact occurs at the time of contact and shortly thereafter, when a combination of very hot impactor and target material is squirted, or "jetted," from the contact between the two (e.g., (Kieffer 1977; Gault et al. 1968). In the case of a large target planet such as the Earth or Venus, most if not all of this jetted phase probably has velocities that exceed escape velocity. However, atmospheric drag may decelerate jets before escape (e.g., Artemieva and Ivanov 2004).

The shock in the impactor has a short but complicated history, reflecting from the irregular surface, spalling pieces of the projectile, reinforcing or attenuating interior stresses, and deceleration of the impactor. Once the shock encounters a free surface, however, it is reflected by a decompression (or "rarefaction") front. Depending on its equation of state and other physical and chemical properties, the impactor will be largely melted or vaporized, and mixed with similarly affected target materials. Conversely, if the impact velocity were sufficiently low, parts of the projectile could survive the impact relatively unscathed and spalled off as solid fragments (Melosh 1984). For oblique impacts, ricochet may occur either with the projectile remaining intact, rupturing into several large fragments, or fragmenting into a myriad of small fragments (Schultz and Gault 1990). This depends on the projectile strength, and the intensity of the effect increases with increasing impact velocity. A common misconception is that the projectile somehow explodes upon impact and that explosion creates the crater.

The *excavation stage* of the event begins after the shock completely engulfs the impactor, thus ending sensible transfer of energy from the projectile to the target (Fig. 5.11). The energy supplied to the target is partitioned into kinetic, thermal and mechanical energy (Gault and Heitowit 1963; Braslau 1970; O'Keefe and Ahrens 1977), but the total energy is constant from the end of the compression stage (energy contained within the target and the ejecta). The intensity of the shock decreases as it encompasses more mass while propagating into the target (Gault and Heitowit 1963). The rate of decrease, however, is also modulated by the irreversible nature of the shock process; the formation of a shock front in any material represents a profligate use of energy. It is highly irreversible in a thermodynamic sense, increasing the entropy of the material through which it passes (e.g., Ahrens and O'Keefe 1972), with greater changes in entropy associated with higher shock stresses. The manifestation of the entropy increase in the shocked material can range from solid-state phase changes through fusion and vaporization to the formation of ionized vapor. As a consequence of this production of waste heat, the energy available to propagate the shock is reduced, and the decay in shock stress with distance is therefore most rapid near the impact point (Gault and Heitowit 1963; Ahrens and O'Keefe 1977; Robertson and Grieve 1977; Cintala et al. 1979; Orphal et al. 1980; Croft 1982; Cintala 1992).

The shape of the shock front in the target at any given time can be thought of as a hemisphere or a truncated sphere, particularly at points far from the impact site (e.g., Gault and Heitowit 1963; Gault et al. 1968; Holsapple and Schmidt 1987; Holsapple 1993). As the shock attenuates, its effects on the target materials decrease from major phase changes through plastic deformation to fracturing. In elastic materials the shock finally propagates as a set of compressional and shear waves dissipating by non-elastic processes. In all cases, however, passage of the shock front imparts a velocity to the target material in a direction parallel to the movement of the front itself with a magnitude roughly proportional to the square root

of the shock stress at that point. Because the shock is nearly hemispherical in a reasonably homogeneous target, the initial motion of the target material is radial from the impact site. This pattern changes as rarefactions propagate into the shocked region from the free surfaces encountered by the shock, including the target surface itself and the boundary of the growing crater or "transient cavity." The net result is an overall motion of the target that is first downward and outward from the impact site, eventually turning upward as individual trajectories are redirected toward the target's surface by the decompression process (Fig. 5.12). The resulting series of trajectories constitute the *flow field*; the best known descriptions of the flow field are the "z-model" of (Maxwell 1973, 1977) and modifications thereof (e.g., Croft 1980, 1981).

Material defining the volume of the transient cavity can be divided into two components: ejected and displaced. One of the idealized trajectories described above delineates the volume of material ejected from the transient cavity from the volume mobilized by the shock but not ejected. The former lies above the "hinge streamline" referred to in Croft's (1980) adaptation of the z-model, whereas the latter lies below it. Superimposing such a flow field on the estimated shape of the transient cavity shows that the ejected fraction comes from the uppermost part of the cavity's volume; the remainder, roughly half the volume of the cavity, is material that is simply pushed out of the way by the shock. This combined process of ejection and displacement has been confirmed by small-scale cratering experiments (Stöffler et al. 1975). At small natural craters, this effect is frozen into the final simple crater form, as documented at the 3.4-km terrestrial crater Brent (Robertson and Grieve 1977), but it is mostly erased in craters large enough to exhibit rebound phenomena. The z-model predicts that the maximum depth of excavation is on the order of a tenth of the diameter of the cavity formed directly by the cratering flow field, i.e., the transient cavity. While this is consistent with the few observations at terrestrial impact craters, it is not well constrained due to the general lack of preserved ejecta as the result of erosion.

As described above, material ejected from locations near the impact site in planetary-scale events is typically both hot and fast. Shocked material farther from the impact site acquires lower velocities, and therefore is ejected at lower speeds. Nevertheless, the faster fraction of

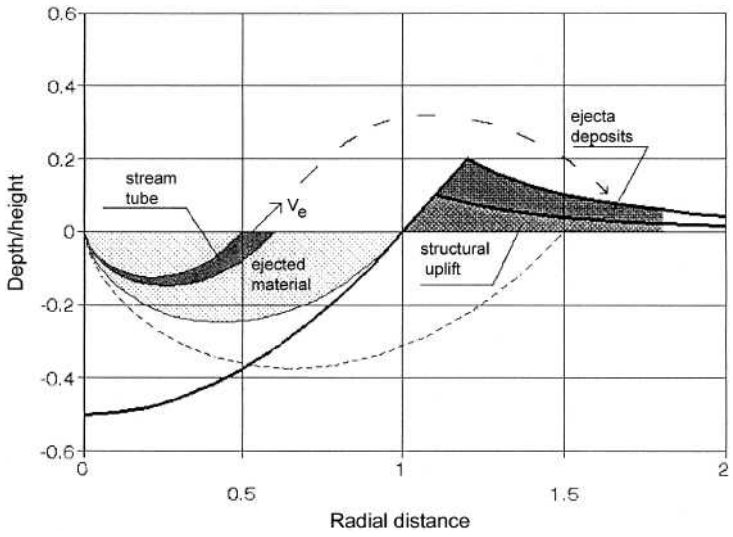

Figure 5.12. Cross section of a transient crater with flow field and excavation cavity; radial distance normalized to the diameter of the apparent crater.

this solid ejecta can be spread over much of the target planet, but because this highly shocked material originated near the impact point, it was almost certainly subjected to high stress gradients and therefore would be severely comminuted (Öpik 1971). The model by Schultz et al. (1981) records the shock state of material as a function of ballistic range and predicts that a wide range of peak pressures is present in the ejecta at a given range, although the peak pressure generally increases with increasing distance from the impact point. Ejecta originating farther from the impact site would be cooler, slower, and less fragmented. The net result of this progression is reflected in the ejecta deposits. Moving away from the crater radially, they grade from a relatively smooth, continuous formation that represents the uppermost component of the crater's rim into a textured deposit that gives way to dense fields of secondary craters. These fields fragment into clusters of secondaries at the extreme limits of the deposit (see Oberbeck et al. 1974; Oberbeck 1975). In dealing with intercrater comparisons of ejecta deposits, it must be kept in mind that the use of scaled distances can be highly misleading.

Deposition of ejecta is obviously an important factor in the mixing of lunar surface materials, but it is dependent on a variety of different factors. Because this process is so complex on the scale of individual samples, agreement among investigators on the nature and absolute extent of such mixing has been difficult to obtain (e.g., Oberbeck et al. 1975; Oberbeck and Morrison 1976; Schultz and Gault 1985). In a terrestrial context, however, a drilling program in the ejecta deposits of the Ries crater in Germany demonstrated unequivocally that local reworked material increases beyond 1 crater radius and composes between 70 and 90 % of the total clast population of the breccia deposits at 2 to 3 crater radii (Hörz et al. 1983). Perhaps the continuing improvement in remote-sensing capabilities will soon provide observational data permitting calibration of the various estimates of mixing ratios as functions of distance from the primary impact on bodies other than Earth. Rationales for this "re-calibration" have been recently presented in the form of a model of global basin ejecta "stratigraphy" by Haskin and coworkers (Haskin 1998; Haskin et al. 2003). The recent quantitative model by Haskin et al. (2002, 2003), based on impact cratering scaling equations (Housen et al. 1983; Holsapple 1993) and the concept of ballistic sedimentation (Oberbeck 1975) predicts characteristics of ejecta deposits, resulting from basin-sized cratering events. These characteristics include deposit thickness at a given distance and fraction of primary ejecta and pre-existing substrate incorporated into the ejecta deposit. The model can be useful for suggesting provenance of sampled lunar material. However, predicted secondary crater densities are at least one order of magnitude greater than observed secondary crater densities surrounding the Imbrium and Orientale basins. The proponents suggest that mutual obliteration erases essentially all secondary craters associated with the debris surge during ballistic sedimentation. If so, a process other than ballistic sedimentation is needed to produce observable secondary craters. This model does not take into account oblique impacts for which the distal ejecta deposits are strongly asymmetric (see discussion of an oblique impact in Section 2.3.2). Some concerns about the Oberbeck model have been expressed by Schultz and Gault (1985).

An attempt to take obliquity into consideration was made by Wieczorek and Zuber (2001) to test the idea of the Imbrium origin for the Imbrian grooves and South Pole-Aitken basin thorium anomaly. Their analysis suggests that the initial material ejected in an oblique impact may be qualitatively modeled by adding a constant velocity tangential to the surface in the impactor's direction to the ejecta velocities determined from the vertical impact-scaling relationships. In reality the nature of oblique impact is much more complex (see Section 2.3.2). The origin of the "grooves" antipodal to Imbrium also remain plausibly related to antipodal convergence of seismic waves (Schultz and Gault 1975).

The *modification stage* of the event begins as soon as the maximum depth of the transient cavity is attained. For a small crater, the floor is raised slightly by elastic and/or gravity-driven rebound, but in a large cavity, the rebound can be on a massive scale (e.g., Grieve et

al. 1981; Ivanov 1994) to the extent that some investigators have suggested that some of the rings of multiring basins are frozen-in "tsunamis" generated by oscillating central rebounds (e.g., Baldwin 1981; O'Keefe and Ahrens 1999). Investigation of the modification stage of the impact-cratering process is much more difficult than the earlier stages for a number of reasons. To a large degree, the compression and excavation stages of large cratering events can be treated as being independent or, at most, only weakly dependent on the target's strength. Cavity modification, however, takes place under conditions that are neither static nor unaffected by material strength (e.g., Melosh and Ivanov 1999). A complication is the poorly understood role of thermal energy and its effects on the material strength of the volume of the target in the cavity's immediate proximity (Cintala and Grieve 1998; O'Keefe and Ahrens 1999). Historically, it has been difficult to include the modification stage in numerical simulations of impacts because of inadequate computational resources. Calculations of the earliest portions of the event are extremely intensive in terms of the number of computer cycles required and the time needed to complete them. The excavation stage is so long relative to the earlier phenomena that until relatively recently it had been addressed only by extrapolating the earlier particle motions ballistically (e.g., Orphal et al. 1980) which is an unappealing but nonetheless unavoidable solution to the problem. Improvements in hardware and coding made calculations to these later times possible, and in recent years, concerted efforts have been made to investigate modification phenomena through computer simulations (e.g., Ivanov 1994).

The rim crest of the transient cavity relaxes from a maximum height that is supported by dynamic stresses during the cavity's growth to a level that is dependent on the magnitude of the event. Small cavities undergo little modification from their transient-cavity form. For larger cavities, wall failure resulting from collapse of the cavity and its subsequent enlargement significantly decreases rim heights of complex craters (e.g., Pike 1977b; Cintala 1979). Mass movement of wall material into the crater has added consequences for the final crater form. Outward-moving impact melt that lined the transient cavity during its growth is transported back into the crater on the slump blocks, to be trapped in the interior as veneers, ponds, or as a coherent melt sheet (Howard and Wilshire 1975; Hawke and Head 1977; Cintala and Grieve 1998). The moving melt mixes with the shocked, brecciated, and highly comminuted material from the cavity walls and floor to form the polymict allochthonous breccias of the crater interior (compare Section 2.2).

Crater scaling. *Scaling* is a term typically used to denote the means by which initial conditions of an impact or explosion can be used to predict the final crater's dimensions. Because the magnitude of even a relatively small planetary impact is beyond anything that can be simulated with current technology, methods must be devised to relate the characteristics of the impactor, the target, the impact velocity, and any other relevant factors with the properties of the resulting crater. The approach used almost exclusively for this task is based on the principles of dimensional analysis (Buckingham 1914; Bridgman 1922). The first extensive use of dimensional analysis in the investigation of cratering phenomena was made by Chabai (1965) in studies of explosion craters; many subsequent investigators applied his work directly to impact events by equating explosive energy to the kinetic energy of the impactor. More than a decade later, however, the lack of a velocity (or momentum) dependence in Chabai's explosion relationships was noted by Holsapple and Schmidt, who developed an extensive suite of scaling relationships for application to impact cratering (Schmidt 1977, 1980; Schmidt and Holsapple 1978, 1982; Holsapple 1980, 1987, 1993; Holsapple and Schmidt 1980; 1982; Housen et al. 1983; Holsapple and Schmidt 1987; Schmidt and Housen 1987). Continuing work by other investigators has tested the scaling relationship predictions, suggested improvements, and incorporated more variables (e.g., Croft 1985; Schultz 1988; Cintala and Hörz 1990; Cintala et al. 1999). A brief discussion of the approach and limitations of dimensional analysis as applied to crater scaling follows, and a few examples are given to illustrate the form that these relationships typically take and to provide a reference for a few of the more common calculations.

In formulating a potential scaling relationship by dimensional analysis, all of the variables needed to describe the process are collected and, following the rules of dimensional analysis as pioneered by Bridgman (1922), groups of those variables are constructed, with the requirement being that no group can possess physical dimensions. For instance, the group P/F, where the variables P and F represent pressure and force, respectively, has the dimensions of length^{-2}, and thus is not a dimensionless group. The group at/v, on the other hand, where a represents acceleration, t time, and v velocity, is dimensionless. The number of such groups are determined by the number of dimensions (e.g., length, mass, time, temperature, etc.) and the number of variables included in the analysis. Once the dimensionless groups (typically called "π-groups") are established, any one of them can be treated as a function of the others; the real task is to determine the nature of that functionality and, in most cases, this can only be done by examining the data.

Laboratory-scale impact craters formed in wet sand probably represent the best analogs available to their large counterparts in rock in terms of scaling studies (Schmidt and Housen 1987). Dimensional analysis has been applied to a set of such craters formed by a variety of impactors over a range of velocities. Using the wet-sand craters as a basis for their analysis, the general form for the rim-crest diameter of the transient cavity D_{tc} as given by (Schmidt and Housen 1987) can be stated as follows:

$$D_{tc} = 1.16\left(\frac{\rho_p}{\rho_t}\right)^{0.39} D_p^{0.78} v_i^{0.44} g^{-0.22} \tag{5.4}$$

in which ρ_p and ρ_t are the densities of the projectile and target, respectively, D_p is the diameter of the projectile, v_i is the impact velocity, and g is the gravitational acceleration. Most transient craters approach a parabolic shape for which transient crater depth H_{tc} is roughly 1/4 to 1/5 of the diameter D_{tc}. The diameter of the transient cavity can be used as a reasonable approximation of the diameter of a simple crater. Models show that appreciable enlargement of simple craters through slumping of their walls would reduce their depths to values lower than are observed (Cintala 1979; Grieve and Garvin 1984; Grieve et al. 1989). The diameters of complex craters, on the other hand, are significantly greater than those of their parent transient cavities because of the modification phenomena described above, and this effect must be included in the scaling relationship for large craters. Croft (1985) derived an expression relating the final rim-crest diameter D_R of a complex crater to the rim-crest diameter of the transient cavity, which can be written as

$$D_R = D_Q^{-0.18} D_{tc}^{1.18} \tag{5.5}$$

where D_Q is the diameter at which the simple-to-complex transition occurs. The value of D_Q for the Moon, for example, is generally taken as 18.7 km (Pike 1988), whereas the corresponding value for crystalline targets on Earth is 4 km (Grieve et al. 1981). Thus, Equation (5.4) can be used for craters with diameters below the simple-to-complex transition on the Moon (Pike 1988); above this size, Croft's (1985) Equation (5.5) must be used with Equation (5.4) to yield

$$D_R = 1.87\times10^{-2}\left(\frac{\rho_p}{\rho_t}\right)^{0.39} D_p^{0.92} v_i^{0.52} \tag{5.6}$$

where cgs units have been assumed and a lunar value for g is 162 cm s^{-1}. Equation (5.6) is applicable only to complex lunar craters. In the event that the crater diameter is known and an estimate of the projectile dimensions is desired, Equation (5.6) can be used to derive D_p for complex lunar craters, *viz.*,

$$D_p = 75.6\left(\frac{\rho_p}{\rho_t}\right)^{-0.42} D_R^{1.09} v_i^{-0.56} \tag{5.7}$$

Small impact craters also depend on the target strength. If the main cratering flow energy is spent as plastic work against strength and friction, this is the so-called "strength regime of cratering," i.e., a "strength crater." For large craters most of the energy is converted into the potential energy of the excavated cavity. This case is in the "gravity regime of cratering" and the crater is termed a "gravity crater." Equation (5.4) is valid for so-called "gravity craters." Figure 5.13 illustrates the general character of the impact-crater scaling by showing the dependence of the rim-crest crater-diameter ratio to the projectile diameter, D/D_p, on the rim-crest crater diameter D for lunar gravity and the impact velocity of 18 km s^{-1} (Ivanov et al. 2001). This figure shows how D/D_p decreases for larger craters.

Melt production scaling. Standard representation of the melt volume V_m in impact craters is $V_m/V_p \sim (v_i^2/E_m)^{\mu}$, where V_p is the projectile volume, v_i is the projectile velocity and E_m is internal energy of melting. O'Keefe and Ahrens (1977) concluded from hydrocode calculations that above a certain limit the total volume of melt and vapor produced in an impact event scaled with the energy of the impactor, resulting in a relation including the factor μ, which they found to be 0.67. However, Bjorkman and Holsapple (1987) tested the point source limit scaling law for melt volumes and found $\mu = 0.55$–0.6. Detailed numerical modeling (Pierazzo et al. 1997) proposed the scaling of melt production for a wide range of impact velocities and target-projectile types in the form:

$$\log\frac{V_m}{V_p} = a + \frac{3}{2}\mu \log\frac{v_i^2}{E_m} \tag{5.8}$$

with $\mu = 0.708 \pm 0.039$ as an average value for all materials. In an oblique impact the melt production is substantially lower (Pierazzo and Melosh 2000b and discussion below).

The only way to prove these multi-stage estimates is to use numerical modeling for estimates of the impact melt volume. Values for the impact melt volume are estimated from geological investigations of terrestrial impact craters (Grieve and Cintala 1992). This test gives a good result, i.e., theoretical estimates reproduce the impact melt volume within of factor of 2 for a given crater diameter (Fig. 5.14).

Excavation depth. Excavation depth is not to be confused with the depth of the transient cavity as the ejecta do not include material excavated from the full depth of the crater (see

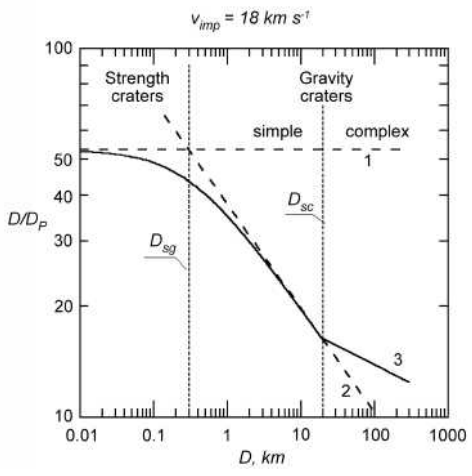

Figure 5.13. The ratio of the crater diameter, D, to the impactor diameter, D_P for various regimes of impact cratering. 1- the "strength branch" of the scaling law, where the D/D_P ratio is constant for a constant effective target material strength; 2 – the "gravity branch" of the scaling law: D/D_P ratio decreases as the crater diameter increases; 3 – the "gravity collapse" branch for complex craters, while the transient crater size is still following the "gravity branch" (2), the final crater diameter is larger than the transient crater diameter due to the crater widening during the transient cavity collapse. The figure is constructed for the impact velocity of 16 km s^{-1} assuming equal projectile and target density, lunar gravity of 1.62 m s^{-2}, strength-to-gravity regime transition at D_{sg} = 300 m (as assumed by Neukum and Ivanov 1994, from the onset of regular continuous ejecta blankets around lunar craters found by Moore et al. 1974), and simple-to-complex crater transition at D_{sc} = 15 km.

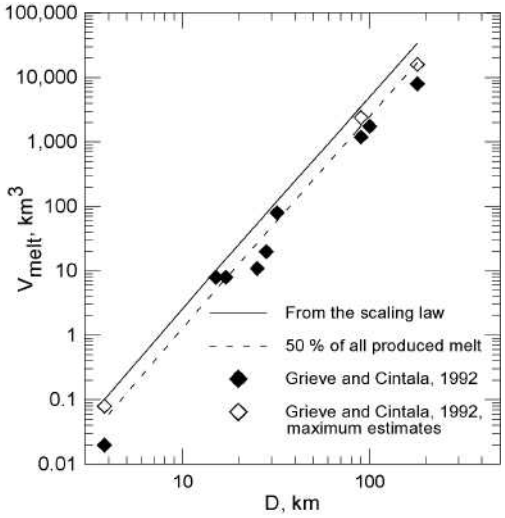

Figure 5.14. Comparison of impact melt volumes for terrestrial impact craters (Grieve and Cintala 1992) with estimates from the scaling law. Scaling laws have been used to estimate the coupling parameter. Following numerical modeling with a given coupling parameter estimates the impact melt volume for typical Earth's crust rocks (granite, gneiss). For an example of these estimates, see Pierazzo et al. (1997).

Fig. 5.12) Material corresponding to the volume of the transient cavity is *displaced* material not *ejected* material. The empirical estimate for the maximum depth of excavation H_{exc} is about 1/3 of the transient crater depth or one-tenth of the transient diameter: $H_{ex} \approx 1/3 H_{tr} \approx 1/10 D_{tr}$.

Ejecta deposit thickness. When the strength can be neglected, the ejection velocity v_e depends upon the ratio of ejection position r within the crater to a final crater radius R (Housen et al. 1983):

$$\frac{v_e}{\sqrt{gR}} = C_e \left(\frac{r}{R}\right)^{\varepsilon} \tag{5.9}$$

where C_e is an empirical coefficient. The power ε can be determined either experimentally or derived from the coupling parameter model. In the latter case it ranges from 1.9 for water to 2.4 for sand (Melosh 1989). Although the thickness of the ejecta deposit may scale similarly, morphological differences are expected as a function of crater size, because the velocity of ejecta that land at a given scaled range depends on a crater size. The ejecta blanket thickness δ falls off as a power of the distance r from the crater center: $\delta = f(R)(r/R)^{-3\pm1}$. A traditional description of the ejecta blanket thickness (McGetchin et al. 1973) $\delta = 0.14R^{0.74}(r/R)^{-3\pm1}$ is from a compilation for data mainly from explosion experiments. Experimental data for impacts are only known from small-scale impact cratering experiments in sand (Stöffler et al. 1975). These data yield a somewhat different function between δ and r, namely $\delta = 0.06R(r/R)^{-3.26}$. However, any scaling is correct only for a vertical impact, and impact obliquity leads to substantial asymmetry in the ejecta blankets, especially at large distances from the crater, outside the "continuous" ejecta blanket (beyond about one crater radius). Experimental and observational results show substantial progress in the understanding ejecta distribution around craters made by oblique impacts (e.g., Anderson at al. 2003; Herrick and Forsberg-Taylor 2003; Schultz and Mustard 2004). However, the general scaling of ejecta blankets at natural impact craters is still an open issue.

2.3.2. Numerical modeling of crater formation by computer code calculations. The first numerical cratering simulation—modeling of the Meteor Crater impact—was done in 1961 by Bjork. Since then, numerical computations began to expand with steadily improving computers and codes capable of providing ever more accurate simulations of the cratering process. Many of the early results achieved by these methods are compiled in papers in Impact and Explosion Cratering (Roddy et al. 1977).

In recent years, numerical models of impact cratering have been applied mainly to Earth, Mars, and small bodies. The main application specific to the Moon has concerned the problem of the Moon's origin in a giant impact (Melosh and Sonett 1986; Cameron and Benz 1991; Cameron 2001; Canup and Asphaug 2001). Recently progress in numerical modeling in impact mechanics has been mainly in the development of more sophisticated models, creation of new three-dimensional codes, and testing on intensively studied terrestrial craters. The time to apply these improved models to problems in lunar cratering is now ripe, as new data sets and increasingly sophisticated observations of the Moon yield new constraints for models and for reevaluation of lunar stratigraphy, which is based mainly on impact events (see Sections 4 and 5).

The physical foundation. The dynamics of an impact, i.e., the displacement and deformation of materials under pressure, stress, and strain as well as the dynamics of any continuous material, are described with a set of differential equations established through the application of the principles of conservation of mass, momentum and energy (e.g., Landau and Lifshitz 1987). These equations are usually coupled with an equation of state, relating the density and internal energy of the material with pressure. A constitutive equation relates the stress in the material to the amount of strain to which the material is subjected. This set of coupled, nonlinear equations can be solved analytically only for a few problems for which certain simplifying restrictions are invoked. Only numerical techniques provide a method of obtaining solutions without appreciable restrictions and simplifications, and thus are widely used in cratering mechanics. They provide important insight into processes and phenomena observed in cratering experiments, and they are the only resource available to study impacts at cosmic velocities, which are unreachable with existing laboratory techniques.

Hydrocodes and modeling of oblique impacts. Computer programs that handle the propagation of shock waves and compute velocities, strain, and stress as a function of time are called "hydrocodes," as initially they did not include strength effects (i.e., materials were treated as liquids). Modern computer codes use sophisticated strength models, such as gradual shear and tensile-damage accumulation, thermal softening, and acoustic fluidization. Many papers and textbooks treat the main principles of hydrocode construction: Eulerian and Lagrangian descriptions, dimensionality, discretization of time and space, numerical schemes, stability, etc. (e.g., Anderson 1987; Zukas 2004 and references therein).

In 1994, hydrocodes were tested for a strengthless material in a giant, natural experiment, the collision of the Shoemaker-Levy 9 comet with Jupiter. Numerical results from various hydrocodes correctly predicted a wide range of impact-related phenomena, including light generated during entry into the Jovian atmosphere, plume formation, and fallout of ejected material (Ahrens et al. 1994; Crawford et al. 1994; Zahnle and MacLow 1994). The results also allowed interpretation of astronomical data and definition of fragment-size distribution (Crawford 1997; Nemtchinov et al. 1997).

Improvements in computer capabilities over the past few years have provided access to the next level of resolution and complexity in impact simulations. Two areas of numerical modeling of impact cratering have received considerable attention recently: (1) oblique impact simulations, which require three-dimensional capability, to model some specific features of non-vertical impacts (Fig. 5.15), and (2) modeling of terrestrial impacts with accurate target lithologies to compare the numerical results with available geological and geophysical data (Figs. 5.16–5.19).

All natural impacts are oblique to some degree, with the most probable impact angle being 45° (Gilbert, 1893; Shoemaker 1962). Although crater rims may appear circular down to low impact angles (15°), the distribution of ejecta around the crater is more sensitive to the angle of impact and currently serves as the best guide to the obliquity of the impact. Numerical modeling has reproduced asymmetric ejection in oblique impacts, providing a means of examining the production of distal ejecta (tektites and martian meteorites, see below), and

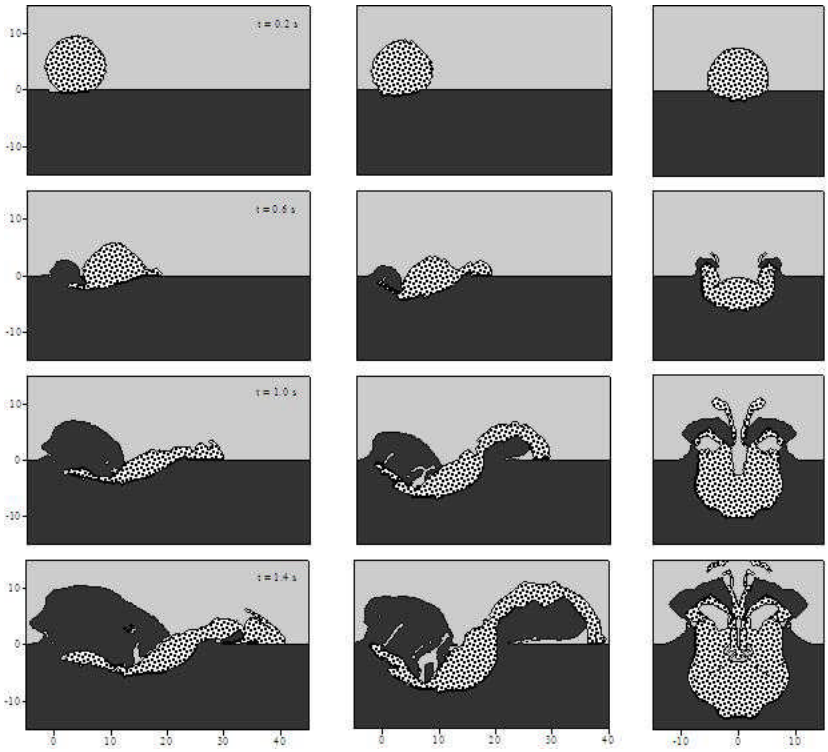

Figure 5.15. Early phases of oblique impact into a target. Material distribution in the plane of impact during the first 1.4 s after the contact (each 0.4 s). A 10 km diameter asteroid moves from the left with velocity of 20 km/s and strikes a solid surface at the point $x = 0$, $z = 0$. The impact angle is 30° in the left column, 45° in the center, and 90° (vertical impact) in the right column. The target is dark gray, atmosphere is light gray and the projectile is stippled.

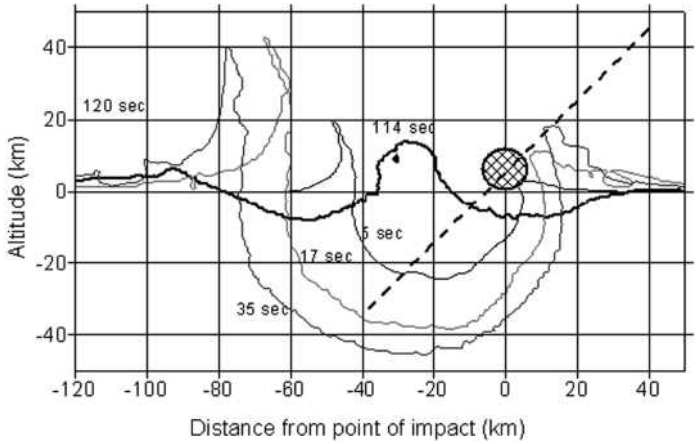

Figure 5.16. Late stage of crater modification by transient cavity collapse. Evolution of the transient cavity for a 45° impact. Patterned circle shows the projectile position at the moment of the first contact with the target. Modeling is for a Chicxulub-scale impact (Ivanov and Artemieva 2002).

revealing substantial differences between vertical and oblique impacts with regard to melt production and the fate of the projectile.

The shock wave generated by an impact weakens with decreasing impact angle (Pierazzo and Melosh 2000a; Artemieva and Ivanov 2001; Stöffler et al. 2002; Fig. 5.17). As a result, both the isobaric core of the initially shocked target material and the volume of melt are asymmetric, both concentrating downrange of the impact point and lying at shallower levels in the target relative to the vertical impact case. The ratio of impact-melt (or vapor) volume to projectile volume has a maximum for vertical (90°) impacts and decreases with impact angle (Fig. 5.17). The decrease is slow for impact angles down to 45°, corresponding to a drop in this ratio of about 20%. For impacts at 30°, however, the ratio decreases by about 50%, whereas at 15°, it is less than 10% of the vertical case (Pierazzo and Melosh 2000a). By incorporating the vertical component of impact velocity (Chapman and McKinnon 1986) standard scaling laws originally proposed by Schmidt and Housen (1987) allow recalculation of these numbers for oblique impacts relative to constant crater volume. In such a case, the ratio of impact-melt volume to crater volume is greatest for a 30° impact (Artemieva and Ivanov 2001). In general, however, scaling laws for oblique impact remain poorly understood for high-velocity planetary impacts. Initial estimates show that high-velocity (>15 km s^{-1}) oblique impacts have practically the same efficiency and produce craters with the same volumes as vertical impacts (Hayhurst et al. 1995; Burchell and MacKay 1998; Ivanov and Artemieva 2001), while laboratory impacts (5–7 km s^{-1}) lose their efficiency rather quickly (Gault and Wedekind 1978; Schultz and Gault 1990). In principle, dimensions of low-velocity impact craters formed in the laboratory depend only on the vertical component of the impact velocity.

Obliquity also influences the fate of the projectile. In particular, the amount and velocity of ricochet are strong functions of impact angle (Schultz and Gault 1990; Pierazzo and Melosh 2000c; Artemieva and Shuvalov 2001). The mass of shock melt or vapor in the projectile material decreases drastically for low impact angles as a result of the shock weakening for decreased impact angles (Fig. 5.18). For asteroidal impacts, the amount of projectile vaporized is limited to a small fraction of the projectile mass. Most of the projectile in cometary impacts, however, is vaporized even at low impact angles. A large fraction of the projectile material

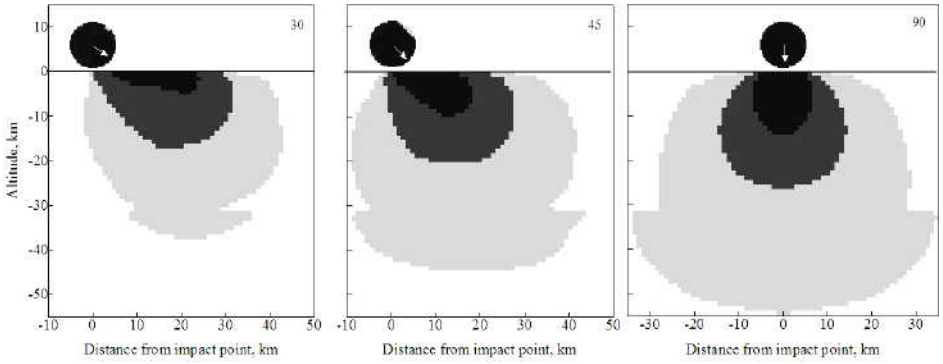

Figure 5.17. Maximum shock pressures in the projectile and the target created with oblique impacts (the central plane through the point of impact is shown). 10 km diameter projectile strikes a Chicxulub-like target (3 km of sediments and 30 km of granite crust on top of a dunitic mantle) with the velocity of 20 km/s. Impact angles are 30° (left plate), 45° (central plate), and 90° (right plate). Light gray color is for shock modified material (20 GPa<P<55 GPa), gray is for melt zone (55 GPa<P<180 GPa), black corresponds to 0 to 30% of granite vaporization (180 GPa < P < 1000 GPa). Most of the projectile is melted or partially vaporized after the shock release. The irregular shape of shock metamorphosed zone in the target is due to refraction of shock waves at the crust/mantle boundary at the depth of 33 km.

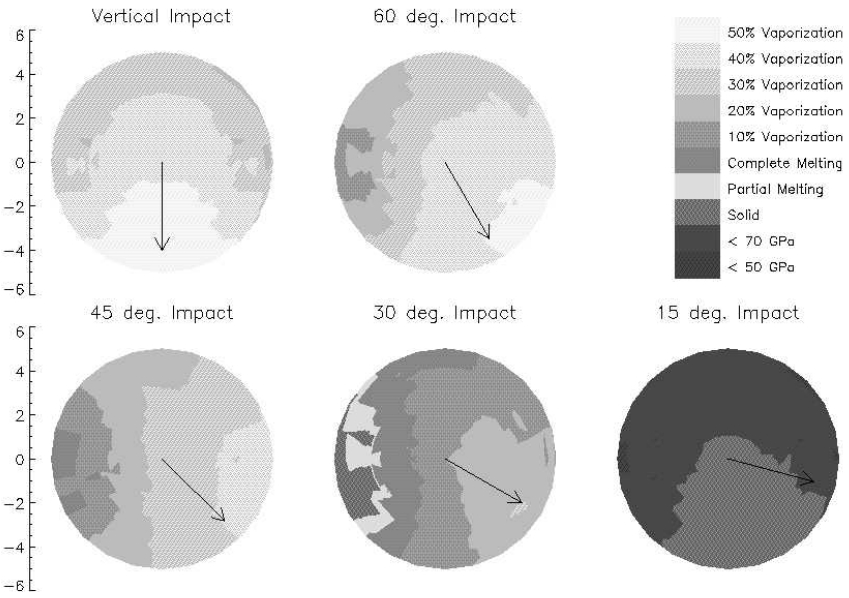

Figure 5.18. Shock pressure distribution in the projectile as a function of impact angle (from Pierazzo and Melosh 2000c).

in oblique impact simulations retains a net downrange motion and a significant amount of it may reach velocities close to or exceeding the escape velocity of Earth. Finally, most of the projectile is ejected from the growing crater in the early stages of an oblique impact. This "ricochet" could explain the absence or very low content of extraterrestrial material in some large impact craters (Palme et al. 1978; Tagle et al. 2004).

Numerical models suggest that oblique impact is the only mechanism giving rise to very special types of impact ejecta including tektites (glassy, cm-sized bodies, deposited within the strewn fields, hundreds of km from the crater, but connected geochemically with the target rocks of the crater) and meteorites from Mars and the Moon (Fig. 5.19). Full-scale, 3D modeling (Artemieva 2001; Artemieva and Ivanov 2002) suggests that no specific conditions are needed to produce these ejecta. The most conducive impacts likely have impact angles in the interval from 30° to 60° and impact velocities typical for Mars (10 km s^{-1}) or Earth (18 km s^{-1}). The obvious deficiency of tektite strewn fields (only four known strewn fields for more than 160 impact craters) may be explained by erosion and weathering and/or a paucity of young craters with diameters larger than 10 km. Martian meteorites may be launched by small asteroid impacts with final crater diameters of 1–3 km (Head et al. 2002), under the restriction that solid fragments larger than 20 cm in diameter are ejected at or above escape velocity from the upper few meters of the target (Artemieva and Ivanov 2002). Detailed numerical simulations with high spatial resolution of this upper layer do not support the idea of meteorite launch without substantial (~10 GPa) compression. This numerical result agrees well with petrological data (Fritz et al. 2003), but conflicts with simplified estimates by Mileikowsky et al. (2000) and is only marginally compatible with magnetic data for ALH84001 (Weiss et al. 2000). Similar conclusions can be drawn for lunar meteorites for which the depth of the subsurface source layer and the range of shock pressures is somewhat lower that in the martian case.

Verification of computer code by direct comparison with laboratory impact experiments, such as those by Schultz and coworkers (e.g., Schultz 1996; Dahl and Schultz 2001), remains an

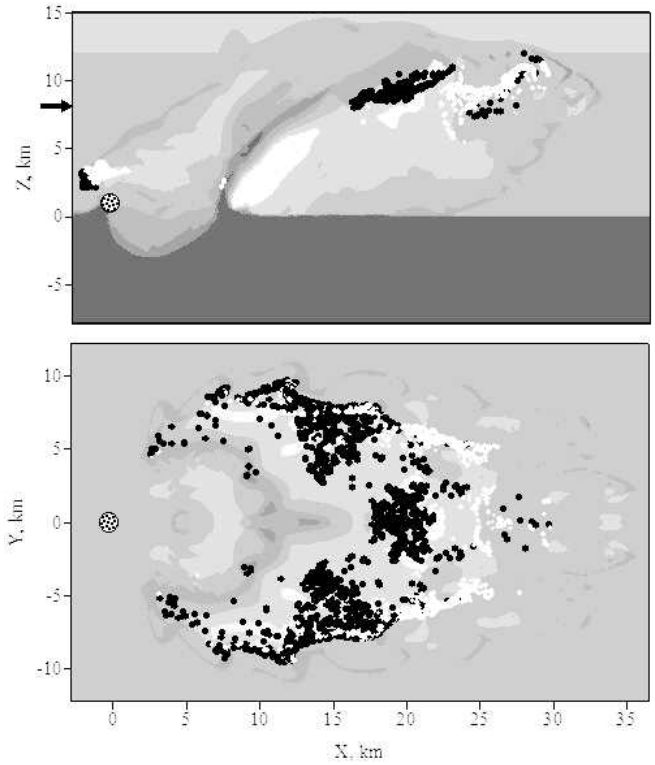

Figure 5.19. Ejection of tektites from the Ries crater. Vertical slice XZ in the plane of impact is on the upper plate, horizontal slice XY at an altitude of 8 km (see arrow) is on the bottom plate. 1.5 km in diameter asteroid (shown as dotted circle) strikes the target at the point $x = 0$, $y = 0$, $z = 0$ with velocity of 20 km/s and impact angle of 30°. Density distribution two seconds after the contact is shown in gray scale, microtektites (<0.1 cm) are shown as white, real tektites (>1 cm) are shown as black.

open issue. Problems in comparing experiments and numerical modeling include lower impact velocities and small scale in impact experiments; however, limitations also exist in the computer simulations. Notwithstanding their fundamental role in the investigation of oblique impacts, laboratory experiments cannot achieve the impact velocities and scale typical of planetary impacts. These limitations necessitate the use of numerical modeling for the study of impact events.

3. THE LUNAR IMPACT FLUX AND CRATER PRODUCTION FUNCTIONS

3.1. Crater production functions

Several decades of lunar exploration have accumulated enough data to present an approximate lunar chronology based on the ages of returned samples. The study of the *size-frequency distribution* (SFD) of lunar impact craters forms a solid basis to show that the SFD has been relatively stable since the end of the early heavy bombardment and that the process of crater formation is still going on. Impact craters represent therefore a record of small body evolution and Solar System chronology.

Despite a comprehensive study of the Solar System cratering record, the question of the "exact" form of the size-frequency distribution of impact craters created on a fresh geologic

unit (i.e., totally rejuvenated at the beginning of cratering with no further obliteration of craters) is far from a final answer. Partially this is a consequence of the fact that it is difficult to identify large "fresh" surfaces because, in most cases, planetary surfaces have a complex geologic history with simultaneous crater accumulation and degradation (e.g., Hartmann 1995). However, some general conclusions can be drawn. Today there are two independent evaluations of the production SFD, named "Hartmann's SFD" and "Neukum's SFD" after the names of the main proponents.

Three main forms of SFD presentations are used. The *cumulative* form presents the number of craters with diameter equal or greater than D: $N = N(>D)$. The *differential* (incremental) distribution (i.e., the Hartmann production function) is the derivative dN/dD of the cumulative SFD $N(>D)$. It gives the number of craters in equal diameter bins: $N(D, D + \Delta D)$. The incremental distribution is a log-incremental distribution where bin boundary diameters have a constant ratio (e.g., from 1 to 2 km, from 2 to 4 km, etc.). As the crater SFD is close to a power law, the *relative* distribution R (or R-plot) presents the deviation of the SFD from the "base" power law:

$$R = D^3\ (dN/dD) \tag{5.10}$$

In practice, the R distribution is calculated on the basis of finite increments of D.

3.2. Hartmann production function — HPF

The tabulated HPF is an assemblage of data selected by Hartmann to present the production function for one specific moment of time, the average time of lunar mare surface formation (see Neukum et al. 2001). In this case the condition for a fresh surface is satisfied by the fact that most lunar mare basalt samples have a narrow range of ages around 3.2 to 3.5 Ga (Stöffler and Ryder 2001), which restricts the lunar maria to an age range within a factor of 1.1. As the tabulated HPF is the result of some averaging of individual crater counts in different areas, it should be treated as a relatively reliable model approach to the construction of the power function. Hartmann uses a log-incremental SFD representation with a standard diameter bin size. The number of craters per km^2, N_H, is calculated for craters in the diameter bin $D_{LFT} < D < D_{RGT}$, where D_{LFT} and D_{RGT} are the left and right bin boundary and the standard bin width is $D_{RGT} = 2^{1/2} D_{LFT}$. Hartmann et al. (2000) approximated the tabulated HPF in the form of a piece-wise, three-segment power law (coefficients first published jointly by Hartman and Neukum et al. 2001):

$$\log N_H = -2.616 - 3.82 \log D_{LFT};\ D_{LFT} < 1.41 \text{ km} \tag{5.11a}$$

$$\log N_H = -2.920 - 1.80 \log D_{LFT};\ 1.41 \text{ km} < D_{LFT} < 64 \text{ km} \tag{5.11b}$$

$$\log N_H = -2.198 - 2.20 \log D_{LFT};\ D_{LFT} > 64 \text{ km} \tag{5.11c}$$

This function is shown in Figure 5.20. Hartmann's choice of power law segments was made in the 1960s when he began this work and was made for historical reasons. At that time, only the shallow branch 1.41 km < D < 64 km was well established, while the pre-existing literature had suggested such laws for asteroids and meteorites, which Hartmann was attempting to relate to the lunar data.

3.3. Neukum production function (NPF)

In a series of publications, Neukum proposed an analytical function to describe the cumulative SFD of lunar impact craters (Neukum 1983; Neukum and Ivanov 1994). Neukum showed that the production function had been more or less stable from Nectarian to Copernican epochs (i.e., from more than 4 Ga until the present). By this time the full size spectrum of craters was known, and in contrast to the piecewise exponential equations used for the HPF, Neukum computed a polynomial fit to the cumulative number of craters, N, per km^2 with diameters larger

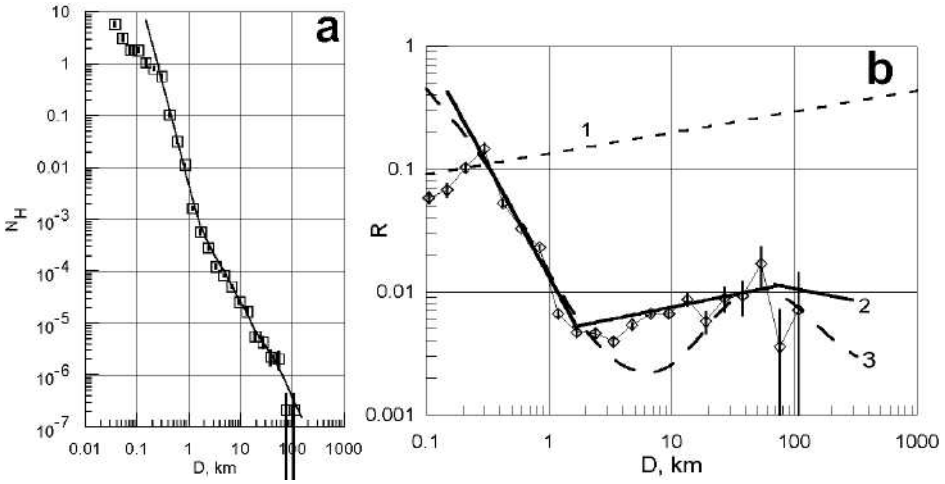

Figure 5.20. (a) Incremental representation of the Hartmann production function (HPF). The HPF, in a direct sense, is the set of points shown in the plot as squares. Straight lines represent the piece-wise power law fitting of the data (Eqn. 5.11). (b) Comparison of production functions derived by Hartmann (HPF, shown as diamonds) and Neukum (NPF) in the R plot representation. The maximum discrepancy between HPF (2) and NPF (3) (roughly a factor of 3) is observed in the diameter bins around $D \sim 6$ km. Below $D \sim 1$ km and in the diameter range of 30–100 km, the HPF and NPF give the same or similar results. Fitting the HPF to NPF Equation (5.12) yields a model age of 3.4 G.y. The NPF, which is fit to the wide range count of impact craters in the Orientale Basin, yields a model age of ~3.7 G.y. The dashed line 1 represents the approximate saturation level estimated by Hartmann (1995). The HPF power law segments (solid line labelled 2 in part b) correspond to Equation (5.11a) for $D < 1.41$ km, to Equation (5.11b) for 1.41 km $< D <$ 64 km, and to Equation (5.11c) for $D > 64$ km.

than a given value D. For the time period of 1 Ga, $N(D)$ may be expressed (Neukum 1983) as:

$$\log_{10}(N) = a_0 + \sum_{n=1}^{11} a_n \left[\log_{10}(D)\right]^n \tag{5.12}$$

where D is in km, N is the number of craters with diameters $>D$ per km^2 per Ga; the coefficients a_n are given in Table 5.4. Equation (5.12) is valid for D from 0.01 km to 300 km. Recently, the NPF was slightly reworked toward the largest craters by re-measuring in that size range (Ivanov et al. 1999, 2001; Neukum et al. 2001). The time dependence of the a_0-coefficient is discussed in the following subsection. A similar equation is used to characterize the projectile SFD derived in Ivanov et al. (2001). Coefficients for this projectile SFD are also listed in Table 5.4. In the projectile SFD column, the first coefficient a_0 has been set to zero for simplicity. This coefficient determines the absolute number of projectiles. The absolute value of a_0 for projectiles may be found by fitting to observational data (see Section 3.7).

3.4. Towards a unified production function

In Figure 5.20b, the NPF and HPF are shown in an R-plot together with representative data for crater counts on the lunar maria and the Orientale basin. The NPF was fit to the crater counts using an assumed age of average lunar maria of 3.2 to 3.5 Ga. We find that both the HPF and NPF are a good match to the observational data below $D \sim 1$ km. However, for $D > 1$ km, the HPF lies well above the NPF, meeting again the NPF at crater diameters $D \sim 40$ km. A maximum discrepancy of a factor of 3 between HPF and NPF is observed in the diameter bins around $D \sim 6$ km. Below $D \sim 1$ km and in the $30 < D < 100$ km range, the HPF and NPF give the same or similar results.

Table 5.4. Coefficients of the analytic production function (Eqn. 5.12) for cumulative number of craters $N(D)$ with diameters larger than D, and relative number of projectiles $R(D_P)$* assumed from measured $N(D)$.

a_n	**"Old" $N(D)$** *(Neukum 1983)*	**"New" $N(D)$** *(Neukum et al. 2001)*	**"New" $N(D)$ sensibility****	**Projectile $R(D_P)$** *(Ivanov et al. 2000)*
a_0	−3.0768	−3.0876		—
a_1	−3.6269	−3.557528	± 3.8 %	+1.375
a_2	+0.4366	+0.781027	± 3.9 %	+0.1272
a_3	+0.7935	+1.021521	± 2.5 %	−1.2821
a_4	+0.0865	−0.156012	± 1.6 %	−0.3075
a_5	−0.2649	−0.444058	± 0.88 %	+0.4149
a_6	−0.0664	+0.019977	± 1.3 %	+0.1911
a_7	+0.0379	+0.086850	± 0.78 %	−0.04261
a_8	+0.0106	−0.005874	± 1.8 %	−0.03976
a_9	−0.0022	−0.006809	± 1.8 %	-3.1802×10^{-3}
a_{10}	-5.18×10^{-4}	$+8.25\times10^{-4}$	± 5.6 %	$+2.799\times10^{-3}$
a_{11}	$+3.97\times10^{-5}$	$+5.54\times10^{-5}$	± 24.1 %	$+6.892\times10^{-4}$
a_{12}			—	$+2.614\times10^{-6}$
a_{13}			—	-1.416×10^{-5}
a_{14}			—	-1.191×10^{-6}

* Relative number of objects (craters or projectiles) is defined as (e.g., Hartmann et al. 1981) $R(D) = D_x^{-3}(dN/dD_x)$ where N is the cumulative number of objects with size larger D_x (crater diameter, D, or projectile diameter, D_P, correspondingly).

** "Sensibility" is the coefficient variation which changes the $N(D)$ value by a factor of 2 up and down.

Although Figure 5.20b shows that the HPF and NPF share some similarities, the factor of 3 discrepancy for $2 < D < 20$ km craters requires further investigation. The discrepancy between HPF and NPF reflects the discrepancy in observational data used to construct the production function. A real "unification" of two types of production functions would require a re-counting of craters in critical areas. In general, one should be cautious in interpreting data in this range, particularly since different data sets show somewhat different SFD curvatures. Additional studies of lunar mare data are needed to further refine the accuracy of the main production-function curve.

To use a production function, one should first select a portion of the lunar surface where all the accumulated craters since the last resurfacing event can be counted. Examples of such "time slices" are:

a) The Orientale basin, which erased a large area near the base of the Imbrian stratigraphic horizon.

b) The emplacement of mare basalts (Hartmann 1970; Hartmann et al. 1981);

c) Eratosthenian-ages craters, which mostly have good stratigraphic dates (Wilhelms et al. 1987)

Figure 5.21 shows crater counts for lunar areas that differ by a factor of 100 in the density of craters per unit area. An examination of these "time slices" suggests that we cannot rule out the simple hypothesis that the lunar production function had a constant shape from ~4 Ga (lunar highland formation) to ~1 Ga (ray craters). Thus, in the limits of data accuracy, we can assume that the projectile SFD was stable over this interval. To test this hypothesis, we compare lunar data to the cratering records found on other planets and asteroids (Sections 3.5–3.7).

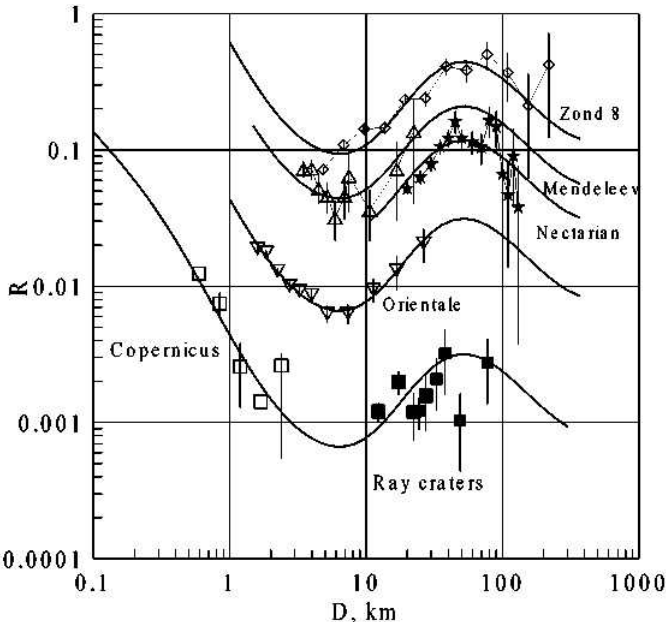

Figure 5.21. *R* plot for several "time slices" of the lunar impact chronology fitted with the NPF curve (Eqn. 5.11b). See data description in Neukum et al. (2001).

Although the HPF and NPF are somewhat different, both assume that the general shape of the SFD of impactors striking the Moon over the last 4 Ga was the same. A different point of view is given by R. Strom (Strom and Neukum 1988; Strom et al. 1992), who claims that the "modern" (post-mare) production function is quite different from that produced during the epoch of the early heavy bombardment. A more extensive treatment of this subject can be found in Strom and Neukum (1988).

3.5. SFD for craters in comparison with asteroids

Recently improved data in astronomical observations of asteroids permit comparison of SFD for lunar craters and asteroids. Using the impact cratering scaling laws and average impact velocity for asteroids (see review by Ivanov et al. 2001), one can convert the lunar production function into a "projectile" size-frequency distribution. This "crater-derived" SFD may be compared directly with astronomical observations of main belt asteroids (Ivanov et al. 2003).

Deviations from a simple power-law SFD of craters considered above suggest that the SFD of asteroids also deviates from a simple power law. A possible mechanism for producing such deviations is based on modeling results describing impact evolution in the main belt (i.e., a "wavy" SFD according to Campo Bagatin et al. 1994a,b; Durda et al. 1998; Davis et al. 2002). For bodies with diameters near a few hundred meters, self-gravity helps prevent catastrophic disruption events by allowing fragments to re-accumulate with the target asteroid (e.g., Love and Ahrens 1996; Melosh and Ryan 1997; Benz and Asphaug 1999). As bodies get stronger via gravity, more projectiles of that size are available to disrupt larger asteroids, ultimately leading to a wave in the shape of the SFD.

The Spacewatch data (Jedicke and Metcalfe 1998) and data of the Sloan digital sky survey (Ivezic et al. 2001) allow estimation of the asteroid SFD down to diameters of approximately 300 m. Observational data agree reasonably well with the "projectile" size frequency

distribution derived from the lunar crater curve (Ivanov et al. 2003). This similarity supports the idea that lunar craters may result from bombardment by collisionally evolved families of projectiles, similar to those in the modern Main Asteroid Belt.

3.6. Near-Earth Asteroids

An SFD similar to the one of the Main Belt is found for Near-Earth Asteroids (NEAs). Figure 5.22 summarizes several recent SFDs estimated from astronomical observations and models of the NEA population. These results are compared to the projectile SFD derived from lunar cratering records with HPF and NPF. The similarity between the following SFDs, (1) crater-forming projectiles derived from 1 to 4 Ga old surfaces on the Moon, (2) the observed main belt asteroid population, and (3) NEAs (Fig. 5.22), suggests a common connection, namely that the main belt is the predominant source of both the current NEA population and those projectiles that have struck the Moon over the last several Ga.

3.7. Craters on Earth and other terrestrial planets

Having the "projectile" SFD estimates on the basis of lunar crater counts, it is possible to construct model crater SFD's for Mercury, Venus, Earth, and Mars, and to compare the model SFD with real observation. The construction of model SFD's takes into account different

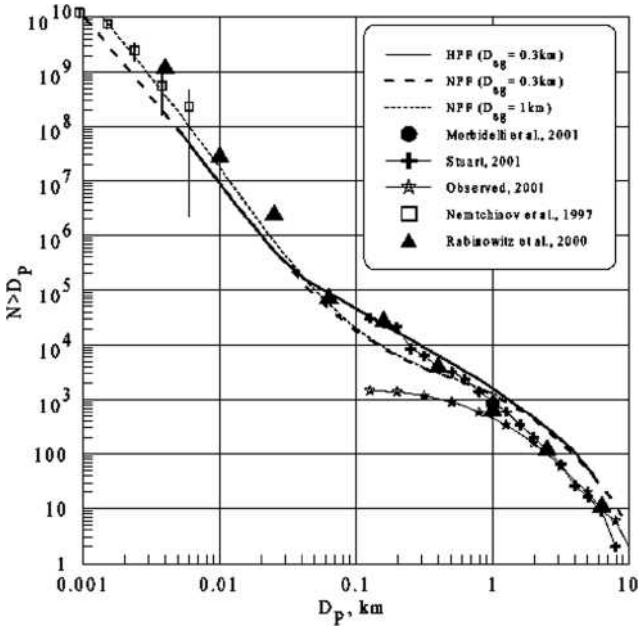

Figure 5.22. Estimates of a cumulative, $N > D_P$, size-frequency distribution for NEAs. The solid, dashed, and dotted lines are model distributions derived from the HPF and NPF for various assumed strength-to-gravity transition diameters for lunar craters. The absolute position of these curves corresponds to the lunar chronology (Eqn. 5.12) combined with estimated average impact probability for Earth-crossing asteroids (ECAs). The number of NEAs (defined as bodies with $q < 1.3$ AU) is larger. For observed bodies with $H <$ 15, the ECA to NEA ratio is ~0.57. Recent astronomical estimates by Rabinowitz et al. (2000), Morbidelli et al. (2001), and Stuart (2001) are generally consistent with these estimates. Satellite observations of bolides entering Earth's atmosphere (Nemtchinov et al. 1997) are consistent with our results for small ($D_P < 10$ m) bodies, although we caution that it is problematic to convert light flashes detected in the atmosphere into projectile sizes. The average probability of ECA impacts is used to estimate the total number of projectiles and the impact (or atmospheric entrance) rate.

gravity values and different average impact velocities for these planets (see details in Ivanov 2001; Ivanov et al. 2001; Neukum et al. 2001).

A recent review of the recalculation of the lunar SFD for the conditions of other planets is given by Ivanov et al. (2003). A tentative conclusion from the review is that within the limits of data accuracy, the size-frequency distribution of craters and, hence, of crater-forming projectiles, appears similar in time (for older and younger craters) and space (for terrestrial planets). Variations in the projectile SFD cannot be excluded (e.g., the role of comets is not yet well defined). However, the assumption of a constant shape of the crater production function (SFD) as a function of time is a reasonable starting point for further discussion. The constant shape of the production function means that the systematic deviation of the lunar crater SFD from a simple power law is stable and is the same for the early heavy bombardment projectiles and for the current near-Earth asteroids. Within model constraints, crater counts can be used as a measure of a relative crater retention age for various areas on the Moon. The absolute ages have been inferred from the dating of lunar returned samples (Sections 5.5–5.7).

Details of the crater SFD for other terrestrial planetary bodies will not be discussed here. However, we briefly present the cratering record of the Earth to represent the Earth-Moon system as a whole. A comprehensive discussion of the lunar chronology from cratering statistics is given in the following sections.

Hartmann (1965, 1966) pointed out that large terrestrial craters reflect an older population, while smaller craters are continually removed by erosion, producing an observed SFD that differs from the production function. The inspection of data from the North American and European cratons (Grieve and Shoemaker 1994) suggests that it is possible to distinguish two populations of craters:

1) 8 craters with diameters from 24 to 39 km, the oldest being ~115 Ma

2) 8 craters with diameters from 55 to 100 km, with the oldest being ~370 Ma

The oldest age in each set gives an estimate of the accumulation time. For a proper balance between crater diameter bin width and the number of craters per bin, only two bins for each age sub-population are used to represent the crater production rate. We assume that craters smaller than ~20 km in the younger set and smaller than ~45 km in the older set are depleted by erosion. The poor statistics for terrestrial craters do not help to resolve the production function's shape; however, the terrestrial craters do help to constrain variations in the impact rate.

Figure 5.23 shows cumulative curves recalculated from lunar data for terrestrial craters for crater retention ages of 0.125, 0.36, and 1 Ga. Subsets of the database from Grieve and Shoemaker (1994) for smaller younger craters (the oldest one is 115 Ma) and larger older craters (the oldest one is ~370 Ma) are in a good agreement with properly scaled lunar isochrones. Recently Hughes (2000) published estimates for the terrestrial cratering rate averaged for the last 125 Ma using the "nearest neighbor" approach. This technique results in estimates that are also near (within error limits) model "lunar analogue" curves (Fig. 5.23). Thus, within a factor of 2 (which is close to error bars shown in Fig. 5.23), a reliable first approximation is to assume a constant cratering rate after the end of the heavy bombardment. Previously, the Phanerozoic cratering rate has been assumed to be larger than the average cratering rate for the last 3 Ga (in contrast to approximately constant impact rate). Partially this contradiction is due to a widely accepted concept that the cumulative number of terrestrial craters may be approximated with a simple power law (e.g., Grieve and Shoemaker 1994; Hughes 2000). The simple power law approximation used, for example, by Hughes (2000), with a cumulative exponent of −1.86, is shown as a dashed line in Fig. 5.23. Projecting the data from the crater diameter range of 10 to 50 km to the normative diameter $D = 1$ km can produce misleading results of $N(D = 1)$. Using the lunar like non-power law curve gives less deviation from a constant cratering rate on Earth (and on the Moon) for the last 3 Ga.

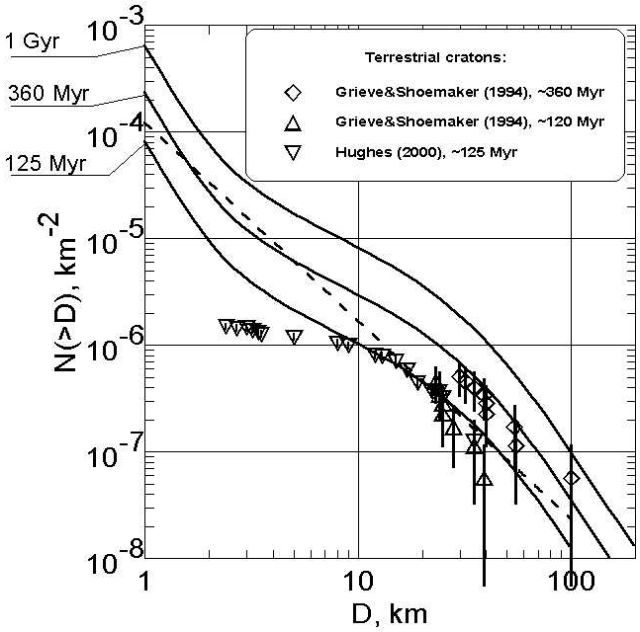

Figure 5.23. Terrestrial cratering data in cumulative form. Data for terrestrial cratons from Grieve and Shoemaker (1994)—area of 17.6 10^6 km^2—are shown as diamonds (for craters younger than ~ 360 Ma) and upward triangles (for craters younger than ~120 Ma). Downward triangles are for estimates by Hughes (2000). Solid curves are isochrones recalculated from lunar data with an account for different gravity and average impact velocity on the Earth. Dashed line illustrates a power law approximation of younger data with an exponent −1.86 used by Hughes (2000).

4. RELATIVE AGE DATING OF LUNAR SURFACE UNITS AND THE LUNAR STRATIGRAPHY

4.1. Principles of relative age dating

Baldwin (1949) provided strong arguments for the impact origin of lunar craters and for the volcanic nature of the mare plains. He also introduced general time relationships based on crater densities and superposition. Following the principles of Gilbert (1893), which were based on telescopic observations, geological mapping of the Moon was pioneered by Shoemaker and Hackman (1962) in preparation of the Apollo program. Lunar Orbiter and Apollo images greatly expanded the telescopic observations and permitted establishment of rock-stratigraphic units.

Lunar mapping and stratigraphy depends on morphologic characteristics, superposition relationships, albedo, and remotely sensed chemical composition of surface units rather than on a detailed examination of rock units and their mutual boundary characteristics. On the Moon, rock-stratigraphic units are primarily understood as morphologically distinct entities formed at a specific time by a defined geological process. Some units, however, remain of uncertain origin, and may have formed over a period of time rather than in a specific event (e.g., the "light plains" in the highlands).

The basic methods and the results of lunar mapping and stratigraphic analysis as derived from telescopic and spacecraft imagery and from the analysis of returned lunar rocks are described comprehensively in Wilhelms et al. (1987). Work on defining the relative ages of

units, their geological and chemical definition, and their formative processes has continued since and progressed with global data obtained from the Clementine and Lunar Prospector missions (e.g., Nozette et al. 1994; Staid et al. 1996; Binder 1998; Jolliff et al. 2000b; Staid and Pieters 2001; Feldman et al. 2002). These missions have also helped to understand more of the third dimension of the lunar crust.

The fundamental method used for relative age dating is the application of the law of superposition. It was apparent that older units recognized this way had more craters than younger units, consistent with the craters being of impact origin. The technique of using crater density as a method of deriving relative ages when superposition relationships were lacking (e.g., non-contacting units) became standard for the Moon and for other planets. The use of size-frequency distributions as measures of relative ages has been long established (reviewed in Hartmann et al. 1981; Wilhelms 1984; Wilhelms et al. 1987; Fig. 5.24).

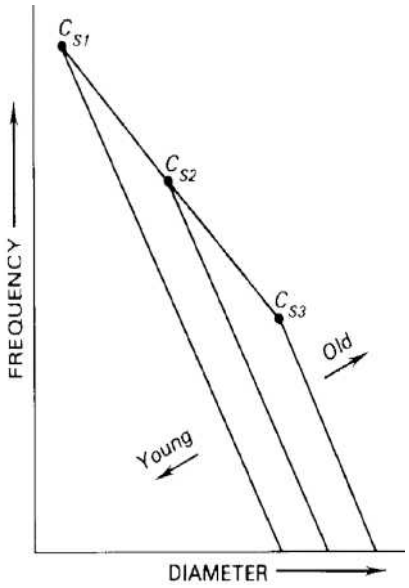

Figure 5.24. Principal graph for age dating of planetary surfaces by cumulative crater frequencies as a function of crater diameter; the kinks in the curves define the parameter C_S which is the transition diameter between the crater production curve (steep) and the crater saturation curve (flat); C_{S1}, C_{S2}, and C_{S3} represent increasing relative crater retention ages; from Wilhelms et al. (1987) (courtesy of the U.S. Geological Society).

The degree of crater degradation is also an indicator of relative age. For a given size, a fresh crater is younger than a degraded one. The overall morphology of craters indicates their relative ages; for instance, older craters are systematically shallower and smoother than younger craters of the same size because of impact erosion. Some erosion-based method is especially needed where the geologic unit of interest is too small for significant crater size-frequency determination. However, several different ways of addressing the morphology of a crater exist. Numerical values such as D_L relate to the size of the largest crater that is nearly destroyed (Soderblom and Lebofsky 1972; Boyce and Dial 1975; Wilhelms 1980). On small surfaces, such a crater will not necessarily be apparent, and D_L is defined as the diameter of craters with the shallow wall slope of 1° (Wilhelms et al. 1987). Despite some pitfalls, this method has been successful and used extensively (Wilhelms et al. 1987; see Table 5.5).

4.2. The lunar stratigraphy

Lunar stratigraphy establishes geologic units and arranges them into a relative time-sequenced column of global significance. A pre-requisite is the identification of rock units or morphological units formed in a single-stage process. Such units are preferably impact basins, impact craters, and lava flows. Morphological units, rather than the exposed bedrock, are necessarily used in photo-based stratigraphy. These units are assembled into higher-order systems, and Rock System boundaries so defined are intended to be the same absolute age everywhere. This chronostratigraphic division (Systems, Series) can be converted into a chronometric division (Periods, Epochs), and with application of radiogenic ages, into absolute time. Figure 5.25 shows these stratigraphic columns, following Wilhelms et al. (1987).

4.2.1. Pre-Nectarian System. The pre-Nectarian System comprises all landforms *older* than the Nectaris basin, and includes about 30 recognized impact basins. Some of these

Table 5.5. Stratigraphic criteria for lunar time-stratigraphic units (after Wilhelms et al. 1987).

System or Series	Crater frequency (number per km²)		C_S (m)	D_L (m)
	≥ 1 km	≥ 20 km		
Copernican System	$< 7.5\times10^{-4}$ (mare) $< 1.0\times10^{-3}$ (crater)	n/a	?	< 165 (mare) < ca. 200 (crater)
Eratosthenian System	$< 7.5\times10^{-4}$ to $\sim 2.5\times10^{-3}$ (mare)	n/a	< 100 (mare)	145–250 (mare)
Upper Imbrian Series	$\sim 2.5\times10^{-3}$ to $\sim 2.2\times10^{-2}$ (mare)	2.8×10^{-5}	80–300 (mare)	230–550 (mare)
Lower Imbrian Series	~ 2.2–4.8×10^{-2} (basin)	1.8–3.3×10^{-5}	320–860 (basin)	n/a
Nectarian System	n/a	2.3–8.8×10^{-5}	800–4000(?) (basin)	n/a
Pre-Nectarian System	n/a	$> 7.0\times10^{-5}$	> 4000(?) (basin)	n/a

D_L: diameter of largest crater eroded to 1° interior slopes; C_S: limiting crater diameter for the steady state crater frequency distribution (Fig. 5.24) and from the approximate formula; $\boldsymbol{D_L} = 1.7\ \boldsymbol{C_S}$; n/a = not applicable.

landforms directly underlie deposits of Nectaris, and others are recognized as pre-Nectarian by the size-frequency curves of superposed craters (Fig. 5.26; Table 5.5). The oldest recognized basin is Procellarum, but this basin may not be of impact origin. The oldest basin of clear impact origin is South Pole-Aitken, which is also the deepest and the largest (Spudis 1993). The pre-Nectarian landforms are dominantly of impact origin; no volcanic landforms or tectonic features have been recognized. Pre-Nectarian terrain is predominant on the lunar farside (Fig. 5.27). Any rocks from such ancient terrains in the Apollo or Luna sample collections have been reworked as fragmental material into later impact-breccia deposits.

4.2.2. Nectarian system. The Nectarian System includes all landforms produced between the formation of the Nectaris impact basin and the formation of the Imbrium impact basin. Nectaris itself has deposits over a fairly wide area. Eleven other Nectarian basins have been recognized, including Serenitatis and Crisium (Fig. 5.26). Direct superpositional relationships allow some definition of their stratigraphic sequence, but some crater frequency distributions have been affected by later basins, e.g., Serenitatis ejecta is badly degraded by Imbrium ejecta. Nectarian "light plains" are more evident than are pre-Nectarian ones, and some of these have been suggested to be volcanic in origin (Fig. 5.28; Wilhelms et al. 1987). The Nectarian System has been masked by the Imbrian basins and later volcanic activity; thus, it is much more common on the lunar farside (Fig. 5.27). More recent studies of the relative and absolute ages of lunar mare basalts (Hiesinger et al. 2003) suggest that mare volcanism started already during the Nectarian Period (assuming a 3.92 Ga age of Nectaris, see below). Basaltic volcanism continued throughout all later Periods and ended around 1.2 Ga ago (Hiesinger et al. 2003) within the Eratosthenian or even Copernican Period depending on the assumed age for the Eratosthenian-Copernican boundary, which is either around 1.5 to 2 Ga or near 0. 8 to 1 Ga (see discussion in Stöffler and Ryder 2001 and Hiesinger et al. 2003, and in Section 6).

4.2.3. Lower Imbrian Series. The Lower Imbrian Series comprises all landforms produced between the formation of the Imbrium impact basin and the formation of the Orientale impact basin (Table 5.5). The deposits of these two basins constitute extensive, laterally continuous

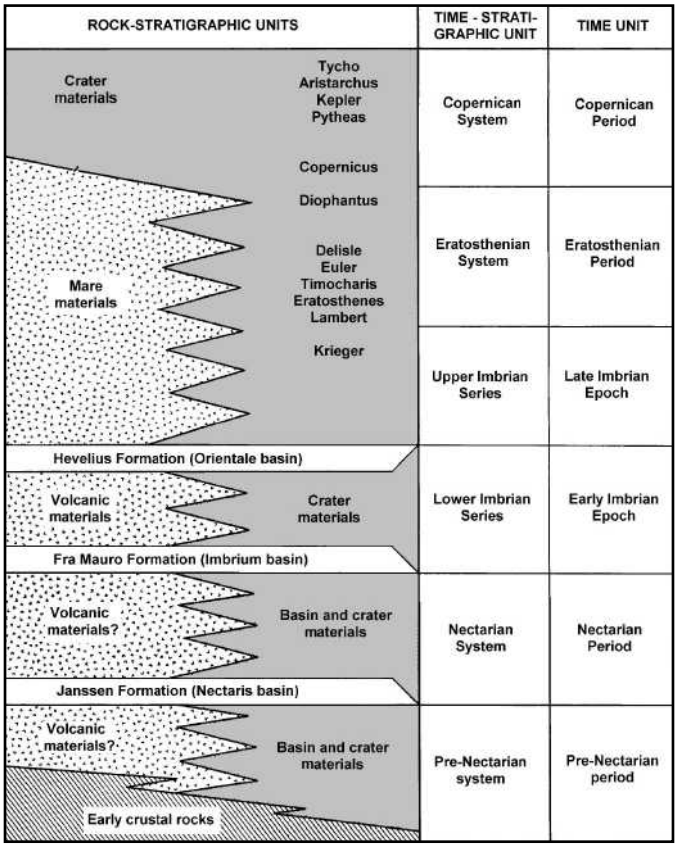

Figure 5.25. The lunar stratigraphic column with rock-stratigraphic, time-stratigraphic and time units (from Wilhelms et al. 1987, courtesy of the U.S. Geological Society).

horizons, although much of the Imbrium basin itself was later flooded with mare lavas. Crater counts as well as its topographic freshness suggest that the Schrödinger basin and its ejecta is Lower Imbrian, but no other basins are in the Lower Imbrian. The size-frequency distribution curve for Orientale deposits lies slightly below that for Imbrium, and both are distinctly below the curve for Nectaris basin deposits (Fig. 5.26). Many "light plains", including the Cayley plains on which Apollo 16 landed, have a Lower Imbrian age (Fig. 5.28), and many may be related to the Imbrium basin. A volcanic origin has also been proposed for at least some light plains, despite the absence of volcanic rocks in the Apollo 16 samples. The Apennine Bench formation, a plains unit within the Imbrium basin, may be a volcanic unit, as it correlates chemically with samples of volcanic KREEP basalt collected at the Apollo 15 landing site.

4.2.4. Upper Imbrian Series. The Upper Imbrian Series includes the landforms produced between the formation of Orientale, the youngest impact basin, and an upper boundary that is defined on the basis of D_L values (Table 5.5). The Upper Imbrian rock units are distinct from older ones: basin deposits are lacking, and two-thirds of the mare volcanic plains are in the Upper Imbrian (Fig. 5.29). The Upper Imbrian was emplaced over a much longer time period than the Lower Imbrian. The extensive mare lavas forming Maria Serenitatis, Tranquillitatis, Crisium, Nectaris, Fecunditatis, Humorum, Nubium, Cognitum, eastern Imbrium, and western Oceanus Procellarum, and several other areas including all the farside mare plains, are part

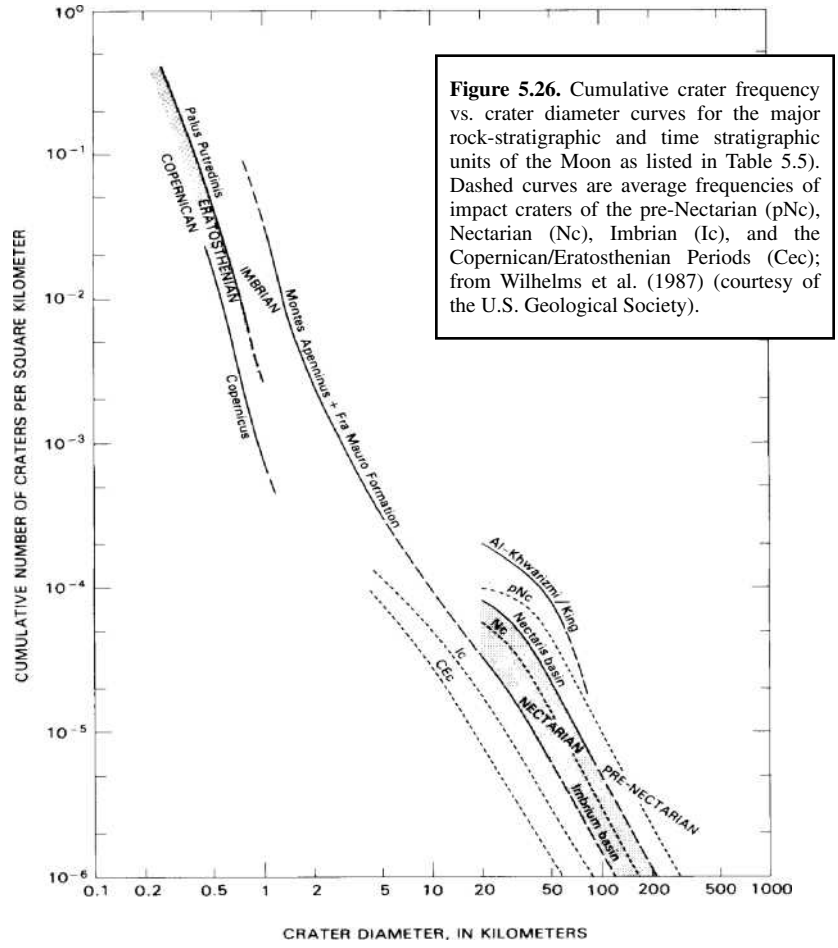

Figure 5.26. Cumulative crater frequency vs. crater diameter curves for the major rock-stratigraphic and time stratigraphic units of the Moon as listed in Table 5.5). Dashed curves are average frequencies of impact craters of the pre-Nectarian (pNc), Nectarian (Nc), Imbrian (Ic), and the Copernican/Eratosthenian Periods (Cec); from Wilhelms et al. (1987) (courtesy of the U.S. Geological Society).

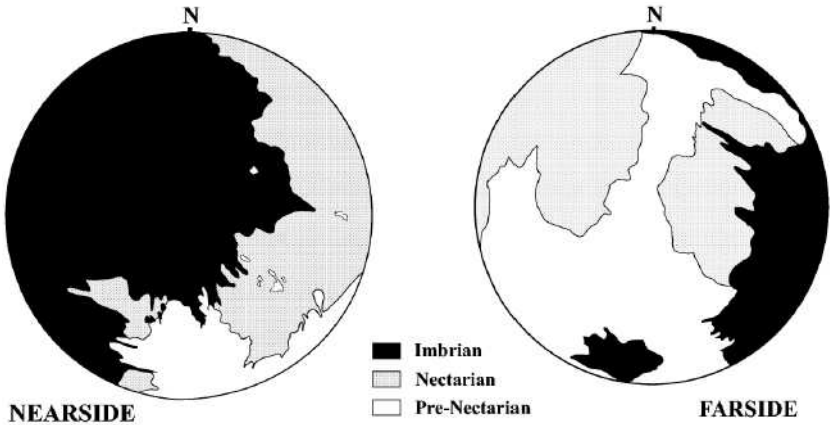

Figure 5.27. Geologic map of the nearside and farside of the pre-Eratosthenian Moon showing the Imbrian, Nectarian, and pre-Nectarian Systems (compiled from Plates 3A and 3B of Wilhelms et al. 1987, courtesy of the U.S. Geological Society).

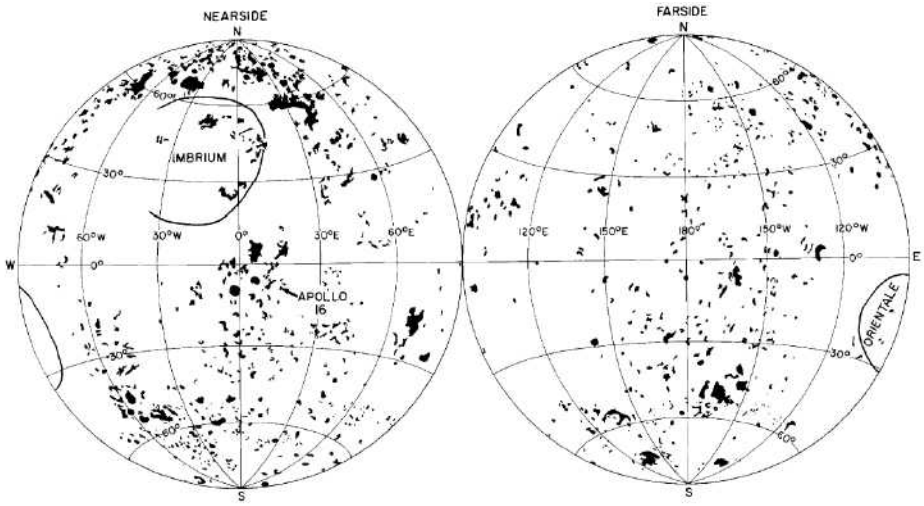

Figure 5.28. Geologic map of the distribution of "light plains" on the nearside and farside of the moon (from Wilhelms et al. 1987, courtesy of the U.S. Geological Society).

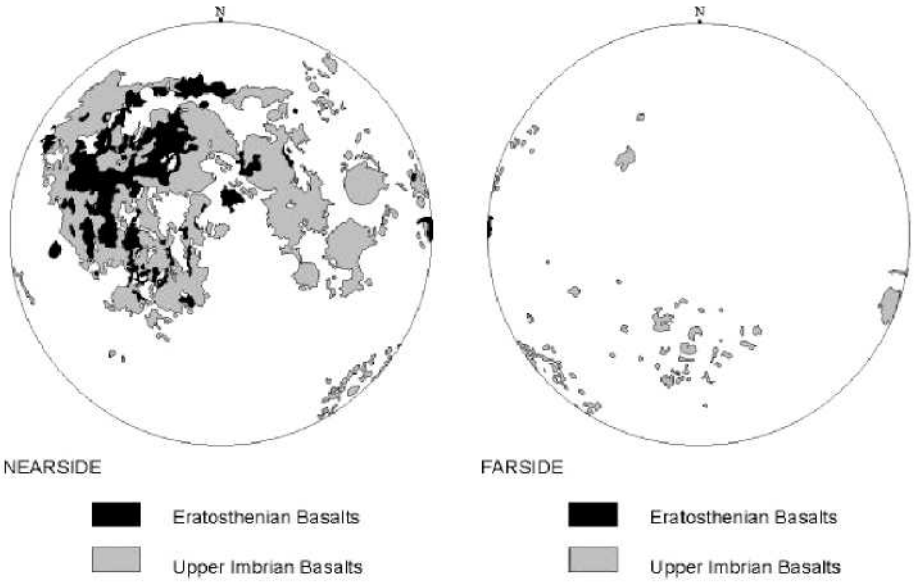

Figure 5.29. Geologic map of mare basalts of the Upper Imbrian Epoch and the Eratosthenian Period on the nearside and farside of the moon; compiled from Plates 9 A,B and 10 A,B of Wilhelms et al. (1987) (courtesy of the U.S. Geological Society).

of the Upper Imbrian Series (Fig. 5.29). Their relative ages have been established on the basis of crater frequencies and by superposition, and their stratigraphic relationships have been elucidated with mineral-chemical data derived from Earth-based spectral reflectance observations and from the Clementine and Lunar Prospector orbital data (e.g., Staid et al. 1996; Jolliff et al. 2000b; Staid and Pieters 2001; Hiesinger et al. 2003). The Upper Imbrian also contains "dark mantling deposits" that have been correlated with volcanic glass of fire-fountain origin, examples of which have been sampled by the Apollo missions, notably the Apollo 15 green glass and the Apollo 17 orange glass. With the exception of the Apollo 12 mission, all mare plains sampled by Apollo and Luna were Upper Imbrian, and no samples were from the Lower Imbrian Series.

4.2.5. Eratosthenian System. The Eratosthenian System is less clearly defined than other systems (Table 5.5). Its upper boundary is even more ambiguous than the lower boundary. Formally the distinction between the Eratosthenian and the subsequent Copernican systems was made according to whether a crater was non-rayed (Eratosthenian) or bright-rayed (Copernican). Eratosthenes itself lacks rays, and Copernicus has bright rays, but according to Stöffler and Ryder (2001) neither crater defines either the base or the top of its eponymous system, instead lying within it. However, the presence of rays depends not only on age, that is degree of impact erosion, but also on crater size and on compositional differences between the impacted target and the region of ejecta deposition. For such reasons a distinction should be made between "compositional" and "maturity" rays which may have different lifetimes (Grier et al. 2001). In any case, superposition on rays of Copernicus establishes a Copernican age. Crater counts on ejecta blankets of Copernican craters are of limited use because most craters are too small for good statistics. The same limited-area constraint applies to D_L (~140 m) as well, and there is the further problem that D_L requires a flat surface, restricting measurements to the small, interior impact-melt region of a crater. Other criteria have been used including infrared (Copernican craters are hotter) and radar (blockier). A new parameter of optical maturity derived from global orbital spectral reflectance measurements from the Clementine spacecraft (Chapter 2) is a promising candidate for a more rigorous determination of relative ages of Copernican and upper Eratosthenian craters.

The Eratosthenian System includes mare plains that are much less extensive than Upper Imbrian plains. They are absent from the lunar farside (other than Mare Smythii on the limb; Fig. 5.29). The plains include those sampled at the Apollo 12 landing site in Oceanus Procellarum. None of the dark mantling volcanic-glass deposits appears to be Eratosthenian. Eratosthenian mare and crater deposits interfinger on much of the central and western nearside of the Moon, enabling a detailed relative stratigraphy to be derived. However, these show that some mare plains traditionally mapped as Eratosthenian embay bright-rayed craters, which must then be assigned to the Eratosthenian, meaning that not all rayed craters must be Copernican.

4.2.6. Copernican System. The Copernican System was first recognized by the rays of its craters, which were shown to be the youngest of lunar features because the are superposed on all other terrains (Table 5.5). Despite the difficulty of using rays in defining a lower boundary (see above), most rayed craters are indeed Copernican, and such craters are scattered all over the Moon. The upper boundary of the Copernican is the present day. Only a very small proportion of the Moon's face is Copernican, although the landscape effects can be global: The rays of Tycho stretch almost around the entire Moon. There are only half as many Copernican craters in any given size range as there are in the Eratosthenian (44 larger than 30 km, cf. 88 in the Eratosthenian). Some patches of mare basalt do overlap rayed craters, and on the basis of craters counts also seem to be Copernican in age (e.g., Schultz and Spudis 1983), mainly in northern Oceanus Procellarum. This interpretation depends, of course, on the definition and absolute age of the lower boundary of the Copernican system (e.g., Hiesinger et al. 2003, and discussion above).

5. GEOLOGIC PROVENANCE AND RADIOMETRIC AGES OF LUNAR ROCKS

5.1. Geologic provenance and stratigraphic significance of lunar samples

Six manned Apollo missions and three robotic Luna missions returned samples from different geologic settings on the Moon (Fig. 5.1, Table 1.1). More than 30 distinct meteorites are recognized as being of lunar origin (Meteoritical Bulletin 2004; <*http//epsc.wustl.edu/admin/resources/meteorites/moon_meteorites_list.html*>). The missions provided samples of basaltic rocks and glasses from mare terrain (Apollo 11, 12, 15, and 17; Luna 16, 24) and impactites (polymict breccias, impact-melt lithologies, and granulitic lithologies) from highland terrain (Apollo 14, 15, 16, 17; Luna 20). The lunar meteorites are derived from unknown locations in the mare as well as highland regions. The proportions of mare and highland derived meteorites indicates that they most likely represent the whole surface of the Moon.

It is obvious that the highland samples are highly processed by multiple impact cratering events. In relation to the primary igneous highland rocks (anorthosite, norite, gabbro, troctolite, dunite) the vast majority of returned samples represent second or third generation rocks. Moreover, thermally processed rocks occur as granulitic rocks and granulitic breccias whose compositions indicate polymict (anorthositic-noritic) precursors.

According to the different types of rocks—igneous rocks, crystalline impact-melt rocks and impact glasses, thermally metamorphosed rocks (granulitic lithologies) and polymict clastic matrix breccias (Table 5.6–5.8; Stöffler et al. 1980; Heiken et al. 1991)—different types of ages can be obtained by radiogenic isotope dating. These include (1) *crystallization ages* defining either magmatic, impact melting or recrystallization events, (2*) impact breccia formation ages* defining the time of the assembly and deposition of a polymict breccia, and (3) *exposure ages* defining the time since which an impact-displaced rock fragment has been exposed to cosmic rays. Concerning methods of radiogenic isotope dating, we refer to the literature (e.g., Faure 1986; Dalrymple 1991). General reviews of the results of lunar chronology have been provided by Turner (1977), Dalrymple (1991), Nyquist and Shih (1992), and Snyder et al. (2000), among others.

Radiometric ages of the different types of lunar samples are of very different geological significance which can only be derived by a careful textural analysis of the samples and their geologic setting with respect to a specific formation defined by photogeologic techniques. This hold particularly for all types of polymict rocks (breccias, impact melts). In principle, direct age dating of a parent geologic formation is only possible for mare basalts. Radiometric ages of igneous highland rocks cannot be related to any corresponding geologic surface formation on the Moon. There is the additional problem that none of the rock samples was collected directly from a bedrock unit as the entire lunar surface is covered with impact-produced regolith at least several meters thick. Consequently, the interpretation problems are different for the different types of rocks:

Volcanic rocks of mare provenance. Even for the comparatively simple case of a volcanic rock, it is not necessarily easy to relate that rock to a mapped geological unit. At any given mare collection site there is a range of basalt types—brought to the surface by multiple reworking of the regolith—that in some cases covers a distinct range of ages. While the youngest of these is most likely the age of the surface unit, if that unit is thin or discontinuous it might not be the surface that is mapped and which retains the crater density/crater degradation characteristics used to define the age of the unit in question.

Impact melt and clastic breccia lithologies of highland provenance. Radiometric age dating of impact-melt rocks is generally possible by direct dating of the glassy or crystalline matrix. However, since datable impact-melt rocks are either displaced individual clasts

Table 5.6. Radiogenic crystallization ages (Gyr) for igneous lunar highland rocks.

Sample[1]			^{40}Ar-^{39}Ar*	Rb-Sr	Sm-Nd	U-Pb, Pb-Pb
Ferroan Anorthosite		22013,9002	4.51 ± ?			
		60025			4.44 ± 0.02	4.51 ± 0.01
		67016 cl			4.56 ± 0.07	
		62236			4.36 ± 0.03	
		67435;33a cl	4.35 ± 0.05			
		67435;33b cl	4.33 ± 0.04			
Magnesian Suite Plutonic Rocks	*Troctolite*	76535	4.19 ± 0.02 4.16 ± 0.04 4.27 ± 0.08	4.51 ± 0.07	4.26 ± 0.06	4.27 ± ?
		14306,150 (?)				4.245 ± 0.075
	Dunite	72417		4.47 ± 0.10		
	Norite	14305;91 (?)				4.211 ± 0.005
		15445;17			4.46 ± 0.07	
		15445;247			4.28 ± 0.03	
		15455;228		4.49 ± 0.13	4.53 ± 0.29	
		72255		4.08 ± 0.05		
		73215;46,25	4.19 ± 0.01			
		77215		4.33 ± 0.04	4.37 ± 0.07	
		78235				4.426 ± 0.065
		78236	4.39 ± ? 4.11 ± 0.02	4.29 ± 0.02	4.43 ± 0.05 4.34 ± 0.04	
	Gabbro-norite	67667			4.18 ± 0.07	
		73255c			4.23 ± 0.05	
Alkali Rocks		14066;47 (?)				4.141 ± 0.005
		14304 cl b			4.34 ± 0.08[a]	4.108 ± 0.053
		14306;60 (?)				4.20 ± 0.03
		14321;16 c				4.028 ± 0.006
		67975;131				4.339 ± 0.005
KREEP Basalt (KB) and Quartz Monzogabbro (QM)	*A15 KB*	15382	3.84 ± 0.05 3.85 ± 0.04	3.82 ± 0.02		
		15386		3.86 ± 0.04	3.85 ± 0.08	
	A17 KB	15434 particle		3.83 ± 0.05		
		72275		3.93 ± 0.04		
				4.04 ± 0.08	4.08 ± 0.07	
	QM	15405,57				4.297 ± 0.035
		15405,145				4.309 ± 0.120
Granite and Felsite		12013		> 4.08		
		12033,507				3.883 ± 0.003
		12034,106				>3.916 ± 0.17
		14082,49				4.216 ± 0.007
		14303 cl				4.308 ± 0.003
		14311, 90				4.250 ± 0.002
		14321 B1 (cl?)	K-Ca:			4.010 ± 0.002
		14321 cl	4.060 ± 0.071	4.04 ± 0.03	4.11 ± 0.20	3.965 ± 0.025
		72215 mix		3.95 ± 0.03		
		73215,43		3.82 ± 0.05		
		73235,60				4.218 ± 0.004
		73235,63				4.320 ± 0.002
		73235,73				>4.156 ± 0.003

Notes: [1] including split number if given by author; * only given if suggestive of crystallization age; [a] disturbed and suspect; cl = clast; (?) uncertain split number

Decay constants from Steiger and Jäger (1977); for references see Papike et al. (1998); from Stöffler and Ryder (2001).

within the lunar regolith or displaced clasts residing in polymict breccias, it is not obvious what geologic unit they were excavated from and what impact crater they represent. For polymict clastic impact-breccia deposits, *the age can only be constrained to be younger than that of the youngest clast.* For ancient clastic breccia deposits produced at times when the impact rate was high, the youngest clast is likely to be very close to the assembly age. Complete or partial resetting of clasts is possible for clasts residing in impact-melt breccias. In this case, the oldest clast gives a lower limit for the age of the precursor rocks of the impact melt unit (e.g., Jessberger et al. 1977). For all types of highland rocks, a meaningful interpretation of their geologic provenance and the correlation with a time-stratigraphic unit can only be made on the basis of photogeologic models of their parent geologic formations (see Section 6).

5.2. Radiometric ages of lunar rocks

Radiogenic isotope ages of lunar rocks have been determined on numerous rocks collected at the Apollo and Luna landing sites as individual fragments or as clasts within polymict breccias, and for lithic and mineral fragments extracted from lunar meteorites. The data are from several different methods, especially Rb-Sr and Sm-Nd isochron and Ar^{40}-Ar^{39} stepwise-heating methods. The data of relevance are those which directly date or indirectly constrain the age of morphological units. In particular these are crystallization ages for volcanic rocks and impact melts. It is beyond the scope of this paper to provide a complete compilation of all available data. The reader is referred to review papers and data compilations (e.g., Dalrymple 1991; Heiken et al. 1991; Nyquist and Shih 1992; Papike et al. 1998; Nyquist et al. 2001; Snyder et al. 2000). The use of these ages in dating specific surfaces and units is discussed in Section 6.

Ages of specific plutonic and volcanic ancient highlands igneous rocks are listed in Table 5.6, which is a fairly complete list of available data, including ancient mare basalts. Most of these ages are inferred to be crystallization ages. They can rarely be used to directly date a geologic unit, but can provide a lower limit in some cases.

Crystallization and recrystallization ages for clasts in specific polymict highlands rocks, mainly impact melts and granulitic breccias, are listed in Table 5.7. This is a representative list, but not complete. Most of these samples are fine grained, leading to the dominance of Ar^{40}-Ar^{39} ages. Few of these ages directly date specific geologic units as discussed in Sections 2 and 6. Some impact-melt rocks, for example at Apollo 17, may directly date impact basins on the basis of geological relationships, in this case, Serenitatis. Clasts in breccia units constrain the ages of such units by being enclosed in them. Some of the samples have been inferred to be ejecta from large craters such as Copernicus (e.g., at Apollo 12), and reheated by those events, providing a means of dating them.

Ages for groups of mare basalts are listed in Table 5.8. Unlike Tables 5.6 and 5.7, these ages are not for specific samples but are best estimates for groups, because chemistry, isotopes, and petrography allow the definition of multiple samples as from a single event and single units. More than one basalt group, with at least some differences in age, exists at each landing site; thus geological arguments are needed to establish which represents best the age of the surface on which crater counts have been established.

A separate group of ages consists of exposure ages, dating when the surface of a sample was exposed to cosmic and solar rays. Such dating is limited to rim deposits of young Copernican craters at the Apollo landing sites, such as North Ray and South Ray Craters (Apollo 16), and Cone Crater (Apollo 14), or to the landslide and secondary cratering at the Apollo 17 site inferred to be from Tycho. Others again reflect purely local events of no great stratigraphic significance in the context of this paper.

Table 5.7. Representative radiogenic crystallization ages (Gyr) for polymict lunar highland rocks.

Sample*		Description	^{40}Ar–^{39}Ar	Rb–Sr
Fragmental Breccias	14064,31	KREEP melt clast	3.81 ± 0.04	
	67015,320	feldspathic melt blobs	3.90 ± 0.01	
	67015,321	VHA melt blob	3.93 ± 0.01 (K-Ar)	
Glassy Breccias and Glass	61015,90	coat	1.00 ± 0.01	
	63503 particle 1m	glass fragment	2.26 ± 0.03	
	67567,4	slaggy bomb	0.84 ± 0.03	
	67627,11	slaggy bomb	0.46 ± 0.03	
	67946,17	slaggy bomb	0.37 ± 0.04	
Crystalline Melt Breccias	14063,215	poikilitic impact melt	3.89 ± 0.01	
	14063,233	aphanitic impact melt	3.87 ± 0.01	
	14167,6,3	melt	3.82 ± 0.06	
	14167,6,7	melt	3.81 ± 0.01	
	15294,6	poikilitic, Gp. Y	3.87 ± 0.01	
	15304,7	ophitic, Gp. B	3.87 ± 0.01	
	15356,9	poikilitic, Gp. C	3.84 ± 0.01	
	15356,12	poikilitic, Gp. C	3.87 ± 0.01	
	60315,6	poikilitic	3.88 ± 0.05	
	63503 particle 1c	very high-Al?	3.93 ± 0.04	
	65015	poikilitic	3.87 ± 0.04	3.84 ± 0.02
	65785	ophitic	3.91 ± 0.02	
	72215,144	aphanite, felsite melts	3.83 ± 0.03	
	72255	aphanite, felsite melts	3.85 ± 0.04	
	72215,238b	aphanite	3.87 ± 0.02	
	73215	aphanite, felsite melts		3.84 ± 0.05
	77075,18	veinlet (Serenitatis)	3.93 ± 0.03	
	72395,96	poikilitic (Serenitatis)	3.89 ± 0.02	
	72535,7	poikilitic (Serenitatis)	3.89 ± 0.02	
	76055	magnesian, poikilitic	3.92 ± 0.05	
	76055,6	magnesian, poikilitic	3.78 ± 0.04	3.78 ± 0.04
Clast-poor Impact Melts	14073	subophitic 14310 group		3.80 ± 0.04
	14074	subophitic 14310 group	3.80 ± 0.04	
	14276	subophitic 14310 group		3.80 ± 0.04
	14310	subophitic	3.88 ± 0.05	3.79 ± 0.04
	14310	subophitic; plag	3.82 ± 0.04	
	65795	subophitic; very feldspathic		3.81 ± 0.04
	60635	subophitic 68415 group		3.75 ± 0.03
	65055	subophitic 68415 group	3.89 ± 0.02	
	67559	subophitic 68415 group		3.76 ± 0.04
	68415	subophitic	3.80 ± 0.06	3.76 ± 0.04
	68416	subophitic 68415 group		3.71 ± 0.02
Granulitic Breccias and Granulites	14063,207		3.90 ± 0.02	
	14179,11	clast	3.97 ± 0.01	
	15418,50		3.98 ± 0.06	
	67215,8		3.75 ± 0.11	
	67415		3.96 ± 0.04	
	67483,13,8		4.20 ± 0.05	
	72255,235b	clast	3.85 ± 0.02	
	77017,46		3.91 ± 0.02	
	78155		4.16 ± 0.04	
	78527		4.15 ± 0.02	
	79215		3.91 ± ?	

* including split number if given by authors

Decay constants from Steiger and Jäger (1977); for references see Papike et al. (1998); from Stöffler and Ryder (2001).

Table 5.8. Best estimates of crystallization ages of mare basalt flows at the Apollo and Luna landing sites.

Landing Site	Basalt Group	Absolute Age (Gyr)
Apollo 11	High-K basalts	**3.58 ± 0.01**
	High-Ti basalts, groups B1,3	3.70 ± 0.02
	High-Ti basalts, group B2	**3.80 ± 0.02**
	High-Ti basalts, group D	3.85 ± 0.01
Apollo 12	Olivine basalt	3.22 ± 0.04
	Pigeonite basalt	3.15 ± 0.04
	Ilmenite basalt	3.17 ± 0.02
	Feldspathic basalt	3.20 ± 0.08
Apollo 15	Ol-normative basalt	**3.30 ± 0.02**
	Qz-normative basalt	3.35 ± 0.01
	Picritic basalt	3.25 ± 0.05
	Ilmenite basalt (15388)	3.35 ± 0.04
	Green glass	~3.3 – 3.4
	Yellow glass	3.62 ± 0.07
Apollo 16	Feldspathic basalt	3.74 ± 0.05
Apollo 17	High-Ti basalt, group A	**3.75 ± 0.01**
	High-Ti basalt, group B1,2	3.70 ± 0.02
	High-Ti basalt, group C	**3.75 ± 0.07**
	High-Ti basalt, group D	3.85 ± 0.04
	Orange glass	~3.5 – 3.6
Luna 16	Aluminous basalt	3.41 ± 0.04
Luna 24	Very-low-Ti basalt (VLT)	**3.22 ± 0.02**
Lunar meteorite Asuka 881757	Basalt (gabbroic)	3.87 ± 0.06

Data compiled from various sources; see especially Snyder et al. (2000), Burgess and Turner (1998), Nyquist and Shih (1992); Dalrymple (1991), Spangler et al. (1984), and references therein. Proposed ages for surface flows (crater retention ages) are given in bold (see Table 5.10); from Stöffler and Ryder (2001).

6. GEOLOGY AND ABSOLUTE AGES OF LUNAR SURFACE UNITS

6.1. Pre-Nectarian Period

The pre-Nectarian Period as a time unit is the time span between the origin of the Moon and the formation of the Nectaris basin, which is most plausibly ~3.92 Ga old (see next section). Since the oldest plausible age of solid lunar surface material is 4.52 Ga (Lee et al. 1997; Halliday 2000), a duration of the pre-Nectarian Period of ~600 Ma is suggested. The pre-Nectarian system is recorded by (1) the impact formations of some 30 multiring basins and their ejecta deposits identified photogeologically, and (2) returned samples of rocks whose absolute ages are older than Nectaris (see Table 5.6). The suite of "plutonic" pre-Nectarian rocks comprises ferroan anorthosites, alkali anorthosites, and rocks of the magnesian suite (troctolites, norites, dunites, and gabbronorites). Clasts of aluminous mare basalts, rare clasts of impact-melt rocks, and granulitic lithologies also display pre-Nectarian ages. All these rock types document the existence of magmatic, thermal metamorphic, and impact processes throughout the pre-Nectarian Period. None of the dated pre-Nectarian rock clasts can be directly related to the geologic unit (formation) in which they formed or to any specific pre-Nectarian surface unit because they were all displaced after their formation by multiple impacts.

The relative ages of most of the pre-Nectarian multiring basins are documented on the basis of crater counts on their ejecta formations (Table 5.9). Wilhelms et al. (1987) distinguished nine age groups in which the density of craters > 20 km per 10^6 km² increases from 79 (Nectaris) to 197 (Al-Khwarizimi/King). In the Wilhelms et al. (1987) scenario, no multiring basins older than 4.2 Ga are unequivocally recorded, thus implying that the oldest basins, South Pole-Aitken and Procellarum, and some 14 obliterated basins, formed between 4.2 Ga and 4.1 Ga. However, these ages are speculative as long as the actual age of the oldest recognizable multiring basin (i.e., South Pole-Aitken) is not determined by isotope dating of returned samples.

6.2. Nectarian Period

Twelve multiring basins of Nectarian age have been identified (Wilhelms et al. 1987; Spudis 1993; Table 5.9). The superposed crater densities (craters > 20 km per 10^6 km²) on the ejecta formations of these basins range from 31 for Bailly to 79 for Nectaris. Ejecta are inferred to have been sampled at Apollo and Luna landing sites for Nectaris, Crisium, and Serenitatis (Apollo 16, Luna 20, and Apollo 15 and 17, respectively). Attempts to assign absolute ages to these basins are based on samples from these landing sites (Table 5.10).

6.2.1. Age of the Nectaris impact basin. The age of the Nectaris basin is derived from radiometric ages of Apollo 16 samples (Table 5.10). The landing site was on the Cayley Formation, representing subdued smooth "light plains," Lower Imbrian Series, sculpted by the Imbrium event (Figs. 5.26, 5.28, and 5.30), and most likely part of its discontinuous ejecta. The site is 60 km west of the Kant Plateau, which is part of the Nectaris basin rim deposits (Fig. 5.30). It is near to the hilly and furrowed Descartes Formation (Muehlberger et al. 1980), which is probably related to the Nectaris ejecta blanket. Light plains similar to the Cayley Formation are common around the Imbrium basin outside of the Fra Mauro Formation (Fig. 5.28).

The local stratigraphy of the Apollo 16 landing site defines two major superimposed formations (Ulrich et al. 1981): the older *Descartes Formation* and the younger surficial *Cayley Formation* exposed as reworked regolith at the whole landing site. The sampling took advantage of two young, fresh craters, North Ray (1 km wide, 230 m deep) and South Ray (680 m, 135 m deep), as well as Stone Mountain and the subdued plains, to obtain materials from both major formations (Fig. 5.30). North Ray Crater is inferred to have excavated rocks that are part of the continuous ejecta blanket of Nectaris (Stöffler et al. 1981, 1985; Wilhelms et al. 1987). The samples collected are dominantly friable feldspathic fragmental breccias and impact melt lithologies with variable textures and compositions from very feldspathic to mafic (aluminous basaltic). Anorthosites, mostly cataclastically brecciated, are common as both individual rocks and as clasts in polymict breccias; feldspathic granulitic rocks and breccias are common, mainly as clasts within breccias. The basin ejecta model of Haskin (Haskin et al. 2002) suggests that the Nectaris, Serenitatis, and Imbrium events each would have contributed significant ejecta deposits to the Apollo 16 site. They estimated that the last of the deposits, i.e., the one produced by the Imbrium event, would have consisted on average of sub-equal proportions of Imbrium and Serenitatis ejecta, less of Nectaris ejecta, plus pre-Nectarian substrate, with only minor contributions from Humorum, Crisium, and later, Orientale. Additional complexities and observations from terrestrial craters that bear upon this model are discussed in Section 7.

In the ejecta of North Ray Crater, highly feldspathic fragmental breccias are most abundant. Lithic clasts, both individual rock fragments of the regolith and clasts within feldspathic fragmental breccias, provide the most reliable age constraints for the Descartes Formation and hence for the age of Nectaris basin (Maurer et. 1978; Jessberger 1983; Wacker et al. 1983; Stöffler et al. 1985). Their ages range from 3.84 Ga to 4.14 Ga. Since the youngest clast determines the age of the polymict impact breccia forming the basement of North Ray Crater, an age as young as 3.85 ± 0.05 Ga has been proposed for the Nectaris basin (Stöffler et al. 1985; Table 5.10). This age may also be supported by the age distribution of lithic clasts of the

Table 5.9. Tabulation of lunar time-stratigraphic units with multi-ring basins (rock-stratigraphic units) and correlated values for the frequency of superimposed craters; modified from Wilhelms et al. (1987).

Time-stratigraphic unit	Rock-stratigraphic unit			Crater frequency
	Basin	Diameter (km)	Age group	Number of craters > 20 km per 10^6 km^2
Pre-Nectarian System	Procellarum	3,200	1	---
	South Pole-Aitken	2,500	1	---
	Tsiolkovsky-Stark	700	2	---
	Grissom-White	600	2	---
	Insularum	600	2	---
	Marginis	580	2	---
	Flamsteed-Billy	570	2	---
	Balmer-Kapteyn	550	2	---
	Werner-Airy	500	2	---
	Pingré-Hausen	300	2	---
	Al-Khwarizimi / King	590	2	197
	Fecunditatis	990	3	---
	Australe	880	3	(> 212)
	Tranquillitatis	800	3	---
	Mutus-Vlacq	700	3	225
	Nubium	690	3	---
	Lomonosov-Fleming	620	3	177
	Ingenii	650	4	162
	Poincare	340	4	(190)
	Keeler-Heaviside	780	4	186
	Coulomb-Sarton	530	5	(145)
	Smythii	840	5	166
	Lorentz	360	6	159
	Amundsen-Ganswindt	355	7	(108)
	Schiller-Zucchius	325	7	(112)
	Planck	325	7	(110)
	Birkhoff	330	7	127
	Freundlich-Sharonov	600	8	129
	Apollo	505	9	119
	Grimaldi	430	9	(97)
Nectarian System	Nectaris	860	1	79
	Mendel-Rydberg	630	(1)	(73)
	Moscoviense	445	1	87
	Korolev	440	1	79
	Mendeleev	330	(2)	63
	Humboldtianum	700	2	62
	Humorum	820	2	56
	Crisium	1,060	2	53
	Serenitatis	740	(2)	(83)
	Hertzsprung	570	2	58
	Sikorsky-Rittenhouse	310	(2)	(27)
	Bailly	300	(2)	(31)
Lower Imbrian Series	Imbrium	1160	---	28
	Schrödinger	320	---	(20)
	Orientale	930	---	22

( ) uncertain values; note that the definition of the diameter for impact basins is controversial (values proposed by Wieczorek and Phillips (1999) are smaller than those given here).

Table 5.10. Cumulative crater frequencies, crater degradation values D_L, and absolute ages of lunar surface units derived from isotope ages of lunar rocks; data are taken from literature from Stöffler and Ryder (2001).

Formation	D_L (m)(1,2)	Crater density, normalized to ave. Mare[a] (2)	N=10^{-3} craters >4 km/km^2 (2)	N=10^{-4} craters >1 km/km^2 (1)	N=10^{-4} craters >1 km/km^2 (3)	N=10^{-6} craters >10 km/km^2 (3)	Age (Gyr) (2,3)	Age (Gyr) new set a (4)	Age (Gyr) new set b (5,6)
Ancient highlands (older crust)	1150 ±200	10–36	564–677		3600 ±1100	920	4.3–4.55 4.35±0.10	?	?
Uplands		7–30	132–564				4.0-4.4	?	?
Nectaris Basin	?	16			1200 ±400	310	4.10±0.10	3.92±0.03	3.92±0.03 3.85±0.05
A16/Descartes Fm					340±70	87	3.90±0.10	3.92±0.03	3.92±0.03 3.85±0.05
Crisium Basin	?	?			570#	145#		3.89±0.02	3.84±0.04
Serenitatis Basin	?	?			?	?	3.98±0.05	3.89±0.01	3.87±0.03
A16/Cayley Fm.	550±50	4.0	34.7					3.85±0.02	3.77±0.02
Imbrium Apennines	350±30	3.0		250–480	?	89	3.91±0.10	3.85±0.02	
A14/Fra Mauro Fm.	350±30	2.8–3.0	47.7	250–480	370±70	94#	3.91±0.10	3.85±0.02	3.77±0.02
Imbrium Basin							3.91±0.10	3.85±0.02	3.77±0.02
Orientale ejecta blanket	500±100	2.50	ND	220	220±?			ND	ND
Orientale Basin								3.72–3.85?	3.72–3.77?
Oldest Mare (Nubium)	315	2.5	ND	ND	ND	ND		ND	
Mare Nectaris	ND	ND	ND	ND	ND	ND		3.74	
M. Tranq., old (A11)	390	ND?	26.2?	200	90±18	23	3.72±0.10	3.80±0.02	
M. Serenitatis (A17)	330–390	1.20		90	100±30	26#		3.75±0.01	
M. Tranq., young (A11)	280–390	1.39	15?	34	64±20	16	3.53±0.05	3.58±0.01	
M. Fecunditatis (L16)	240–300	0.93	15.3		33±10	8.4	3.40±0.05	3.41±0.04	
M. Imbrium (A15)	255–285	0.43	8.01	26	32±11	8.2	3.28±0.10	3.30±0.02	
M. Crisium (L24)		0.43	8.17	26	30±10	7.6	3.30±0.10	3.22±0.02	
O. Procellarum (A12)	210–215	0.72	13.6	24	36±11	9.2	3.18±0.10	3.15±0.04	
Autolycus	160–200	ND	ND	ND	ND	ND		2.1±?	
Copernicus	88–112	0.30	0.06		13±3	3.3	0.85±0.20	0.8±0.015	
Tycho, A17	ND?	0.10	0.019	ND	0.9 ±0.18	0.23	0.109 ±0.004	0.109±0.004	
Tycho	10–20							0.109±0.004	
North Ray Crater	4–5	ND	ND	ND	0.44 ±0.11	0.11	0.05 ±0.0014	0.053±0.008	
Cone Crater	ND	ND	ND	ND	0.21 ±0.05	0.05	0.026 ±0.0008	0.025±0.012	
South Ray Crater								0.002±0.0002	
Terrestrial craters (Phanerozoic)					3.6±1.1	9.2	0.375 ±0.075	0.375±0.075	

(1) = Wilhelms et al. (1987); (2) Hartmann et al. (1981); (3) Neukum and Ivanov (1994); (4) Stöffler and Ryder (2001), Ryder and Spudis (1987), Wilhelms et al. (1987); (5) Stöffler and Ryder (2001), Deutsch and Stöffler (1987), Stadermann et al. (1991); (6) previous proposals, 3.85: Stöffler et al. (1985), 3.87: Jessberger et al. (1977); # from Neukum (1983); ave. = average; ND = not determined; A = Apollo; Fm. = Formation; L = Luna; M. = Mare; O. = Oceanus; Tranq. = Tranquillitatis; a: average mare = 1.88×10^{-4} craters >4 km/km^2. For mare and small, young craters (lower half of table), age assignments by (4,5,6) are the same (rightmost column).

Fra Mauro Formation excavated by Cone Crater at the Apollo 14 site (Stadermann et al. 1991). Other proposed ages (Table 5.10) are 3.92 ± 0.03 Ga (Deutsch and Stöffler 1987; Wilhelms et al. 1987) and 3.95 Ga (James 1981). The data used for deriving these ages do not support older ages for Nectaris such as the 4.1 Ga age proposed by Neukum (1983) as referenced in Neukum and Ivanov (1994). In part, the arguments for ages older than 3.85 Ga reflect the 3.85 Ga age of Imbrium, which is younger than Nectaris. Wilhelms et al. (1987) suggests 3.92 Ga for Nectaris only because this age is most compatible with his assumption of a constant cratering rate in the pre-Nectarian and Nectarian time since about 4.2 Ga (with 30 multiring basins formed between 4.2 and 3.92 Ga and 12 basins formed between 3.92 and 3.85 Ga, his inferred age of Imbrium). However, an assumed constant cratering rate is not a valid age constraint and ages younger than 3.85 for Imbrium have also been proposed (see Section 6.3.1).

6.2.2. Age of the Crisium impact basin. The absolute age of the Crisium basin is tentatively inferred from radiometric ages of a few small particles from the Luna 20 regolith (Wilhelms et al. 1987; Spudis 1993), collected from ejecta deposits of Crisium. Luna 20 landed on the southern rim deposits of the Nectarian Crisium basin (Fig. 5.30), about 35 km north of the mare plains of Fecunditatis (Vinogradov 1973). A core of ~50 g of fine-grained light gray regolith was collected by drilling analogous to Luna 16. Most of the rock fragments are feldspathic granulites, although the bulk soil is somewhat less aluminous than Apollo 16 soil or the highlands meteorites.

Most of the dated fragments are feldspathic, KREEP-poor impact-melt rocks not unlike some of the characteristic melt rocks at the Apollo 16 landing site, although one dated sample (22007,1; 3.87 Ga; Podosek et al. 1973) is similar to the more KREEP-rich, Apollo 17 crystalline melt rocks, which are interpreted as Serenitatis impact melt. One sample of the KREEP-poor impact melt lithology (22023,3,F) was dated at 3.895 ± 0.017 Ga (Swindle et al. 1991) which is proposed as a consistent age for the Crisium basin. Wilhelms et al. (1987) suggested an age of 3.84 ± 0.04 Ga for Crisium (Table 5.10). It remains uncertain whether any of the dated lithic clasts represent Crisium melt or even the youngest clasts of the continuous deposits of Crisium. Its actual age could be younger than 3.89 Ga (see Table 5.10) and nearly as young as the next younger dated basin (Serenitatis).

The relative ages of the Crisium and Serenitatis basins are not definitely clear. The crater density value for superimposed craters > 20 km per 10^6 km² is higher for Serenitatis (83?) than for Crisium (53) although it is based on very poor statistics (Table 5.9; Fig. 5.26), and Serenitatis has been extremely modified by Imbrium. Wilhelms et al. (1987) argues on the basis of superposition and morphology characteristics that Serenitatis is younger than Crisium. This would set an age of 3.87 ± 0.012 Ga, the proposed age for Serenitatis (see below), as the lower limit for the age of Crisium.

6.2.3. Age of the Serenitatis impact basin. The Apollo 15 and 17 landing sites are close to (though just outside of) the main rim of the Serenitatis basin, thus samples from both sites appeared to be suitable for dating the Serenitatis event (Fig. 5.30). Apollo 17 samples were collected from massifs of the Taurus-Littrow region, which are part of the eastern main rim of Serenitatis. The massifs, rising to 2 km above the floor, are dominantly of Serenitatis origin (and therefore Nectarian), and consist of autochthonous and/or allochthonous pre-Serenitatis material. This region is relatively undisturbed and only slightly modified by deposits of younger basins (Wilhelms et al. 1987; Spudis 1993). In contrast, the Imbrium basin-forming event destroyed and buried the western rim formations of Serenitatis.

Most of the sampled boulders, which are most likely derived from the massifs, and large rocks are impact-melt breccias. The most common type of melt breccia is a mafic poikilitic variety. One boulder is composed of an aphanitic, chemically more diverse melt breccia. Fragments of old igneous rocks (dunites, norites etc.) are present as clasts in these melt

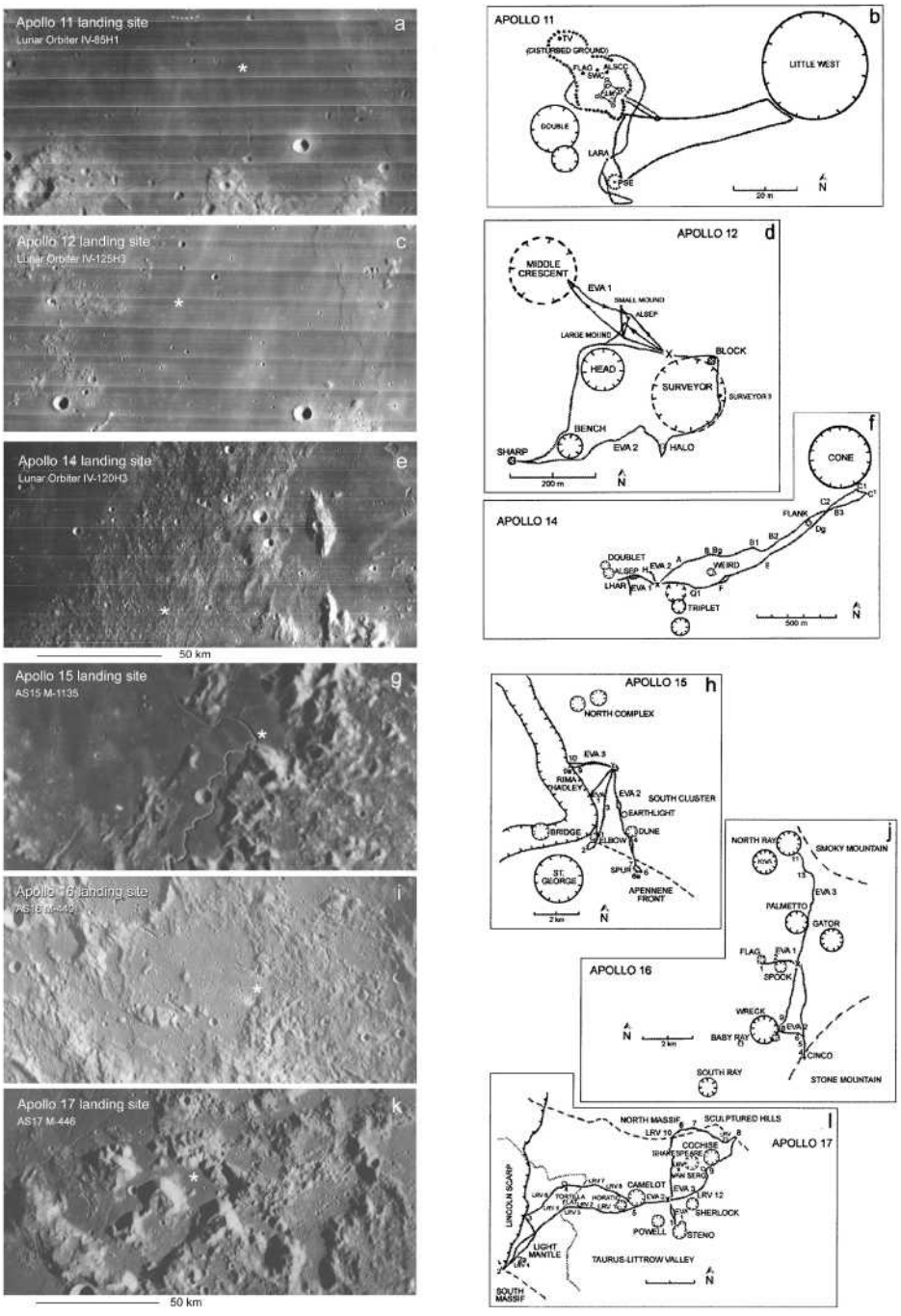

Figure 5.30. (a) Apollo 11 landing area, Mare Tranquillitatis, (b) Map and sampling traverses at the Apollo 11 landing site, (c) Apollo 12 landing area, Oceanus Procellarum, (d) Map and sampling traverses at the Apollo 12 landing site, (e) Apollo 14 landing area, Fra Mauro Formation, (f) Map and sampling traverses at the Apollo 14 landing site, (g) Apollo 15 landing area, Palus Putredinis, Mare Imbrium, and Hadley Delta,

caption and figure continued on facing page

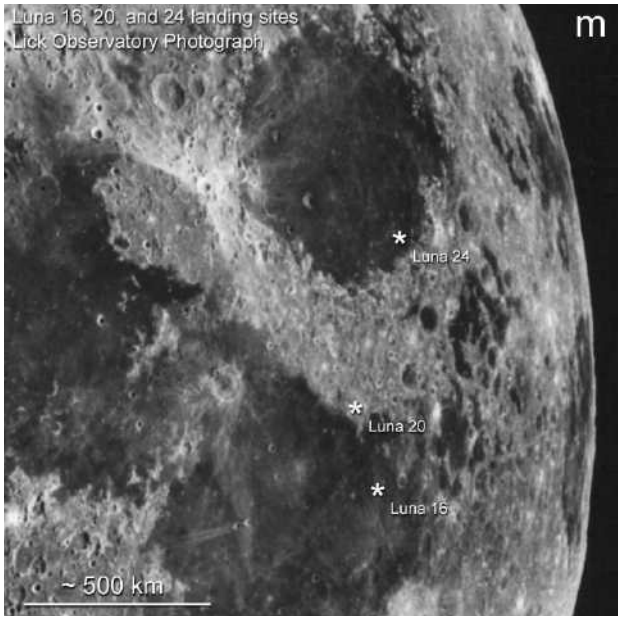

Figure 5.30 (*continued from facing page*). (h) Map and sampling traverses at the Apollo 15 landing site, (i) Apollo 16 landing area, Descartes region, (j) Map and sampling traverses at the Apollo 16 landing site, (k) Apollo 17 landing area, Taurus-Littrow region, Mare Serenitatis, (l) Map and sampling traverses at the Apollo 17 landing site, (m) Landing areas of the Luna 16, 20, and 24 missions, Mare Crisium and Mare Fecunditatis.

breccias. Abundant small fragments of feldspathic granulite suggest that much of the massif material is composed of this lithology (see also Jolliff et al. 1996). The most widespread lithology is represented by poikilitic, fragment-laden impact melt of uniform composition. This is generally inferred to be Serenitatis melt (e.g, Spudis and Ryder 1981). It provides a tightly constrained age of 3.893 ± 0.009 Ga (Dalrymple and Ryder 1996 and references therein; Table 5.10). One boulder and a few smaller fragments from the South Massif are aphanitic fragment-laden impact melts. These have a chemical composition distinct from the poikilitic melts, and they are more varied in both chemistry and fragment population. Inferred ages range between 3.86 and 3.93 Ga, but are on average, younger than those of the poikilitic rocks. These rocks might be a variant of Serenitatis melt, or even from the Imbrium event, although this would be in conflict with the 3.77 ± 0.02 Ga age of Imbrium for which arguments are presented below. Previously proposed ages of 3.86 ± 0.04 or 3.87 ± 0.03 Ga for Serenitatis are based on these younger ages (Jessberger et al. 1977; Wilhelms et al. 1987; Deutsch and Stöffler 1987; Table 5.10). Although the 3.89 Ga age of Serenitatis is well constrained, it remains open whether Serenitatis is indeed 3.89 ± 0.1 or 3.87 Ga because of the uncertainties in assigning unequivocally either one of the two types of impact melt to the Serenitatis event.

6.3. Early Imbrian Epoch

6.3.1. Age of the Imbrium impact basin. Imbrium basin deposits have been sampled at three Apollo landing sites (Apollo 14, 15, and 16) where different facies of Imbrium ejecta were deposited as indicated by photogeological interpretations (Wilhelms et al. 1987; Spudis 1993) and by cratering models (Oberbeck 1975; Schultz and Merrill 1981; Melosh 1989). *Apollo 15* sampled ejecta deposits (most likely including impact melt) at the main rim of the

Imbrium basin, *Apollo 14* sampled polymict breccias and impact-melt rocks of the continuous ejecta blanket (Fra Mauro Formation), and *Apollo 16* sampled a zone of distal discontinuous ejecta (polymict breccias and impact-melt rocks of the Cayley Formation).

Two major proposals for the age of Imbrium have been published in recent years after an age of 3.85–3.90 Ga had been generally accepted before 1980. The ages proposed more recently (Table 5.10) are 3.85 ± 0.02 Ga (Wilhelms et al. 1987; Ryder 1990a, 1994; Spudis 1993; Hartmann et al. 2000) and 3.77 ± 0.02 Ga (Deutsch and Stöffler 1987; Stadermann et al. 1991). The originally accepted age was based mainly on the measured ages of lithologies that were in some way supposedly reset by the Imbrium event and that displayed a peak of their frequency distribution within the 3.85–3.90 Ga age range (e.g., Taylor 1975). This approach is incorrect in light of the foregoing discussion, yet continues to exist. Wilhelms et al. (1987) stated: "The time of the Imbrium impact seems to be well constrained at from 3.82 to 3.87 Ga; the average and well represented age of 3.85 ± 0.03 Ga is tentatively adopted here." This incorrect view persists; for example, Hiesinger et al. (2003) referred to an age of the Imbrium basin as old as 3.91 ± 0.1 Ga. The more recent proposals discussed herein are not based on "histogram" approaches, but on age constraints that apply to relevant geological units.

Arguments for a 3.85 ± 0.02 Ga age. The continuous Imbrium ejecta (Fra Mauro Formation) was directly sampled at the Apollo 14 site. Sampling was from both Cone Crater ejecta and the smooth terrain (Fig. 5.30), both representing the Fra Mauro Formation. At the rim of Cone Crater, feldspathic fragmental breccias were sampled. Melt fragments within these breccias, have a range of ages from about 3.95 to 3.85 Ga (a few older fragments are not impact melts) (Stadermann et al. 1991 and others). Samples collected outside of the Cone Crater ejecta blanket include melt samples with younger ages, down to nearly 3.7 Ga (especially belonging to a single chemical group exemplified by 14310). However, these are not necessarily from the Fra Mauro Formation (a view which is questioned by Deutsch and Stöffler 1987). The Cone Crater samples suggest an age for the Imbrium ejecta blanket of 3.85 ± 0.02 Ga.

Melt samples at the Apennine Front (Apollo 15, Fig. 5.30) must be dominantly pre-Imbrian or contemporaneous with it, as no major impact events later affected the site. Dalrymple and Ryder (1993) obtained chronological data on the range of Apollo 15 impact melts defined by Ryder and Spudis (1987). All but one of the datable samples gave ages around 3.86–3.88 Ga, the other one gave an age of 3.84 ± 0.02 Ga. These data suggest an age for the ejecta blanket of 3.85 ± 0.02 Ga. The Cayley Plains at Apollo 16 are less definitive but nearly all of the impact melts must pre-date Imbrium and nearly all have ages greater than about 3.86 Ga. The main exception is a significant group with a composition similar to local regolith, to be described in the next section. Thus the Apollo 16 data are consistent with that from Apollo 15 as an upper limit on the age of Imbrium.

The Apennine Bench Formation (Hackmann 1966) has the physical features of a volcanic unit. Gamma-ray orbital data (Apollo 15 and Lunar Prospector missions) show that the unit has thorium abundances identical with those of the volcanic KREEP basalts found as small fragments and a common regolith constituent at the Apollo 15 landing site (Hawke and Head 1978; Spudis 1978; Ryder 1987). These volcanic rocks have a well-defined age of 3.85 ± 0.02 Ga, indistinguishable from the upper limit for Imbrium defined by its ejecta. Thus both the upper and lower absolute age limits for Imbrium are the same, establishing the Imbrium basin as 3.85 ± 0.02 Ga (Table 5.10).

Arguments for a 3.77 ± 0.02 Ga age. This age has been derived from detailed Consortium studies of the Apollo 14 and 16 highland breccia samples (e.g., Stöffler et al. 1981, 1985, 1989; Stadermann et al. 1991 and references therein). The main arguments for the 3.77 Ga age are given in Deutsch and Stöffler (1987) and supplemented by Stadermann et al. (1991). The youngest lithic clast of the basement breccias of the Apollo 14 and 16 sites, representing the Imbrium related Fra Mauro and Cayley Formations, respectively, must provide the age of

the parent basin. At both sites, there are "young crystalline impact melt rocks" ranging in age from 3.71 ± 0.03 Ga to 3.81 ± 0.01 Ga (Deutsch and Stöffler 1987). The 3.77 ± 0.02 Ga age is mainly based on the group of anorthositic-noritic melt rocks (3 Apollo 16 melt rocks clustering at 3.75 ± 0.01 Ga) and on the group of youngest Apollo 14 melt rocks, which are chemically distinct from them. The age of 3.77 ± 0.02 Ga is covered by the age uncertainties of the two groups of subophitic melt rocks (Deutsch and Stöffler 1987).

The Apollo 14 and 16 samples younger than 3.82 Ga belong to different textural and chemical groups and range in size from the cm- to the m-scale (e.g., boulder 68415/416). The subophitic samples (e.g., 14310 and 68415/416) represent clast-free, relatively coarse-grained and therefore slowly cooled impact-melt rocks, particularly critical for the arguments against a post-Imbrian origin of these rocks. According to arguments given in Deutsch and Stöffler (1987), these rocks are considered to originate from large pre-Imbrian impact crater formations (melt sheets and polymict breccia deposits); they cannot be derived from erratic clasts ejected from local or distant post-Imbrium craters.

Deutsch and Stöffler (1987) questioned both the argument that the Apennine Bench Formation is younger than Imbrium and that it is composed of the same type of KREEP basalts that occur as clasts at the Apollo 15 landing site dated at 3.85 ± 0.05 Ga (e.g., Carlson and Lugmair 1979). There is no direct geologic evidence that the volcanic "light plains" of the Apennine Bench extend to the Apollo 15 site forming the substratum of the mare basalts and covering Imbrium ejecta (Fig. 7.13 in Spudis 1993) because these assumed relationships are not exposed at the Apollo 15 site. Deutsch and Stöffler (1987) argue therefore, that the Apennine Bench Formation is pre-Imbrian in age and formed on top of an older terra unit that assumed its present position between the inner ring and the main rim of the Imbrium multiring basin as a parautochthonous megablock of the pre-impact target not completely flooded by mare basalt flows.

6.3.2. Age of the Orientale impact basin. Orientale is the youngest of the multiring basins on the Moon (Wilhelms et al. 1987; Spudis 1993), but its absolute age cannot be determined directly from measured ages because samples related to Orientale have not been identified with any certainty at any of the landing sites. This is not surprising because only ray material could be present at the landing sites and would be difficult to identify in the sample collections. Wilhelms et al. (1987) contended that Orientale must have been formed between 3.85 and 3.72 Ga, assuming that 3.85 Ga is the age of Imbrium and 3.72 Ga is a lower limit set by the oldest age of nearby exposed mare basalts of Upper Imbrian age. Based on relative crater densities of these basins, he proposed a tentative age of 3.8 Ga for Orientale. However, it could be almost as old as Imbrium, i.e., 3.84 Ga. Based on the proposed age of 3.77 ± 0.02 Ga for Imbrium (see above) and on the relative crater densities, Orientale should be equal to or younger than 3.75 Ga and could be as young as 3.72 Ga (Table 5.10).

6.4. Late Imbrian Epoch

6.4.1. Age of Apollo 17 basalt surfaces (3.70 - 3.75 Ga). Apollo 17 landed on mare plains of the same intermediate-age group of the Upper Imbrian Series that occupies northern Mare Tranquillitatis near Apollo 11 (Fig. 5.29). The site is located in a mare-flooded valley, a radial graben in the massifs that form a main topographic rim of the Serenitatis basin (Fig. 5.30). The subfloor basalt at the landing site is about 1.4 km thick. Much of the surface of massifs and mare in the area is covered with a "dark mantling material," correlated with volcanic orange glass sampled at the site. The samples collected on the valley floor near numerous fresh clustered craters are dominantly mare basalts and some regolith breccias, and dark mantle material was sampled as orange glass deposits.

The Apollo 17 mare basalt samples collected over a wide area of several kilometers are high-Ti basalt. They fall into distinct chemical groups (Table 5.8) that represent at least four distinct extrusions (Warner et al. 1979; Neal et al. 1990; Ryder 1990b). Most of the samples

are group A (3.75 Ga) or the more complex group B (3.70 Ga). Group C (~3.75 Ga) samples have been identified only among the few Shorty Crater samples, and group D (~3.85 Ga ?) only by one sample from the Van Serg regolith core. Samples from boulders at the rim of the 650 m diameter Camelot Crater (Station 5) presumably represent the deepest excavated basalt, perhaps 100 m; and all belong to group A basalts which occur at all mare sampling locations. Samples of boulders 150 m from the rim of 600 m diameter Steno Crater (Station 1) presumably represent a shallower level and belong to group B basalts. Group B basalts are found throughout the mare sampling locations except Shorty Crater. These relationships suggest that group A basalts underlie group B basalts, consistent with their radiometrically determined ages (Table 5.8). Wolfe et al. (1981) suggested that Group C basalts, dominating the ejecta of the small Shorty Crater, were the youngest, but radiometric ages show that they are older than Group B and similar in age to Group A. Thus the youngest basalts, which flood at least the eastern end of the Taurus-Littrow valley, are the group B basalts (3.70 Ga). However, to the west the covering by group B basalts may be patchy leaving group C and A basalts as the topmost bedrock (3.75 Ga).

Geologic relationships at the Apollo 17 site make relating a radiometric age to a crater density or crater degradation parameter an uncertain task. These include the presence of dark mantle deposits, which appear to be correlated with the sampled orange volcanic glass, with a preferred age of ~3.5 Ga (Tera and Wasserburg 1976); the apparently patchy distribution of the lava flows; and the considerable obscuration of the older cratering history by the production of the central cluster of craters (Lucchitta and Sanchez 1975) at about 110 Ma. However, it seems likely that the mare plain at least to the immediate east of the landing site consists of lava flows with an age of 3.70 Ga, while those extending out into Mare Serenitatis and Mare Tranquillitatis might be slightly older. It is unlikely that the oldest sampled basalts, group D, form any extensive surface in the region. We infer that an age of 3.75 Ga probably best represents the crater densities measured in basalts just inside the southeast rim of Serenitatis (Table 5.10).

6.4.2. Age of Apollo 11 basalt surfaces (3.58 Ga and 3.80 Ga). The landing site, 40 km north-northeast of the nearest highlands region at the Kant Plateau (Fig. 5.30), is on intermediate-age-group basalts of the Upper Imbrian Series, the southern of two belts separated by the youngest-age group (Fig. 5.29). Three patchy units of mare basalt of different age are in the area within at least several tens of kilometers of the landing site (Grolier 1970a,b). For details of the landing site geology, see Heiken et al. (1991) and Stöffler and Ryder (2001).

The mare basalt samples collected from approximately 400 m west of a sharp-rimmed, rayed crater approximately 180 m in diameter and 30 m deep (West Crater) (Fig. 5.30) are all high-Ti varieties. Beaty and Albee (1978) suggested that most of the samples collected were ejected from West Crater. The samples have a range of compositions and ages that represent at least four separately extruded basalt types (Table 5.8). Group A (3.58 Ga), the high-K basalt, is most abundant. Group B1-B3 (3.70 Ga), a complex group, comprises most of the rest of the samples, while the two oldest groups B2 (3.80 Ga) and D (3.85 Ga) are comparatively minor. Exposure data (Geiss et al. 1977) indicate that the group A samples came from a surface exposure, and that the low-K basalts (groups B and D) came from a shielded site, most excavated in a single impact (possibly West Crater, which is only 30 m deep, but possibly from much further away).

Galileo and Clementine spectral reflectance data (Staid et al. 1996) indicate that the landing site lies in, but close to the edge of, a western unit that is both the youngest and the highest in Ti in Tranquillitatis, which they correlate with the group A basalts. A much more extensive nearby unit identified spectrally is older and extends a coherent surface as far north as the Apollo 17 landing site, consistent with this unit being the group B1-3 basalts, which are similar in both age and composition to Apollo 17 basalts. Even older basalts identified spectrally as a little lower in Ti may correspond with group B2 or D (or both). Of the crater density units referred to by Wilhelms et al. (1987) and Neukum and co-workers (e.g., Neukum and Ivanov 1994), we infer

that the young one is the 3.58 Ga group A basalts, and the older one is group B2 or D, which is about 3.80 Ga. For a more detailed discussion see Stöffler and Ryder (2001).

6.4.3. Age of Luna 16 basalt surface (3.41 Ga). Luna 16 landed on mare lavas that flood the 690 km diameter Fecunditatis basin of pre-Nectarian age, about 400 km south of highlands formed by the ejecta blanket of Crisium basin (Fig. 5.30). The mare floods are thin; probably slightly thicker than a kilometer in the center and about 300 m at the landing site (De Hon and Waskom 1976). The basalt plains are in the middle to upper part of the Upper Imbrian System (Fig. 5.29). The sampling site is on a dark unit whose spectral class indicates a higher Ti content than most of Mare Fecunditatis. Presumably this is the unit to which the crater density listed in the Table of Neukum and Ivanov (1994) corresponds.

The samples consist of 101 g of dark gray regolith, obtained by drilling to a depth of 35 cm (Vinogradov 1971). Most of the few particles >3 mm are of feldspathic mare basalt or minerals derived from them; others are glassy agglutinates and regolith breccias. A small amount of feldspathic highland material is present (e.g., Keil et al. 1972). The tiny mare basalt fragments available from the Luna 16 regolith appear to be mainly a coherent chemical group that is more aluminous than typical mare basalts and with intermediate Ti contents (4-5% TiO_2) (Grieve et al. 1972; Keil et al. 1972; Kurat et al. 1976; Ma et al. 1979); they probably represent a single flow or related flows. The basalt fragments are all fine-grained, suggesting either a thin flow or a series of similar, overlapping thin flows. A Rb-Sr isochron and a ^{40}Ar-^{39}Ar age on a single fragment are consistent with an age of 3.41 Ga for this basalt group (Table 5.8; Huneke et al. 1972; Papanastassiou and Wasserburg 1972). Two separate fragments (3.45 ± 0.06 Ga and 3.30 ± 0.15 Ga) are consistent with this age (Cadogan and Turner 1977). The regolith composition (Reid et al. 1972) indicates that the age of this group of basalts is representative of the mare surface at the Luna 16 landing site.

6.4.4. Age of Apollo 15 basalt surface (3.30 Ga). The site is located on a mare plain of the youngest group of the Upper Imbrian Series (Fig. 5.26), about 2 km from Hadley Rille, whose walls expose a layered mare basalt sequence (Fig. 5.30). The maria flood an embayment in the Apennine front, a scarp that is the main rim crest of the Imbrium basin. Extensive lava plains occur to the west of the landing site. Sampling was in the mare plains near the Hadley rille edge and in an area called South Cluster (Fig. 5.30). Samples from the plains are mainly mare basalts and regolith breccias.

The mare basalt samples collected from the mare plains on the Apollo 15 missions are dominated by two low-Ti varieties, the olivine-normative mare basalts (3.30 Ga) and the quartz-normative mare basalts (Ryder and Schuraytz 2001), which are 3.35 Ga old (Table 5.8). The other rare mare basalt fragments are of a similar age, but were found as exotic fragments on the Apennine Front. Various types of volcanic glasses (~3.3–3.6 Ga, Spangler et al. 1984) occur only locally or dispersed in the regolith. Stratigraphically the olivine-normative mare basalts appear to be the highest and are dominant among small rock samples (compilation in Ryder 1985). This is consistent with their younger radiometric ages.

The chemical composition of the Apollo 15 mare regolith samples demonstrates the domination by the olivine-normative mare basalt (Korotev 1987), even at Dune Crater. The difference in ages of all the Apollo 15 mare basalt types (and probably the glass as well) is in any case so small and the total thickness so great that the crater density measured for this part of Palus Putredinis can be ascribed to an age of 3.30 Ga with confidence (Table 5.10).

6.4.5. Age of Luna 24 basalt surface (3.22 Ga). Luna 24 landed on the Upper Imbrian mare plains that flood the Crisium basin (Fig. 5.30), about 40 km north of the basin rim (Butler and Morrison 1977; Florensky et al. 1977). Mare Crisium is fairly uniform but three successive main units have been mapped by Head et al. (1978a). Luna 24 landed on the upper part of the middle age group that is common in the northern part of the basin but also forms exposed

patches in the south. Various lines of evidence suggest that the basalts at the site are about 1–2 km thick. The Luna 24 core (12 mm diameter) was 160 cm long and ~200 cm deep (Barsukov 1977; Florensky et al. 1977). Some larger particles, up to 10 mm in size, are basaltic rocks ranging from very-low-Ti basalt to olivine basalt. Other fragments include glasses, breccias, and agglutinates. Most of the basaltic fragments and at least a large proportion of the coarser mineral fragments from all levels of the Luna 24 regolith core represent a distinct very-low-Ti aluminous mare basalt type (Ryder and Marvin 1978; Taylor et al. 1978; Graham and Hutchison 1980). Metabasalts, impact melts, and glasses have the same composition, indicating that it is a dominant component of the regolith, although other lithic types are present.

The available ages, which appear to all be on low-Ti mare basalts and metabasalts, show a rather narrow range around 3.22 Ga (Burgess and Turner 1998). That the metabasalts have the same ages suggest that they are metamorphosed flow margins and that the basalts consist of a sequence of overlapping flows of similar composition. It is possible that a slightly younger age of 2.93 Ga for one particle should be considered more reliable. Nonetheless it would appear that the basalt particles are dominated by a single component with an age of 3.22 Ga (Table 5.8).

The bulk regolith is very similar in chemical composition for both major and minor elements to that of the very-low-Ti basalts, indicating that these basalts are the surface unit at the landing site. This is inconsistent with the remote-sensing data that show that surfaces with such low Ti do not exist within tens of kilometers of the nominal landing site (Blewett et al. 1997). This implies that Luna 24 did not land where it was reported to have landed, or that the basalts collected are representative of only a very small area surrounded by basalts with higher Ti that were not collected and thus not dated. However, according to Wilhelms et al. (1987), Mare Crisium is stratigraphically among the most uniform, and therefore we consider the 3.22 Ga age to be correlated with the typical crater density of the southern Mare Crisium (Table 5.10).

6.5. Eratosthenian Period

6.5.1. Age of Apollo 12 basalt surface (3.15 Ga). The Apollo 12 site is in a region of mare basalts of a younger age (Eratosthenian) and spectral type different from those at the Apollo 11 site (Fig. 5.30). Highland islands within about 15 km suggest that the basalts are quite thin, and the area is topographically complex. Nearly all of the sampled terrain is dominated by ejecta of several craters larger than 100 m (Fig. 5.30). The site is close to the rim of the 300 m diameter Surveyor Crater. The rock samples are mainly mare basalts, with some regolith breccias.

On the basis of chemical and isotopic characteristics, the collection of more than 40 mare basalt rocks from the Apollo 12 landing site represent three numerically subequal groups (olivine basalts, pigeonite basalts, and ilmenite basalts) and a single fragment of a fourth group (feldspathic basalt) (Neal et al. 1994). The ilmenite and pigeonite basalt groups have very similar ages (3.15–3.17 Ga), with the olivine basalts and the feldspathic basalt being perhaps slightly older (3.22 Ga; Table 5.8). This is consistent with stratigraphic relationships, where the ilmenite basalts are the only type found around the smaller craters, and the pigeonite and olivine basalts required excavation from larger craters (Surveyor, 200 m diameter and Middle Crescent, 400 m diameter). This would indicate that the ilmenite basalt is about 40 m thick (Rhodes et al. 1977). Details of the sample provenance and the relationships with the remotely-sensed data are discussed in Stöffler and Ryder (2001). They note some inconsistency in the use of crater density in plots of this site, even by the same author group. The crater densities are reported to be lower than those of the Apollo 15 site in some papers and higher in others (Neukum et al. 1975a; Neukum and Wise 1976; Neukum 1977; Wilhelms et al. 1987). The crater density data for Apollo 12 (e.g., Neukum et al. 1975a) show an unusual kink at the critical point around 1–2 km sizes, deviating from a standard calibration. Possibly some secondary craters have not been identified and the actual count is indeed lower for Apollo 12 than for Apollo 15. We suggest that the interpolated lower count correlates with the surface basalt age of 3.15 Ga (Table 5.10).

6.6. Copernican Period

6.6.1. Age of Autolycus and Aristillus (2.1 Ga). Early geologic analysis of the Apollo 15 landing site showed that a ray from either of the rayed craters Aristillus or the older but nearer Autolycus crossed the landing site and deposited exotic material. KREEP basalt fragments with an original crystallization age of ~3.84 Ga collected at the landing site were shocked and thermally heated, and in one case shock-melted, at 2.1 Ga (Ryder et al. 1991). Autolycus lies in the Apennine Bench Formation, correlated with Apollo 15 KREEP basalts (Spudis 1978) and is expected to contribute more material to the landing site than Aristillus, which would contribute mainly mare basalt fragments. Thus it is a reasonable inference that Autolycus formed at 2.1 Ga (Table 5.10). If so, and assuming that Autolycus is indeed a Copernican crater, then that Period commenced earlier than commonly assumed from the inference that Copernicus itself is less than 1 Ga (see next section). Unfortunately, and in part because Autolycus has been degraded by the later Aristillus ejecta, crater density measurements have not been made, although D_L measurements (180 ± 20) suggest that it is very close to the Copernican-Eratosthenian boundary (Wilhelms et al. 1987). Autolycus is definitely one of the most degraded Copernican craters.

Although an age of ~1.3 Ga has been suggested for the stratigraphically younger Aristillus crater on the basis of the age of a 1-m block of KREEP impact melt on the Apennine Front (sample 15405; Bernatowicz et al. 1978), this correlation is unreliable (Table 5.10). Aristillus is unlikely to have both created and ejected the melt in question to such a distance, and a delivery from Aristillus floor material by a later impact seems unlikely. It is more likely that sample 15405 is of a more local origin.

6.6.2. Age of Copernicus (0.8 Ga). The Apollo 12 mare landing site is heavily contaminated with KREEP materials, although the nearest non-mare outcrops are about 25 km away. Rays from Copernicus cross the landing site, and Meyer et al. (1971) suggested that KREEP glass in the samples was produced and ejected by the Copernicus event and thus could be used to date it. Subsequent ^{40}Ar-^{39}Ar dating of such materials suggested appreciable degassing at about 800 Ma (Eberhardt et al. 1973; Alexander et al. 1976). U,Th-Pb data also yielded an age of 850 ± 100 Ma for regolith disturbance (Silver 1971). Bogard et al. (1994) found that a granite fragment encased in KREEP glass had been almost completely degassed at 800 ± 15 Ma. These ages are all from samples 12032 and 12033, the most immature and most KREEP rich regoliths, which were probably both collected at Head Crater (Korotev et al. 2000).

The 800 ± 15 Ma age is most commonly accepted as that of Copernicus (Table 5.10). If the dated samples are from Copernicus' rays, then the age of Copernicus is well established. However, this interpretation could be wrong. Not all of the KREEP at the site can be from Copernicus, even in a concentrate in a ray, and most of it may have arrived by other means (Korotev et al. 2000, Jolliff et al. 2000a). The dated samples are all from a restricted site (Head Crater) and the KREEP glass is apparently not found elsewhere, whereas a ray as seen from orbit might be expected to more widely distribute materials. In addition, Copernicus itself does not seem to have excavated dominantly KREEP materials, although KREEP might have been an early jet phase excavating shallow material. With these caveats, then either the age of Copernicus is well-defined at 800 ± 15 Ma (Table 5.10), or it is known only to be younger than about 2 Ga.

6.6.3 Age of Tycho (0.1 Ga). The dating of the crater Tycho (98 km diameter) rests on the inference that a landslide on the slope of the South Massif (Apollo 17) was triggered by ejecta of Tycho, which is about 2200 km away. The exposure age near 0.1 Ga of landslide material then represents the age of Tycho (Wolfe et al. 1975; Arvidson et al 1976; Drozd et al. 1977; Lucchitta 1977). The "Central Cluster" craters at the Apollo 17 site also show an exposure age of about 0.1 Ga, and were interpreted as secondary craters of Tycho (Wolfe et al. 1975; Lucchitta 1977). Thus, Drozd et al. (1977) proposed an age for Tycho of 109 ± 4 Ma (Table 5.10). However, the geological evidence for the South Massif landslide and the Central Cluster craters being formed by distal ejecta from Tycho are somewhat equivocal.

6.6.4. Ages of Cone, North Ray, and South Ray Craters (25, 50, and 2 Ma). These young Copernican craters are of prime interest among all other young craters which have been dated on the basis of cosmic ray exposure ages because (1) samples collected from their ejecta deposits provide the basis for the age determination of the Nectaris and the Imbrium basins (see Sections 6.2 and 6.3) and (2) crater frequency data measured on their ejecta blankets are available (Moore et al. 1980; Table 5.10). According to the exposure age data (Drozd et al. 1974, 1977; Stadermann et al. 1991; Eugster 1999) the ages of Cone Crater (Apollo 14 landing site) and of North Ray and South Ray Craters (Apollo 16 landing site) are 25.1 ± 1.2 Ma, 50.3 ± 0.8 Ma and 2.0 ± 0.2 Ma, respectively (Table 5.10).

6.7. Derivation of a revised, time-calibrated lunar stratigraphy

As discussed in the foregoing section, revised absolute ages can be assigned to the rock-stratigraphic or time-stratigraphic units (Fig. 5.25) as they have been established since the early work of Shoemaker and Hackmann (1962) and later documented in most detail by Wilhelms et al. (1987). The scheme of Wilhelms et al. (1987) and earlier versions of it (Wilhelms 1980, 1984) have been adopted by virtually all textbooks and review articles related to the Moon (e.g., Taylor 1982; Hartmann et al. 1984; Heiken et al. 1991; Spudis 1993). This scheme has to be revised in terms of absolute ages only slightly as shown in Fig. 5.31. Most critical are the absolute ages of the following stratigraphic boundaries: Pre-Nectarian-Nectarian, Nectarian-Imbrian, and Eratosthenian-Copernican. Although we have adopted a 3.92 Ga age for the first, a 3.85 Ga age cannot be ruled with absolute certainty. Two optional ages for the Nectarian-Imbrian boundary have to be kept at this point (3.85 and 3.77 Ga; Stöffler and Ryder 2001). The Eratosthenian-Copernican boundary is most variable in the literature ranging from nearly 2 Ga (Stöffler and Ryder 2001) to 1.5 Ga (Neukum and Ivanov 1994), to 1.2 Ga (Wilhelms et al. 1987), and to less than 1.0 Ga (Stöffler and Ryder 2001). We propose for future consideration to use the age of Copernicus itself as the boundary age: 800 Ma (Fig. 5.31). This would of course imply that the presence of rays at impact craters is no longer a criterion for a Copernican age. Instead, the crater density measured on the ejecta blanket of Copernicus and calibrated by its age (800 Ma) would be the main criterion. As discussed in Section 6, there are a number of problems with rayed craters and their lifetime as exemplified by Autolycus, whose possible age would shift the Copernican Period very far back in time. Using Copernicus as the boundary event would make the definition of the main stratigraphic boundaries on the Moon more consistent since all boundaries would then be defined by major impact events (Fig. 5.31). Moreover, the age sequence 3.92, 3.89, 3.87, 3.85 or 3.77, and 3.75 Ga for Nectaris, Crisium, Serenitatis, Imbrium, and Orientale, respectively, would be most compatible with the differences of the crater densities for these impact basins (Wilhelms et al. 1987).

7. THE LUNAR CRATERING HISTORY

7.1. The lunar cratering rate as a function of time: The data base

The most recent determinations of the absolute ages of datable lunar surface formations have been presented by Stöffler and Ryder (2001) and related to the available measurements of the cumulative frequency of superimposed impact craters. The following section is essentially based on this recent review. The age data, the crater frequencies, and the widely used parameter of crater degradation (D_L) are summarized in Table 5.10. They are used to derive revised calibration curves for the crater retention ages of lunar surfaces of varied age ranging from about 4 Ga to the present (Figs. 5.32 and 5.33). The same data have also been used for the revised calibration curve of Neukum et al. (2001). As recognized very early in the Apollo lunar science program (e.g., Hartmann 1970; Soderblom and Lebofsky 1972), such calibration curves are of fundamental importance for (1) determining the cratering rate in the Earth-Moon system as a function of time, (2) establishing an absolute lunar stratigraphy, and (3) providing

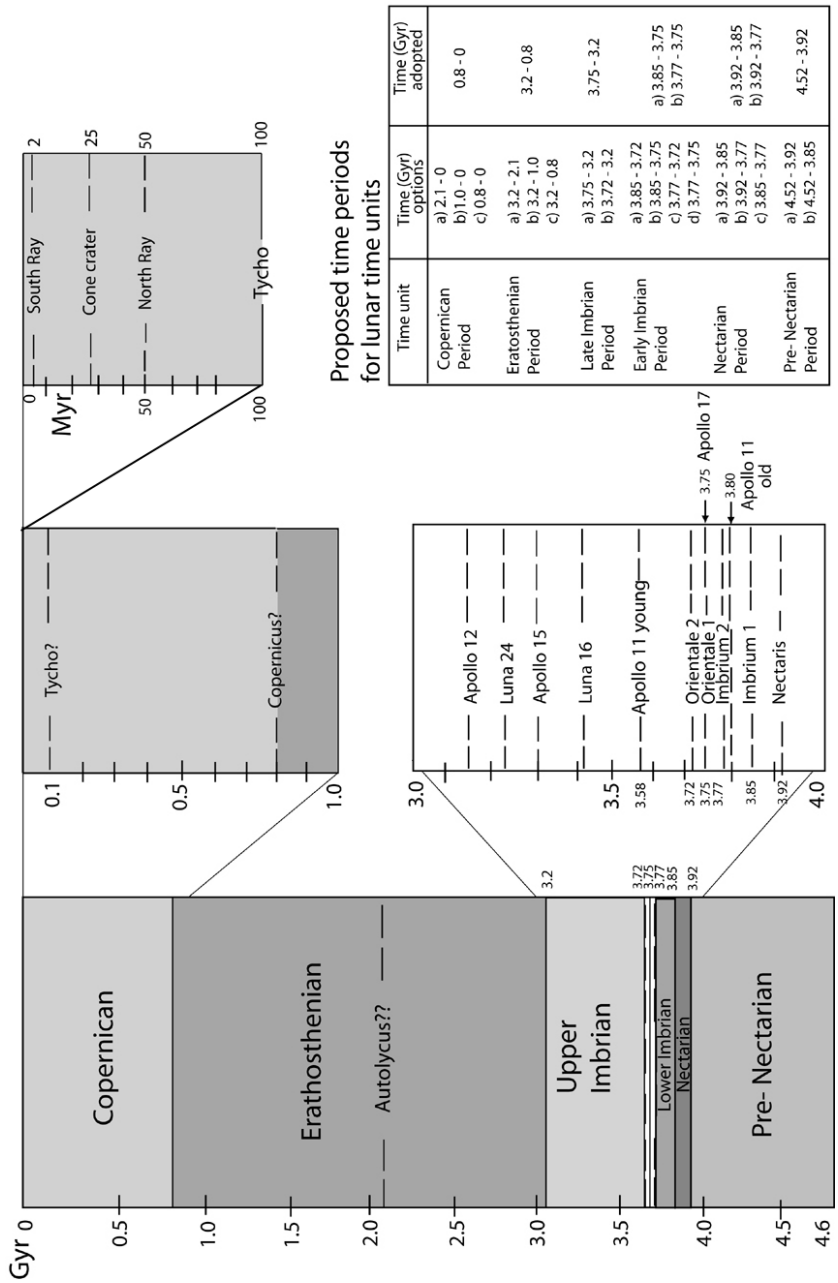

Figure 5.31. Proposal for a revised time-calibrated lunar stratigraphy based on data from Stöffler and Ryder (2001) and from references therein. The proposal differs from these authors regarding the age of the Eratosthenian-Copernican boundary. The data points for the lunar landing sites refer to ages of mare basalt surfaces. The optional age of 3.85 Ga for Nectaris basin is not shown here because the 3.92 Ga age is preferred.

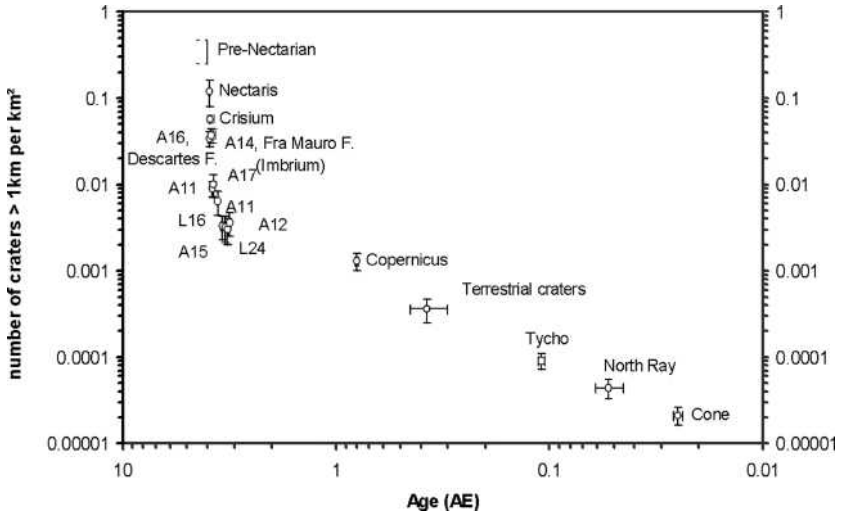

Figure 5.32. Cumulative crater frequencies for craters > 1 km per km² as a function of the age of dated lunar surfaces; data are from Table 5.10 in a log-log-plot; for some impact basins alternative ages are given according to sets a) and b) of Table 5.10 (from Stöffler and Ryder 2001).

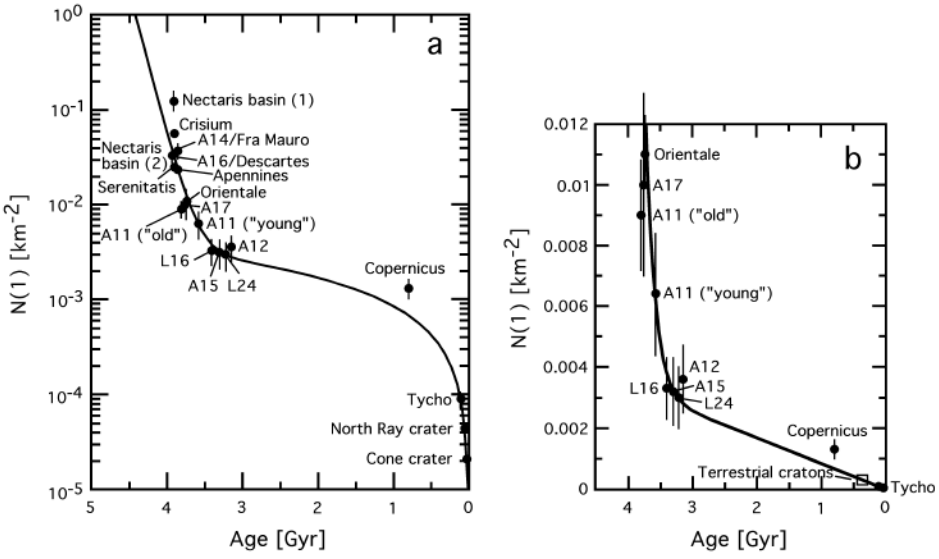

Figure 5.33. Graphical representation of Equation (5.13) (lunar cratering chronology) with data points from Table 5.10 (see also Table VI of Stöffler and Ryder 2001); *N*-values for Serenitatis and Apennines are from G. Neukum (pers. comm. of unpub. data) and are not contained in Table 5.10; a) logarithmic scale for *N*, b) part of the lunar *N*/*T* function with linear scale for *N*. Data for terrestrial craters are shown assuming a constant cratering rate (see Fig. 5.23) with error bars of factor of $2^{1/2}$.

a standard reference curve for stratigraphic time applicable for other planetary bodies of the inner solar system (cf. Section 3).

Calibration curves for the lunar cratering rate and the absolute crater retention ages have been presented previously by a number of authors (Hartmann 1972; Soderblom and Lebofsky 1972; Neukum et al. 1975b, Neukum and König 1976; Hartmann et al. 1981; Neukum and Ivanov 1994) which used another set of ages derived for specific surface areas from isotope ages of lunar samples. These curves were reproduced in a large number of reference books and textbooks such as Taylor (1982), Wilhelms et al. (1987), and Heiken et al. (1991), and have been widely and sometimes, as will be shown below, uncritically accepted by the planetary science community.

During the evaluation of the presently available database (Sections 4–6), it became evident that several problems exist with previously used age calibration curves of the lunar crater frequency data (relative crater retention ages) from which absolute crater retention ages have been derived for lunar surface units of unknown age. The problems relate to the following:

1. The definition of coeval surface units for a specific set of crater counts
2. Incorrect derivation of mare surface ages from ranges of mare basalt ages
3. The use of outdated or even incorrect absolute ages (including incorrect uncertainties) of surface units based on wrong interpretations of ages of lunar rocks
4. Incorrect ages of multiring basins including incorrect uncertainties
5. The unsubstantiated assignment of an absolute age of >4.3 Ga to terrains of oldest lunar crust ("ancient highland," "lunar uplands") displaying the highest values for measured crater frequencies

For some of these issues or open questions we present solutions or suggestions; some others remain open or at least disputable.

We propose new best estimates for *ages of mare surfaces* at the Apollo and Luna landing sites and new errors for these ages, which are lower than the errors used in previous calibration curves by the Basaltic Volcanism Study Project (Hartmann et al. 1981) and by Neukum and Ivanov (1994): 3.75 ± 0.01 Ga (Apollo 17), 3.80 ± 0.02 Ga (Apollo 11 older surface unit), 3.58 ± 0.01 Ga (Apollo 11 younger surface unit), 3.41 ± 0.04 Ga (Luna 16), 3.30 ± 0.02 Ga (Apollo 15), 3.22 ± 0.02 Ga (Luna 24), and 3.15 ± 0.04 Ga (Apollo 12). These data and the corresponding values used previously are given in Tables 5.8 and 5.10 and used for the Figures 5.32 and 5.33.

For the *ages of multiring basins* of the Nectarian and Imbrian Systems we are proposing two differing sets of data for which arguments are discussed in Section 6. They may be used in parallel for the calibration curve until better data become available (Table 5.10, Figs. 5.32 and 5.33). The differences in ages for Imbrium (3.85 Ga vs. 3.77 Ga) and the various ages proposed for Nectaris ranging from 3.92 Ga to 3.85 Ga as well as the somewhat differing ages for Crisium and Serenitatis do not have much influence on the shape of the calibration curves (Figs. 5.32 and 5.33). However, there is an effect on the curves due to the deletion of old, outdated ages and of unjustified errors (Hartmann et al. 1981; Neukum and Ivanov 1994) for the Nectaris basins (4.1 ± 0.1 Ga), the Descartes Formation (3.90 ± 0.1 Ga), the Imbrium basin, and the Fra Mauro Formation (3.91 ± 0.1 Ga). An additional important effect comes from discarding very old ages for the pre-Nectarian highlands such as the specific age of 4.35 ± 0.1 Ga for the "ancient highlands" (Neukum and Ivanov 1994) and the age ranges of 4.0–4.4 Ga and 4.35–4.55 Ga for the "most densely cratered province" and the "uplands" (Hartmann et al. 1981). For these old ages no firm geologic evidence combined with any clear isotope data basis exists.

For the *ages of Eratosthenian and Copernican craters* and the related ejecta blankets appreciable uncertainties still exist. Although some of the youngest ages are indisputable and

perfectly constrained (Cone, North Ray and South Ray Craters), others are isotopically well constrained ages (radiometric and exposure ages) but their geological interpretation is uncertain or equivocal (2.1, 0.8, and 0.1 Ga for Autolycus, Copernicus, and Tycho, respectively), and the remaining age (1.3 Ga for Aristillus), little more than speculative.

The improved data base has been incorporated into the absolute age calibration for the lunar cratering rate as shown in Figures 5.32 and 5.33 by Stöffler and Ryder (2001) and by Neukum et al. (2001). These new calibration curves, which are also adopted here, affect all calibration curves for other terrestrial planets (see original curves in Hartmann et al. 1981, Figs. 8.6.1 to 8.6.5 as reprinted in Taylor 1982, p. 105, and in Neukum and Ivanov 1994, Fig. 16). The calibration curve published in the Lunar Sourcebook (Heiken et al. 1991, Fig. 4.15) contains large errors (e.g., the data points for L24, A14, and A16 are incorrect) and is therefore misleading by suggesting large uncertainties for the determination of absolute crater retention ages of lunar surfaces. For example, for a surface with 10^{-4} craters >4 km/km^2, the minimum and maximum values for its age differ by some 1.7 Ga (!) compared to about 0.9 Ga read from the revised calibration. For an area with 5×10^{-4} craters >4 km/km^2 the corresponding value drops from about 0.55 Ga to some 0.15 Ga. This problem holds similarly with the lunar standard curve of Hartmann et al. (1981, Fig. 8.6.1) but somewhat less with Neukum and Ivanov's (1994) curve because it contains the correct value for Luna 24 and smaller error bars for Apollo 16 and 14 than that in Heiken et al. (1991).

7.2. Interpretations of the lunar cratering rate and the ongoing debate about a possible late cataclysm

What are the major implications of the new calibration curve (Figs. 5.32 and 5.33, Table 5.10), which is based on Stöffler and Ryder (2001) and Neukum et al. (2001), for the lunar cratering rate as a function of time?

First, it is important to note that the data base is compatible with the analytical formula for the crater production rate originally proposed by Neukum (1983) and discussed in detail in Neukum and Ivanov (1994) and Neukum et al. (2001):

$$N(1) = 5.44\times10^{-14}\left[\exp(6.93\,T)-1\right] + 8.38\times10^{-4}\,T \qquad (5.13)$$

which relates the number of craters equal to and larger than 1 km in diameter per km² in an area with the crater accumulation time (crater retention age) T in Ga. Assuming a constant shape in time for the "Size-Frequency Distribution" (SFD) for the projectiles (see Section 3), Equation (5.13) is valid for any crater diameter because we assume a constant slope of the crater size-frequency distribution.

The data base presented above also demonstrates with a first order accuracy that (a) during the last 3 Ga the lunar impactor flux was relatively constant with possible variations by a factor of 2, which is in accordance with age data for young impact-melt rocks to be discussed below, and (b) before 3 Ga ago, the impactor flux ("early heavy bombardment flux") was much higher and rapidly decaying in time. Figure 5.33, for example, shows the graphical representation of Equation (5.13) and demonstrates that on approximately 4 Ga old surfaces 95% of all craters were formed between 3 and 4 Ga ago and only 5% of craters are younger than 3 Ga. The time-derivative of the number frequency - time relationship ($N - T$ function) gives an expression for the cratering rate, dN/dt. The results are shown in Fig. 5.34. One can see that the cratering rate 4 Ga ago was 500 times higher than the constant rate during the last 3 Ga in accord with earlier models by Hartmann (1970), Hartmann et al. (1984), and Neukum (1983).

The recommended calibration curve (Figs. 5.32 and 5.33) is better constrained, with small errors in the age range from about 4.0 to 3.0 Ga, corresponding to cumulative crater frequencies of about 1.5×10^{-1} craters >1 km/km² to about 2×10^{-3} craters >1 km/km². However, major uncertainties still exist for the pre-Nectarian Period (> ca. 4 Ga) and for the Eratosthenian and

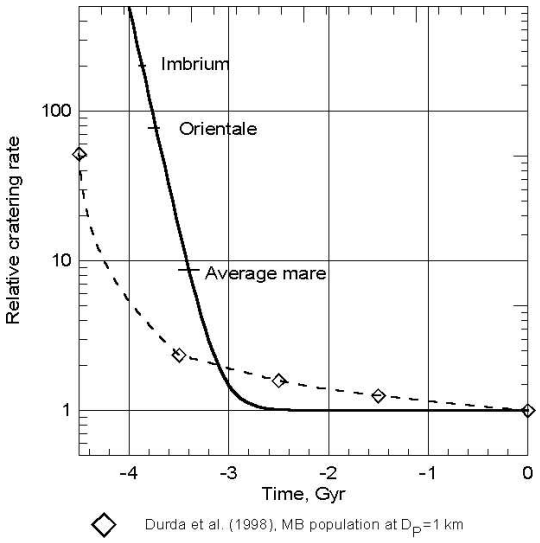

Figure 5.34. Estimate of the cratering rate as a function of time. The curve is a time derivative of Equation (5.13), normalized to the modern impact rate. Diamonds present the model by Durda et al. (1998) where the gradual decrease of the number of the Main Belt asteroids is due to the collision evolution only (no losses to planet crossing orbits).

Copernican Periods (< about 3 Ga). The steepness of the calibration curve above about 3.75 Ga, the possibility that the pre-Nectarian surfaces for which crater counts exist (see Table 5.10 and Fig. 5.26) may not be older than 4.2 Ga (Wilhelms et al. 1987), and the fact that impact melt lithologies older than 4.15 Ga are lacking indicate that the cratering rate may not increase smoothly according to the present calibration curve from 3.75 Ga up to the time of the formation of the Moon. Ryder (1990a) argued that a smooth increase would be incompatible with the accretion rates required for the size of the Moon, contrasting with opposite views (Hartmann et al. 2000). The observations at least mean that the cratering rate between 4.5 and 4.0 Ga is not known and that there is still room for speculation about a possible late lunar cataclysm (Tera et al. 1974; Ryder 1990a; Hartmann et al. 2000).

Recent age data obtained for impact-melt rock clasts of lunar meteorites (Cohen et al. 2000; Cohen 2002) have been interpreted by these authors in favor of the cataclysm hypothesis (see also Kring and Cohen 2002), referring to a peak in the age distribution around 3.9 Ga and to a lack of ages older than ~4.0 Ga. This view has been questioned by Hartmann (2003) since the ages of impact-melt rocks measured by Cohen et al. (2000) and Cohen (2000) in fact show a wide range from ~4.2 to ~0.5 Ga, in agreement with the corresponding age data from the Apollo 16 landing site (Stöffler et al. 1985; Deutsch and Stöffler 1987; see also Sections 5.2 and 6.2). Moreover, Hartmann claims that the lack of ages of lunar impact-melt rocks older than ~4.1 Ga is a consequence of the early heavy bombardment which lead to a "pulverization" of melt rocks prior to ~4.1 Ga (his model implies survival half-lives of melt rocks of <100 Ma prior to 4.1 Ga ago: "lack of old impact melts does not mean lack of old impacts"). Hartmann (2003) argued strongly against a late cataclysm ("The hypothesis of a lunar cataclysmic cratering episode between 3.8 and 3.9 Ga ago lacks proof"). He argued also against the view of Kring and Cohen (2002) that a late cataclysm affected the whole inner solar system by showing that the age data (Apollo lunar rocks, lunar meteorites, asteroidal meteorites) cannot be interpreted in this way. We believe that the review of all available data discussed in this chapter provides no solid arguments for assuming a low cratering rate early in the Moon's history and one distinct, late cataclysm (around 3.8–3.9 Ga ago), but it leaves the possibility for the existence of discrete spikes in the pre-Imbrian cratering rate, which in general appears to decline smoothly from a maximum rate existing very early in the Moon's history (see also Hartmann 2003). In fact, the impactor flux required to accrete the Earth in ~50 Ma and declining with half-lives ranging from

a few Ma early in time to about 20–30 Ma later in time can be fit to the mathematical model function of Neukum et al. (2001) discussed above (Hartmann et al. 2000; Hartmann 2003).

The cratering rates for the Eratosthenian and Copernican Periods are also not sufficiently well constrained because reliable absolute ages for surfaces formed between 3 Ga and 1 Ga are conspicuously lacking. In spite of the uncertain ages of the craters Autolycus, Aristillus, and Copernicus, the tentative figures for their ages are largely compatible with a steady state and constant cratering flux since about 3 Ga, although the data for Copernicus (Figs. 5.32 and 5.33) may indicate a slightly increased flux in the past 1 Ga. The possibility of a non-constant flux has been confirmed recently by the non-uniform distribution of ^{40}Ar-^{39}Ar ages of 155 glass spherules collected from the Apollo 14 regolith (Culler et al. 2000). Culler et al. suggested that the cratering rate decreased since about 3.5 Ga by a factor of 2 to 3 to a minimum value at about 0.5–0.6 Ga and increased by a factor of 3.7 ± 1.2 in the past 0.4 Ga in accordance with data for terrestrial craters (Grieve and Shoemaker 1994) and astronomical constraints (Shoemaker et al. 1994). We argued in Section 3 that a reevaluation of the terrestrial cratering record and of the astronomical data sets does not support a recent increase of the impact flux as suggested by Culler al. (2000). The question of whether such changes in the post-Imbrian cratering flux of the Earth-Moon system are real or not (see Ryder 2000; Hörz 2000; Muller et al. 2000) has important implications for the chronostratigraphy of Mars and other terrestrial planets.

7.3. Open questions and future work

The most burning open questions concerning the time-calibrated impact rate and the absolute time scale for the lunar stratigraphy relate to the following issues:

(a) The lack of datable lunar samples from which age data could be derived for lunar highland terrains that are older than 4.0 Ga such as intensely cratered highland regions of the far side of the Moon or surface material deposited by the South Pole-Aitken impact basin.

(b) The lack of datable lunar samples from Eratosthenian and possibly Copernican mare basalt surfaces (extending to at least 1.2 Ga ago as proposed by Hiesinger et al. 2003) and from large Eratosthenian and Copernican rayed craters such as Autolycus, Copernicus, and Tycho.

(c) Continued uncertainties in the unequivocal dating of lunar multiring basins, in particular, of the Nectaris and Imbrium basins and the lack of age data for the Orientale impact basin.

(d) The existence (or not) of a late cataclysm or of spikes in the impact flux prior to 3.75 Ga as a consequence of issues (a) and (c); this problem is related to the lack of impact-melt rock samples older than about 4.2 Ga.

(e) The source and nature of projectiles impacting the Moon during the Early Heavy Bombardment and/or during discrete spikes of the impact flux, e.g., a late cataclysm.

The problem with the lack of fundamental ground truth data concerning the lunar cratering rates in the "old" pre-Nectarian and in the "younger" Eratosthenian and Copernican time periods—outlined in the issues (a) and (b)—can only be solved by new sample return missions to pre-Nectarian, Eratosthenian, and Copernican regions of the Moon. In terms of the fundamental task to improve the lunar standard reference for the cratering flux in the inner solar system, such missions should be given an equally high priority as sample return missions to Mars.

Part of the problem related to issues (c) and (d) is model dependent and part of it is due to insufficient evaluation and sometimes incorrect interpretation of lunar highland samples and of their absolute ages. This holds particularly for polymict breccias and for their geological setting and provenance. The first part of the problem concerns the lack of understanding of impact cratering mechanics of large basins, especially of the effects of ballistic sedimentation

(Oberbeck 1975) on the stratigraphy and nature of samples at the highland landing sites such as Apollo 14, 15, 16, and 17. Haskin and coworkers have reinvestigated this problem (Haskin et al. 2002, 2003) and proposed "average stratigraphies" for the relevant landing sites. However, these models do not account for important details such as the influence of pre-existing relief on the thickness distribution of the secondary mass flow, which could be much thinner at specific places than predicted by the model (see the ground truth at the Ries crater ejecta blanket, Hörz et al. 1983; Pohl et al. 1977). Such model stratigraphies are of limited use for specific local interpretations; for example, it cannot be proven that post-Imbrian craters such as North Ray Crater (Apollo 16) did not penetrate into Nectaris deposits as predicted by the model because the real, local thicknesses of the Imbrium deposits are not known. The distinct differences in the distributions of ages of clasts found in breccias at North Ray Crater rim as opposed to those in the Cayley plains (Apollo 16), and in breccias at Cone Crater rim as opposed to those of the main landing site of Apollo 14 speak to the contrary of the model assumptions (e.g., Stöffler et al. 1985; Deutsch and Stöffler 1987; Stadermann et al. 1991).

The second major problem of issue (d) is the lack of old impact melt lithologies, which has been used in favor of a late cataclysm (e.g., Ryder 1990a; Kring and Cohen 2002). The absence of old impact melts has been explained by Hartmann (2003) as an effect of the very heavy early bombardment in erasing the record of impact-melt rocks older than 4.1 Ga. We believe that multiple impact cratering cannot completely erase previously formed, old impact melt clasts because (1) resetting of ages by remelting of old melt lithologies is extremely inefficient and (2) impact brecciation typically does not lead to very fine grained material which could no longer be dated (in fact all returned highland breccias are not at all fine-grained, e.g., Heiken et al. 1991). In our view it appears more likely that the specific geological setting of the Apollo highland landing sites (14, 15, 16, and 17) lead to a very selective sampling of material dominated by Nectaris, Serenitatis, and Imbrium ejecta deposits, all being younger than 3.92 Ga, and by material from smaller craters, locally reworked by the ejecta of these three basins from craters formed shortly before those large impact events, e.g., later than 4.2 Ga ago. One important additional aspect related to the problem, which has been largely neglected so far, is that coherent melt sheets of very large craters could be differentiated similar to the terrestrial Sudbury Igneous Complex (Pye et al. 1984; Grieve et al. 1991) and be developed as clast-free impact melt lithologies with "igneous" textures that would not necessarily be recognized as impact-melt rocks. Members of the very old "Mg-suite" of plutonic rocks having ages between 4.5 and 4.2 Ga (see Table 5.6) could be old impact-melt rocks. In conclusion, data from the study of the Apollo and Luna samples cannot solve the issues of the early bombardment history of the Moon. The study of lunar meteorites is somewhat more promising but the final answers can only come from new sample-return missions.

The extremely high impact rate during the early heavy bombardment (EHB) leads to the question—outlined in issue (e)—about the nature of projectiles responsible for this effect: asteroids, comets, or left-over planetesimals? A detailed discussion of this issue is beyond the scope of this article and the reader is referred to a recent review by Hartmann et al. (2000). Clearly, the source and nature of projectiles during the EHB period and the decay of the EHB flux in time are important topics for future studies. An equally enigmatic issue relates to the source and nature of projectiles that are potentially responsible for spikes in the flux during the EHB or for a late or terminal cataclysm, if it can be proven.

8. ACKNOWLEDGMENTS

The first author is greatly indebted to the technical staff and students of the Institute of Mineralogy, Museum für Naturkunde, Berlin, for excellent assistance. In particular, thanks are due to Hwa Ja Nier, Kirsten Born, Ingo Herter, Daniel Lieger, Karin Reineck, and Heidi Wolff. The third author's (B.A.I.) participation is supported by the Humboldt Foundation, Germany.

Critical reviews by Elisabetta Pierazzo and Peter Schultz helped to improve the manuscript and are appreciated.

9. REFERENCES

Ahrens TJ, O'Keefe JD (1972) Shock melting and vaporization of lunar rocks and minerals. The Moon 4:59-94

Ahrens TJ, O'Keefe JD (1977) Equations of state and shock-wave attenuation on the Moon. *In*: Impact and Explosion Cratering. Roddy DJ, Pepin RO, Merrill RB (eds), Pergamon, p 639-656

Ahrens TJ, Takata T, O'Keefe JD, Orton GS (1994) Impact of comet Shoemaker-Levy 9 on Jupiter. Geophys Res Letters 21:1087-1090

Alexander EC Jr, Bates A, Coscio MR Jr, Dragon JC, Murthy VR, Pepin RO, Venkatesan TR (1976) K/Ar dating of lunar soils II. Proc Lunar Sci Conf 7:625-648

Anderson CE (1987) An overview of the theory of hydrocodes. Int J Impact Engng 3:33-59

Anderson JLB, Schultz PH, Heineck JT (2003) Asymmetry of ejecta flow during oblique impacts using three-dimensional particle image velocimetry. J Geophys Res 108(E8):13.1-10, doi:10.1029/2003JE002075

Artemieva NA (2001) Tektites and Martian Meteorites in Numerical Modeling of Impacts. Meteorit Planet Sci 36:A12

Artemieva NA, Shuvalov VV (2001) Motion of a fragmented meteoroid through the planetary atmosphere. J Geophys Res 106:3297-3310

Artemieva NA, Ivanov BA (2001) Numerical simulation of oblique impacts: impact melt and transient cavity size. Lunar Planet Sci XXXII:1321

Artemieva NA, Ivanov BA (2002) Ejection of Martian meteorites - can they fly? Lunar Planet Sci XXXIII:1113

Artemieva NA, Ivanov BA (2004) Launch of martian meteorites in oblique impacts. Icarus 171:84-101

Arvidson R, Drozd RJ, Guinness E, Hohenberg CM, Morgan CJ, Morrison RH, Oberbeck VR (1976) Cosmic ray exposure ages of Apollo 17 samples and the age of Tycho. Proc Lunar Sci Conf 7:2817-2832

Baldwin RB (1949) The Face of the Moon. University of Chicago Press

Baldwin RB (1981) On the tsunami theory of the origin of multi-ring basins. *In*: Multi-Ring Basins. Schultz PH, Merrill RB (eds), Pergamon, p 275-288

Barsukov VL (1977) Preliminary data for the regolith core brought to earth by automatic lunar station Luna 24. Proc Lunar Sci Conf 8:3303-3318

Bauer JF (1979) Experimental shock metamorphism of mono- and polycrystalline olivine. A comparative study. Proc Lunar Planet Sci Conf 10:2573-2596

Beaty DW, Albee AL (1978) Comparative petrology and possible genetic relations among the Apollo 11 basalts. Proc Lunar Planet Sci Conf 9:359-463

Benz W, Asphaug E (1999) Catastrophic disruptions revisited. Icarus 142:5-20

Bernatowicz TJ, Hohenberg CM, Hudson B, Kennedy BM, Podosek FA (1978) Argon ages for lunar breccias 14064 and 15405. Proc Lunar Planet Sci Conf 9:905-919

Binder A (1998) Lunar Prospector: overview. Science 281:1475-1476

Bischoff A, Stöffler D (1984) Chemical and structural changes induced by thermal annealing of shocked feldspar inclusion in impact melt rocks from Lappajärvi Crater, Finnland. Proc Lunar Planet Sci Conf 14:B645-B656

Bischoff A, Stöffler D (1992) Shock metamorphism as a fundamental process in the evolution of planetary bodies: information from meteorites. Eur J Mineral 4:707-755

Bjork RL (1961) Analysis of the formation of Meteor Crater, Arizona: a preliminary report. J Geophys Res 66:3379-3387

Bjorkman MD, Holsapple KE (1987) Velocity scaling impact melt volume. Int J Impact Eng 5:155–163

Blewett DT, Lucey PG, Hawke BR, Jolliff BL (1997) Clementine images of the lunar sample-return stations: Refinement of FeO and TiO2 mapping techniques. J Geophys Res 102:16,319-16,325

Bogard D, Hörz F, Johnson P (1987) Shock effects and argon loss in samples of the Leedey L6 chondrites experimentally shocked to 29-70 GPa pressures. Geochim Cosmochim Acta 51:2035-2044

Bogard D, Hörz F, Stöffler D (1988) Loss of radiogenic argon from shocked granitic clasts in suevite deposits from the Ries Crater. Geochim Cosmochim Acta 52:2639-2649

Bogard D, Garrison DH, Shih CY, Nyquist LE (1994) ^{40}Ar-^{39}Ar dating of two lunar granites: The age of Copernicus. Geochim Cosmochim Acta 58:3093-3100

Bottomley RJ, York D, Grieve RAF (1990) ^{40}Argon-^{39}Argon dating of impact craters. Proc Lunar Planet Sci Conf 20: 421-431

Boyce JM, Dial AL Jr. (1975) Relative ages of flow units in Mare Imbrium and Sinus Iridum. Proc Lunar Sci Conf 6: 2585-2595

Braslau D (1970) Partitioning of energy in hypervelocity impact against loose sand targets. J Geophys Res 75:3987-3999

Bridgman PW (1922) Dimensional Analysis. Yale University Press

Buckingham E (1914) On physically similar systems: Illustrations of the use of dimensional equations. Phys Rev 4: 345-376

Burchell MJ, MacKay NG (1998) Crater ellipticity in hypervelocity impacts on metals. J Geophys Res 103:22,761-22,774
Burgess R, Turner G (1998) Laser ^{40}Ar-^{39}Ar age determinations of Luna 24 mare basalts. Meteorit Planet Sci 33:921-935
Butler P, Morrison DA (1977) Geology of the Luna 24 landing site. Proc Lunar Sci Conf 8:3281-3301
Cadogan PH, Turner G (1977) ^{40}Ar-^{39}Ar dating of Luna 16 and Luna 20 samples. Phil Trans Royal Soc London 284: 167-177
Cameron AGW (2001) From interstellar dust to the Earth-Moon system. Meteorit Planet Sci 36:9-22
Cameron AGW, Benz W (1991) The origin of the Moon and the single impact hypothesis. Icarus 92:204-216
Campo Bagatin A, Cellino A, Davis DR, Farinella P, Paolicchi P (1994a) Wavy size distribution for collisional systems with a small-size cutoff. Planet Space Sci 42:1049-1092
Campo Bagatin A, Farinella P, Petit J-M (1994b) Fragment ejection velocities and the collisional evolution of asteroids. Planet Space Sci 42:1099-1107
Canup RM, Asphaug E (2001) Outcomes of planet-scale collisions. Lunar Planet Sci XXXII:1952
Carlson RW, Lugmair GW (1979) Sm-Nd constraints on early lunar differentiation and the evolution of KREEP. Earth Planet Sci Lett 45:123-132
Chabai AJ (1965) On scaling dimensions of craters produced by buried explosives. J Geophys Res 70:5075-5098
Chapman CR, McKinnon WB (1986) Cratering of planetary satellites. *In*: Satellites. Burns JA, Matthews MS (eds), Univ Arizona Press, p 529-533
Cintala MJ (1979) Mercurian crater rim heights and some interplanetary comparisons. Proc Lunar Planet Sci Conf 10: 2635-2650
Cintala MJ (1992) Impact-induced thermal effects in the lunar and mercurian regoliths. J Geophys Res 97:947-974
Cintala MJ, Grieve RAF (1994) The effects of differential scaling of impact melt and crater dimensions on lunar and terrestrial craters: Some brief examples. *In*: Large Meteorite Impacts and Planetary Evolution. GSA Spec Paper 293:51-59
Cintala MJ, Grieve RAF (1998) Scaling impact-melt and crater dimensions: Implications for the lunar cratering record. Meteorit Planet Sci 33:889-912
Cintala MJ, Hörz F (1990) Regolith evolution in the laboratory: Scaling dissimilar comminution experiments. Meteoritics 25:27-40
Cintala MJ, Wood CA, Head JW (1977) The effects of target characteristics on fresh crater morphology: Preliminary results for the Moon and Mercury. Proc Lunar Sci Conf 8:3409-3425
Cintala MJ, Head JW, Veverka J (1979) Characteristics of the cratering process on small satellites and asteroids. Proc Lunar Planet Sci Conf 9:3803-3830
Cintala MJ, Shelfer TD, Hörz F (1999) Growth times of impact craters formed in fine-grained sand. Lunar Planet Sci XXX:1958
Cohen BA (2002) Geochemical and geochronological constraints on early lunar bombardment history. Lunar Planet Sci XXXII:1984
Cohen BA, Swindle TD, Kring DA (2000) Support for the lunar cataclysm hypothesis from lunar meteorite impact melt ages. Science 290:1754-1756
Collins GS, Melosh HJ, Morgan JV, Warner MW (2002) Hydrocode simulations of Chicxulub crater collapse and peak-ring formation. Icarus 157:24-33
Collins GS, Melosh HJ (2004) Numerical modeling of the South Pole-Aitkin impact. Lunar Planet Sci XXXV:1375
Crawford DA (1997) Comet Shoemaker-Levy 9 fragment size and mass estimates from light flux observations. Lunar Planet Sci XXVIII:267
Crawford DA, Boslough MB, Trucano TJ, Robinson AC (1994) The impact of comet Shoemaker-Levy 9 on Jupiter. Shock Waves 4:47-50
Croft SK (1978) Lunar crater volume: Interpretation by models of impact cratering and upper crustal structure. Proc Lunar Planet Sci Conf 9:3711-3733
Croft SK (1980) Cratering flow fields: Implications for the excavation and transient expansion stage of crater formation. Proc Lunar Planet Sci Conf 11:2347-2378
Croft SK (1981a) The modification stage of basin formation: Conditions of ring formation. *In*: Multi-Ring Basins. Schultz PH, Merrill RB (eds) Pergamon, p 227-257
Croft SK (1981b) The excavation stage of basin formation: A qualitative model. *In*: Multi-Ring Basins. Schultz PH, Merrill RB (eds) Pergamon, p 207-225
Croft SK (1982) A first-order estimate of shock heating and vaporization in oceanic impacts. *In*: Geological Implications of Impacts of Large Asteroids and Comets on the Earth. GSA Spec Paper 190:143-152
Croft SK (1985) The scaling of complex craters. Proc Lunar Planet Sci Conf 15, In J Geophys Res 89:C828-C842
Culler TS, Becker TA, Muller RA, Renne PR (2000) Lunar impact history from ^{40}Ar/^{39}Ar dating of glass spherules. Science 287:1785-1788
Dahl JM, Schultz PH (2001) Measurement of stress wave asymmetries in hypervelocity projectile impact experiments. Int J Impact Eng 26:145-155
Dalrymple GB (1991) The Age of the Earth. Stanford University Press

Dalrymple GB, Ryder G (1993) $^{40}Ar/^{39}Ar$ ages of Apollo 15 impact melt rocks by laser step heating and their bearing on the history of lunar basin formation. J Geophys Res (Planets) 98:13085-13095

Dalrymple GB, Ryder G (1996) $^{40}Ar/^{39}Ar$ age spectra of Apollo 17 highlands breccia samples by laser step-heating and the age of the Serenitatis basin. J Geophys Res (Planets) 101:26069-26084

Davis D, Weidenschilling SJ, Farinella P, Paolicchi P, Binzel RP (1989) Asteroid collisional history: Effects on sizes and spins. *In*: Asteroids II. Binzel RP, Gehrels T, Matthews MS (eds) Univ Arizona Press, p 805-826

De Hon RA, Waskom JD (1976) Geologic structure of the eastern mare basins. Proc Lunar Sci Conf 7:2729-2746

Dence MR, Grieve RAF, Robertson PB (1977) Terrestrial impact structures: Principal characteristics and energy considerations. *In*: Impact and Explosion Cratering. Roddy DJ, Pepin RO, Merrill RB (eds) Pergamon Press, p 247-276

Deutsch A, Schärer U (1994) Dating terrestrial impact events. Meteoritics 29:301-322

Deutsch A, Stöffler D (1987) Rb-Sr analyses of Apollo 16 melt rocks and a new age estimate for the Imbrium basin: Lunar basin chronology and the early heavy bombardment of the Moon. Geochim Cosmochim Acta 51:1951-1964

Dressler BO, Reimold WU (2001) Terrestrial impact melt rocks and glasses. Earth Sci Rev 56:205-284

Drozd RJ, Hohenberg CM, Morgan CJ, Ralston CE (1974) Cosmic-ray exposure history at the Apollo 16 and other lunar sites: Lunar surface dynamics. Geochim Cosmochim Acta 38:1625-1642

Drozd RJ, Hohenberg CM, Morgan CJ, Podosek FA, Wroge ML (1977) Cosmic-ray exposure history at Taurus-Littrow. Proc Lunar Sci Conf 8:3027-3043

Durda D, Greenberg R, Jedicke R (1998) Collisional models and scaling laws: A new interpretation of the shape of the Main-Belt asteroid distribution. Icarus 135:431-440

Eberhardt P, Geiss J, Grögler N, Stettler A (1973) How old is the crater Copernicus? The Moon 8:104-114

Eugster O (1999) Chronology of dimict breccias and the age of South Ray crater at the Apollo 16 site. Meteorit Planet Sci 34:385-391

Faure G (1986) Principles of Isotope Geology (2nd edition). Wiley

Feldman WC, Gasnault O, Maurice S, Lawrence DJ, Elphic RC, Lucey PG, Binder AB (2002) Global distribution of lunar composition: New results from Lunar Prospector. J Geophys Res 107(E3):5-1–5-14, doi:10.1029/2001JE001506

Florensky CP, Basilevsky AT, Ivanov AV, Pronin AA, Rode OD (1977) Luna 24: Geological setting of landing site and characteristics of sample core (preliminary data). Proc Lunar Sci Conf 8:3257-3279

French BM (1998) Traces of Catastrophe: A handbook of shock-metamorphic effects in terrestrial meteorite impact structures. LPI Contribution No. 954, Lunar and Planetary Institute

French BM, Short NM (1968) Shock Metamorphism of Natural Materials. Mono Book Corporation

Fritz J, Greshake A, Stöffler D (2003) Launch conditions for Martian meteorites: Plagioclase as a shock pressure barometer. Lunar Planet Science XXXIV:1335

Gault DE, Heitowit ED (1963) The partition of energy for hypervelocity impact craters formed in rock. Proc Hypervelocity Impact Symp 6:419-456

Gault DE, Wedekind JA (1978) Experimental studies of oblique impacts. Proc Lunar Planet Sci Conf 9:3843-3875

Gault DE, Quaide WL, Oberbeck VR (1968) Impact cratering mechanics and structures. *In*: Shock Metamorphism of Natural Materials. French BM, Short NM (eds) Mono Book Corporation, p 87-99

Geiss J, Eberhardt P, Grögler N, Guggisberg S, Maurer P, Settler A (1977) Absolute time scale of lunar mare formation and filling. Royal Soc London Phil Trans 285:151-158

Gilbert GK (1893) The Moons face a study of the origin of its features. Phil Soc Wash Bull 12:241-292

Graham AL, Hutchison R (1980) Mineralogy and petrology of fragments from the Luna 24 core. Royal Soc London Phil Trans A 297:15-22

Grier JA, McEwen AS, Lucey PG, Milazzo M, Strom RG (2001) Optical maturity of ejecta from large rayed lunar craters. J Geophys Res 106: 32,847-32862

Grieve RAF (1987) Terrestrial impact structure. Ann Rev Earth Planet Sci 15:245-270

Grieve RAF (1991) Terrestrial impact: the record of the rocks. Meteoritics 26:175-194

Grieve RAF, Cintala MJ (1992) An analysis of differential impact melt-crater scaling and implications for the terrestrial impact record. Meteoritics 27 526–538

Grieve RAF, Garvin JB (1984) A geometric model for excavation and modification at terrestrial simple impact craters. J Geophys Res 89:11561-11572

Grieve RAF, Shoemaker EM (1994) The record of past impacts on Earth. *In*: Hazards Due to Comets and Asteroids. Gehrels T (ed) Univ Arizona Press, p 417-462

Grieve RAF, Pilkington M (1996) The signature of terrestrial impacts. AGSO J Australian Geol Geophys 16:399-420

Grieve RAF, Therriault A (2000) Vredefort, Sudbury, Chicxulub: Three of a kind? Annual Rev Earth Planet Sci 28: 305-338

Grieve RAF, McKay GA, Weill DF (1972) Microprobe studies of three Luna 16 basalt fragments. Earth Planet Sci Lett 13:233-242

Grieve RAF, Robertson PB, Dence MR (1981) Constraints on the formation of ring impact structures based on terrestrial data. Multi-Ring Basins, Proc Lunar Planet Sci 12A:37-57

Grieve RAF, Stöffler D, Deutsch A (1991) The Sudbury Structure - Controversial or misunderstood? J Geophys Res 96: 22,753-22,764
Grieve RAF, Langenhorst F, Stöffler D (1996) Shock metamorphism of quartz in nature and experiment: II. Significance in geoscience. Meteorit Planet Sci 31:6-35
Grieve RAF, Garvin JB, Coderre JM, Rupert J (1989) Test of a geometric model for the modification stage of simple impact crater development. Meteoritics 24:83-88
Grolier MJ (1970a) Geologic map of Apollo site 2 (Apollo 11); Part of Sabine D region, southwestern Mare Tranquillitatis. USGS Map I-619 [ORB II-6 (25)], scale 125000
Grolier MJ (1970b) Geologic map of the Sabine region on the Moon, Lunar Orbiter site II P-6, southwestern Mare Tranquillitatis, including landing site 2. USGS Map I-618 [ORB II-6 (100)], scale 1100000
Hackmann RJ (1966) Geologic map of the Montes Apenninus quadrangle of the Moon. USGS Map I-463 (LAC-41), scale 11000000
Hale WS, Grieve RAF (1982) Volumetric analysis of complex lunar craters: Implications for basin ring formation. Proc Lunar Planet Sci Conf 13, In J Geophys Res 87:A65-A76
Hale WS, Head JW (1979) Central peaks in lunar craters: Morphology and morphometry. Proc Lunar Planet Sci Conf 10:2623-2633
Halliday AN (2000) Terrestrial accretion rates and the origin of the Moon. Earth Planet Sci Lett 176:17-30
Hartmann WK (1965) Terrestrial and lunar flux of meteorites in the last two billion years. Icarus 4:157-165
Hartmann WK (1966) Martian cratering. Icarus 5:565-576
Hartmann WK (1970) Lunar cratering chronology. Icarus 13:299-301
Hartmann WK (1972) Paleocratering of the Moon Review of post-Apollo data. Astrophys Space Science 17:48-64
Hartmann WK (1995) Planetary cratering I: Lunar highlands and tests of hypotheses on crater populations. Meteoritics 30:451-467
Hartmann WK (2003) Megaregolith evolution and cratering cataclysm models – Lunar cataclysm as a misconception (28 years later). Meteorit Planet Sci 38:579-593
Hartmann WK, Neukum G (2001) Crater chronology and the evolution of Mars. *In*: Chronology and Evolution of Mars. Kallenbach R, Geiss J, Hartmann WK (eds) Kluwer Dordrecht, p 165-194
Hartmann WK, Wood CA (1971) Moon: Origin and Evolution of Multi-Ring Basins. The Moon 3:3-78
Hartmann WK, Farinella P, Vokrouhlický D, Weidenschilling SJ, Morbidelli A, Marzari F, Davis DR, Ryan E (1999) Reviewing the Yarkovsky effect: New light on the delivery of stone and iron meteorites from the asteroid belt. Meteorit Planet Sci 34:161-167
Hartmann WK, Phillips RJ, Taylor GJ (1984) Origin of the Moon. Lunar & Planetary Institute
Hartmann WK, Ryder G, Dones L, Grinspoon DH (2000) The time-dependent intense bombardment of the primordial Earth-Moon system. *In*: Origin of the Earth and Moon. Righter RM, Canup R (eds) Univ Arizona Press, p 493-512
Hartmann WK, Strom RG, Weidenschilling SJ, Balsius KR, Woronow A, Dence MR, Grieve RAF, Diaz J, Chapman CR, Shoemaker EM, Jones KL (1981) Chronology of planetary volcanism by comparative studies of planetary craters. *In*: Basaltic Volcanism on the Terrestrial Planets. Pergamon Press, p 1049-1128
Haskin LA (1998) The Imbrium impact event and the thorium distribution at the lunar highlands surface. J Geophys Res 103:1679-1689
Haskin LA, Korotev RL, Gillis JJ, Jolliff BL (2002) Stratigraphies of Apollo and Luna highland landing sites and provenances of materials from the perspective of basin impact ejecta modeling. Lunar Planet Sci XXXIII:1364
Haskin LA, Moss BE, McKinnon WB (2003) On estimating contributions of basin ejecta to regolith deposits at lunar sites. Meteorit Planet Sci 38:13-33
Hawke BR, Head JW (1977) Impact melt on lunar crater rims. *In*: Impact Explosion Cratering. Roddy DJ, Pepin RO, Merrill RB (eds) Pergamon, p 815-841
Hawke BR, Head JW (1978) Lunar KREEP volcanism: Geologic evidence for history and mode of emplacement. Proc Lunar Planet Sci Conf 9:3285-3309
Hayhurst CJ, Ranson HJ, Gardner DJ, Birnman NK (1995) Modelling of microparticle hypervelocity oblique impacts on thick targets. Int J Impact Eng 17:375-386
Head JN, Melosh HJ, Ivanov BA (2002) Martian meteorite launch: High-speed ejecta from small craters. Science 298: 1752-1756
Head JW (1976) The significance of substrate characteristics in determining morphology and morphometry of lunar craters. Proc Lunar Sci Conf 7:2913-2929
Head JW (1977) Origin of outer rings in lunar multi-ring basins: Evidence from morphology and ring spacing. *In*: Impact and Explosion Cratering. Roddy DJ, Pepin RO, Merrill RB (eds) Pergamon, p 567-573
Head JW, Adams JB, McCord TB, Pieters CM, Zisk SH (1978a) Regional stratigraphy and geologic history of Mare Crisium. Lunar and Planetary Institute, compiler, Mare Crisium: The view from Luna 24: Conf on Luna 24, Houston, Texas, 1977 Proceedings. Geochim Cosmochim Acta Supp 9:43-74
Heiken G, Vaniman D, French BM (eds) (1991) The Lunar Sourcebook: A User's Guide to the Moon. Lunar and Planetary Institute and Cambridge Univ Press

Herrick RR, Forsberg-Taylor NK (2003) The shape and appearance of craters formed by oblique impact on the Moon and Venus. Meteorit Planet Sci 38: 1551–1578

Hiesinger H, Head JW, Wolf U, Jaumann R, Neukum G, (2003) Ages and stratigraphy of mare basalts in Oceanus Procellarum, Mare Nubium, Mare Cognitum, and Mare Insularum. J Geophys Res 108(E7):1-1–1-27, doi: 10.1029/2002JE001985

Hildebrand AR, Pilkington M, Connors M, Ortiz-Aleman C, Chavez RE (1995) Size and structure of the Chicxulub crater revealed by horizontal gravity gradients and cenotes. Nature 376:415-417

Holsapple KA (1980) The equivalent depth of burst for impact cratering. Proc Lunar Planet Sci Conf 11:2379-2401

Holsapple KA (1987) The scaling of impact phenomena. Int J Impact Eng 5:343-355

Holsapple KA (1993) The scaling of impact processes in planetary sciences. Ann Rev Earth Planet Sci 21:333-373

Holsapple KA, Schmidt RM (1980) On the scaling of crater dimensions 1 Explosive processes. J Geophys Res 85: 7247-7256

Holsapple KA, Schmidt RM (1982) On the scaling of crater dimensions 2 Impact processes. J Geophys Res 87:1849-1870

Holsapple KA, Schmidt RM (1987) Point source solutions and coupling parameters in cratering mechanics. J Geophys Res 92:6350-6376

Hornemann U, Müller WF (1971) Shock-induced deformation twins in clinopyroxene. Neues Jb Min Mh 6: 247-256

Hörz F (2000) Time-variable cratering rates? Science 288:2095a

Hörz F, Ostertag R, Rainey DA (1983) Bunte Breccia of the Ries: Continuous deposits of large impact craters. Rev Geophys Space Phys 21:1667-1725

Housen KR, Schmidt RM, Holsapple KA (1983) Crater ejecta scaling laws: Fundamental forms from dimensional analysis. J Geophys Res 88:2485-2499

Howard KA (1974) Fresh lunar impact craters: Review of variations with size. Proc Lunar Sci Conf 5:61-69

Howard KA, Wilshire HG (1975) Flows of impact melt in lunar craters. J Res US Geological Survey 3:237-251

Hughes DW (2000) A new approach to the calculation of the cratering rate of the Earth over the last 125±20 Ma. Monthly Notices Royal Astron Soc 317:429-437.

Huneke JC, Podosek FA, Wasserburg GJ (1972) Gas retention and cosmic-ray exposure ages of a basalt fragment from Mare Fecunditatis. Earth Planet Sci Lett 13:375-383

Ivanov BA (1994) Geomechanical models of impact cratering: Puchezh-Katunki structure. *In*: Large Meteorite Impacts and Planetary Evolution. Dressler BO, Grieve RAF, Sharpton VL (eds) GSA Spec Paper **293**:81-91

Ivanov BA (2001) Mars/moon cratering rate ratio estimates. *In*: Chronology and Evolution of Mars. Kallenbach R, Geiss J, Hartmann WK (eds) Kluwer Dordrecht, p 87-104

Ivanov BA (2002) Deep drilling results and numerical modeling Puchezh-Katunki impact crater, Russia. Lunar Planetary Science XXXIII:1286

Ivanov BA, Artemieva NA (2001) Transient cavity scaling for oblique impacts. Lunar Planetary Science XXXII:1327

Ivanov BA, Artemieva NA (2002) Numerical modeling of the formation of large impact craters. *In*: Catastrophic Events and Mass Extinctions: Impact and Beyond. GSA Spec Paper 356:619-630

Ivanov BA, Basilevsky AT, Neukum G (1997) Atmospheric entry of large meteoroids: Implication to Titan. Planet Space Sci 45:993-1007

Ivanov BA, Neukum G, Wagner R (1999) Impact craters NEA and Main Belt asteroids Size-frequency distribution. Lunar Planet Sci XXX:1583

Ivanov BA, Neukum G, Wagner R (2001) Size-frequency distributions of planetary impact craters and asteroids. *In*: Collisional Processes in the Solar System. Rickman H, Marov M (eds) Kluwer, p 1-34

Ivanov BA, Neukum G, Bottke W, Hartmann WK (2003) The comparison of size-frequency distributions of impact craters and asteroids and the planetary cratering rate. *In*: Asteroids III. Bottke W, Cellino A, Paolicchi P, Binzel RP (eds) University Arizona Press, p 89-101

Ivezic Z, Tabachnik S, Rafikov R, Lupton RH, Quinn T, Hammergren M, Eyer L, Chu J, Armstrong JC, Fan X, Finlator K, Geballe TR, Gunn JE, Hennessy GS, Knapp GR, Leggett SK, Munn JA, Pier JR, Rockosi CM, Schneider DP, Strauss MA, Yanny B, Brinkmann J, Csabai I, Hindsley RB, Kent S, Lamb DQ, Margon B, McKay TA, Smith JA, Waddel P, York DG, and the SDSS Collaboration (2001) Solar system objects observed in the Sloan Digital Sky Survey Commissioning Data. Astron J 122:2749-2784

James OB (1981) Petrologic and age relations of the Apollo 16 rocks: Implications for the subsurface geology and the age of the Nectaris basin. Proc Lunar Planet Sci Conf 12:209-233

Jedicke R, Metcalfe TS (1998) The orbital absolute magnitude distributions of Main Belt asteroids. Icarus 131:245-260

Jessberger EK (1983) ^{40}Ar-^{39}Ar dating of North Ray Crater ejecta I. Lunar Planet Sci XIV:349-350

Jessberger EK, Kirsten T, Staudacher T (1977) One rock and many ages - further data on consortium breccia 73215. Proc Lunar Sci Conf 8:2567-2580

Jolliff BL, Rockow KM, Korotev RL, Haskin LA (1996) Lithologic distribution and geologic history of the Apollo 17 site: The record in soils and small rock particles from the highland massifs. Meteor Planet Sci 31:116-145

Jolliff BL, Gillis JJ, Korotev RL, Haskin LA (2000a) On the origin of nonmare materials at the Apollo 12 landing site. Lunar Planet Sci XXXII:1671

Jolliff BL, Gillis JJ, Haskin LA, Korotev RL, Wieczorek MA (2000b) Major lunar crustal terranes: Surface expressions and crust-mantle origins. J Geophys Res (Planets) 105:4197-4216
Keil K, Kurat G, Prinz M, Green JA (1972) Lithic fragments glasses and chondrules from Luna 16 fines. Earth Planet Sci Lett 13:243-256
Kettrup B, Deutsch A, Masaitis VL (2003) Homogeneous impact melts produced by a heterogeneous target? Sr-Nd isotopic evidence from Popigai crater, Russia. Geochim Cosmochim Acta 67:733-750
Kieffer SW (1977) Impact conditions required for formation of melt by jetting of silicates. *In*: Impact and Explosion Cratering. Roddy DJ, Pepin RO, Merrill RB (eds) Pergamon Press, p 751-769
Kieffer SW, Schaal RB, Gibbons RV, Hörz F, Milton DJ, Dube A (1976) Shocked Basalt from Lonar Impact Crater, Indis, and Experimental Analogues. Proc Lunar Sci Conf 7:1391-1412
Kitamura M, Goto T, Syono Y (1977) Intergrowth textures of diaplectic glass and crystal in shock loaded P-anorthite. Contr Mineral Petrol 61:299-304
Kitamura M., Tsuchiyama A, Watanabe S, Syono Y, Fukuoka K (1992) Shock recovery experiments on chondritic material. *In*: High-Pressure Research: Applications to Earth and Planetary Sciences. Syono Y, Manghnani MH (eds) Terra Sci. Publ., p 33-34
Korotev RL (1987) Mixing levels the Apennine Front soil component and compositional trends in the Apollo 15 soils. Proc Lunar Planet Sci Conf 17:E411-E431
Korotev RL, Jolliff BL, Zeigler RA (2000) The KREEP components of the Apollo 12 regolith. Lunar Planet Sci XXXI: 1363
Kring DA, Cohen BA (2002) Cataclysmic bombardment throughout the inner solar system 3.9-4.0 Ga. J Geophys Res 107(E2):4-1–4-6
Kurat G, Kracher A, Keil K, Warner R, Prinz M (1976) Composition and origin of Luna 16 aluminous mare basalts. Proc Lunar Sci Conf 7:1301-1321
Lakomy R (1990) Implications for cratering mechanics from a study of the Footwall Breccia of the Sudbury impact structure, Canada. Meteoritics 25:195-207
Landau LD, Lifshitz EM (1987) Fluid Mechanics. Pergamon Press
Lee DC, Halliday AN, Snyder GA, Taylor LA (1997) Age and origin of the Moon. Science 278:1098-1103
Love S, Ahrens TJ (1996) Catastrophic impacts on gravity dominated asteroids. Icarus 124:141-155
Lucchitta BK (1977) Crater clusters and light mantle at the Apollo 17 site: A result of secondary impact from Tycho. Icarus 30:80-96
Lucchitta BK, Sanchez AG (1975) Crater studies in the Apollo 17 region. Proc Lunar Sci Conf 6:2427-2441
Ma MS, Schmitt RA, Nielsen RL, Taylor GJ, Warner RD, Keil K (1979) Petrogenesis of Luna 16 aluminous mare basalts. Geophys Res Lett 6:909-912
Maurer P, Eberhardt P, Geiss J, Grögler N, Stettler A, Brown GM, Peckett A, Krähenbühl U (1978) Pre-Imbrian craters and basins Ages compositions and excavation depths of Apollo 16 breccias. Geochim Cosmochim Acta 42:1687-1720
Maxwell DE (1973) Cratering Flow and Crater Prediction Methods. Physics International Co
Maxwell DE (1977) Simple Z model of cratering, ejection, and overturned flap. *In*: Impact and Explosion Cratering. Roddy DJ, Pepin RO, Merrill RB (eds) Pergamon, p 1003-1008
McCormick KA, Taylor GJ, Keil K, Spudis PD, Grieve RAF, Ryder G (1989) Sources of clasts in terrestrial impact melts: Clues to the origin of LKFM. Proc Lunar Planet Conf 19:691-696
McGetchin TR, Settle M, Head JW (1973) Radial thickness variation in crater ejecta: Implications for lunar basin models. Earth Planet Sci Lett 20:226-236
Melosh HJ (1984) Impact ejection spallation and the origin of meteorites. Icarus 59:234-260
Melosh HJ, Sonett CP (1986) When worlds collide: Jetted vapor plumes and the Moon's origin. *In*: Origin of the Moon. Hartmann WK, Phillips RJ, Taylor GJ (eds) Lunar and Planetary Institute, p 621–642
Melosh HJ (1989) Impact Cratering - A Geologic Process. Oxford Univ Press
Melosh HJ, Ivanov BA (1999) Impact crater collapse. Ann Rev Earth Planetary Science 27:385-415
Melosh HJ, Ryan EV (1997) Asteroids shattered but not dispersed. Icarus 129:562-564
Meyer C Jr, Brett R, Hubbard NJ, Morrison DA, McKay DS, Aitken FK, Takeda H, Schonfeld E (1971) Mineralogy, chemistry and origin of the KREEP component in soil samples from the Ocean of Storms. Proc Lunar Sci Conf 2:393-411
Mileikowsky C, Cucinotta FA, Wilson JW, Gladman B, Horneck G, Lindegren L, Melosh HJ, Rickmann H, Valtonen M, Zheng JQ (2000) Natural transfer of viable microbes in space - 1. From Mars to Earth and Earth to Mars. Icarus 145:391-427
Morbidelli A, Petti JM, Gladman B, Chambers J (2001) A plausible cause of the late heavy bombardment. Meteorit Planet Sci 36:371-380
Moore HJ, Hodges CA, Scott DH (1974) Multi-ringed basins - Illustrated by Orientale and associated features. Proc Lunar Sci Conf 5:71-100
Moore HJ, Boyce JM, Hahn DA (1980) Small impact craters in the lunar regolith - their morphologies relative ages and rates of formation. The Moon and the Planets 23:231-252
Morgan J, Warner M (1999) Chicxulub: The third dimension of a multi-ring impact basin. Geology 27:407-410

Muehlberger WR, Hörz F, Sevier JR, Ulrich GE (1980) Mission objectives for geological exploration of the Apollo 16 landing site. Proceedings of the Lunar and Planetary Institute compiler Conf on the Lunar Highland Crust, Houston, Texas 1979. Geochim Cosmochim Acta suppl. 12:1-49

Müller WF, Hornemann U (1969) Shock-induced planar deformation structures in experimentally shock-loaded olivines and in olivines from chondritic meteorites. Earth Planet Sci Lett 7:251-264

Muller RA, Becker TA, Culler TS, Karner DB, Renne PR (2000) Time-variable cratering rates? Science 288:2095a

Neal CR, Taylor LA, Hughes SS, Schmitt RA (1990) The significance of fractional crystallization in the petrogenesis of Apollo17 type A and B high-Ti basalts. Geochim Cosmochim Acta 54:1817-1833

Neal CR, Hacker MD, Snyder GA, Taylor LA, Liu Y-G, Schmitt RA (1994) Basalt generation at the Apollo 12 site. Part 1: New data classification and re-evaluation. Meteoritics 29:334-348

Nemtchinov IV, Shuvalov VV, Kosarev IB, Artemieva NA, Trubetskaya IA, Svetsov VV, Ivanov BA, Loseva TV, Neukum G, Hahn G, de Niem D (1997) Assessment of comet Shoemaker-Levy 9 fragment sizes using light curves measured by Galileo spacecraft instruments. Planet Space Sci 45:311-326

Neukum G (1977) Different ages of lunar light plains. The Moon 17:383-393

Neukum G (1983) Meteoritenbombardement und Datierung planetarer Oberflächen. Habilitation Dissertation for Faculty Membership Ludwig-Maximilians-University Munich, 186 p

Neukum G, Ivanov BA (1994) Crater size distribution and impact probabilities on Earth from lunar terrestrial-planet and asteroid cratering data. *In*: Hazards Due to Comets and Asteroids. Gehrels T (ed) Univ Arizona Press, p 359-416

Neukum G, König B (1976) Dating of individual lunar craters. Proc Lunar Sci Conf 7:2867-2881

Neukum G, Wise DU (1976) Mars: A standard crater curve and possible new time scale. Science 194:1381-1387

Neukum G, König B, Arkani-Hamed J (1975a) A study of lunar impact crater size-distributions. The Moon 12:201-229

Neukum G, König B, Fechting H, Storzer D (1975b) Cratering in the Earth-moon system: Consequences for age determination by crater counting. Proc Lunar Sci Conf 6:2597-2620

Neukum G, Ivanov B, Hartmann WK (2001) Cratering records in the inner solar system. *In*: Chronology and Evolution of Mars. Kallenbach R, Geiss J, Hartmann WK (eds) Kluwer, p 55-86

Nozette S and the Clementine team (1994) The Clementine mission to the Moon: Scientific overview. Science 266: 1835-1839

Nyquist LE, Shih CY (1992) The isotopic record of lunar volcanism. Geochim Cosmochim Acta 56:2213-2234

Nyquist LE, Bogard DD, Shih CY (2001) Radiometric chronology of Moon and Mars. *In:* The Century of Space Science. Kluwer Publishers, p 1325-1376

Oberbeck VR (1975) The role of ballistic erosion and sedimentation in lunar stratigraphy. Rev Geophys Space Phys 13:337-362

Oberbeck VR, Morrison RH (1976) Candidate areas for *in situ* ancient lunar materials. Proc Lunar Sci Conf 7:2983-3005

Oberbeck VR, Morrison RH, Hörz F, Quaide WL, Gault DE (1974) Smooth plains and continuous deposits of craters and basins. Proc Lunar Sci Conf 5:111-136

Oberbeck VR, Hörz F, Morrison RH, Quaide WL, Gault DE (1975) On the origin of the lunar smooth-plains. The Moon 12:19-54

O`Keefe JD, Ahrens TJ (1977) Impact-induced energy partitioning melting and vaporization on terrestrial planets. Proc Lunar Sci Conf 8:3357-3374

O`Keefe JD, Ahrens TJ (1999) Complex craters: Relationship of stratigraphy and rings to impact conditions. J Geophys Res 104:27091-27104

Öpik EJ (1971) Cratering and the Moons surface. Academic Press

Orphal DL, Borden WF, Larson SA, Schultz PH (1980) Impact melt generation and transport. Proc Lunar Planet Sci Conf 11:2309-2323

Ostertag R (1983) Shock experiments on feldspar crystals. Proc Lunar Planet Sci Conf 14, In J Geophys Res (Suppl) 88:B364-B376

Palme H, Janssens M-J, Takahashi H, Anders E, Hertogen J (1978) Meteoritic material at five large impact craters. Geochim Cosmochim Acta 42:313-323

Papanastassiou DA, Wasserburg GJ (1972) The Rb-Sr age of a crystalline rock from Apollo 16. Earth Planet Sci Lett 16:289-298

Papike JJ, Ryder G, Shearer CK (1998) Lunar samples. Rev Mineral 36:5-1–5-234

Phinney WC, Simonds CH (1977) Dynamical implications of the petrology and distribution of impact melt rocks. *In*: Impact and Explosion Cratering. Roddy DJ, Pepin RP, Merrill RB (eds) Pergamon, p 771-790

Pierazzo E, Melosh HJ (2000a) Hydrocode modeling of oblique impacts: The fate of the projectile. Meteorit Planet Sci 35:117-130

Pierazzo E, Melosh HJ (2000b) Understanding oblique impacts from experiments, observations and modeling. Ann Rev Earth Planet Sci 28: 141-167

Pierazzo E, Melosh HJ (2000c) Melt production in oblique impacts. Icarus 145:252-261

Pierazzo E, Vickery AM, Melosh HJ (1997) A re-evaluation of impact melt production. Icarus 127:408-423

Pieters CM, Head JW, Gaddis L, Jolliff B, Duke M (2001) Rock types of South Pole- Aitken Basin and extent of basaltic volcanism. J Geophys Res 106:28001-28022
Pike RJ (1974) Depth/diameter relations of fresh lunar craters: Revision from spacecraft data. Geophys Res Letters 1: 291-294
Pike RJ (1977a) Size-dependence in the shape of fresh impact craters on the Moon. *In*: Impact and Explosion Cratering. Roddy DJ, Pepin RO, Merrill RB (eds) Pergamon, p 489-510
Pike RJ (1977b) Apparent depth/apparent diameter relations for lunar craters. Proc Lunar Sci Conf 8:3427-3436
Pike RJ (1980a) Formation of complex impact structures: Evidence from Mars and other planets. Icarus 43:1-19
Pike RJ (1980b) Geometric Interpretation of Lunar Craters. US Geol Survey Prof Paper 1046-C, US Govt Printing Office
Pike RJ (1985) Some morphologic systematics of complex impact structures. Meteoritics 20:49-68.
Pike RJ (1988) Geomorphology of impact craters on Mercury. *In*: Mercury. Vilas F, Chapman CR, Matthews MS (eds) Univ. Arizona Press, p 165-273
Pike RJ, Spudis P (1987) Basin-ring spacing on the Moon, Mercury, and Mars. Earth, Moon, and Planets 39:129-194
Podosek FA, Huneke JC, Gancarz AJ, Wasserburg GJ (1973) The age and petrography of two Luna 20 fragments and inferences for widespread lunar metamorphism. Geochim Cosmochim Acta 37:887-904
Pohl J, Stöffler D, Gall H, Ernstson K (1977) The Ries impact crater. *In*: Impact and Explosion Cratering. Roddy DJ, Pepin RP, Merrill RB (eds) Pergamon, p 343-404
Pye EG, Naldrett AJ, Giblin PE (1984) The Geology and Ore Deposits of the Sudbury Structure. Ontario Geological Survey Special Volume 1
Rabinowitz D, Helin E, Lawrence K, Pravdo S (2000) A reduced estimate of the number of kilometre-sized near-Earth asteroid. Nature 403:165-166
Ravine MA, Grieve RAF (1986) An analysis of morphologic variation in simple lunar craters. Proc Lunar Planet Sci Conf 17, In J Geophys Res 91:E75-E83
Reid AM, Ridley WI, Harmon RS, Warner JL, Brett R, Jakes P, Brown RW (1972) Highly aluminous glasses in lunar soils and the nature of the lunar highlands. Geochim Cosmochim Acta 36:903-912
Reimold WU, Stöffler D (1978) Experimental shock metamorphism of dunite. Proc Lunar Planet Sci Conf 9:2805-2824
Rhodes JM, Blanchard DP, Dungan MA, Brannon JC, Rodgers KV (1977) Chemistry of Apollo 12 mare basalts: Magma types and fractionation processes. Lunar Science Conf 8:1305-1338
Robertson PB, Grieve RAF (1977) Shock attenuation at terrestrial impact structures. *In*: Impact and Explosion Cratering. Roddy DJ, Pepin RP, Merrill RB (eds) Pergamon, p 687-702
Roddy DJ, Pepin RO, Merrill RB (eds) (1977) Impact and Explosion Cratering. Pergamon Press
Russel SS, Zolensky M, Righter K, Folco L, Jones R, Connolly HC Jr, Grady MM, Grossman JN (2006) The Meteoritical Bulletin, Bo. 89, 2005 September. Meteor Planet Sci 40:A201-A263
Ryder G (1981) Distribution of rocks at the Apollo 16 landing site. *In*: Workshop on Apollo 16. LPI Tech Rpt 81-01. James OB, Hörz F (eds) Lunar and Planetary Institute, p 112-119
Ryder G (1985) Catalog of Apollo 15 rocks. JSC Publ No 20787, Curatorial Branch Publ 72, NASA Johnson Space Center
Ryder G (1987) Petrographic evidence for nonlinear cooling rates and a volcanic origin for Apollo 15 KREEP basalts. Proc Lunar Planet Sci Conf 17, In J Geophys Res 92:E331-E339
Ryder G (1990a) Lunar samples, lunar accretion and the early bombardment of the Moon. EOS Trans Amer Geophys Union 71:313-333
Ryder G (1990b) A distinct variant of high-titanium mare basalt from the Van Serg core Apollo 17 landing site. Meteoritics 25:249-258
Ryder G (1994) Coincidence in time of the Imbrium basin impact and the Apollo 15 volcanic flows: The case for impact-induced melting. Geol Soc Am Spec Paper 293:11-18
Ryder G (2000) Glass beads tell a tale of lunar bombardment. Science 287:1768-1769
Ryder G, Marvin UB (1978) On the origin of Luna 24 basalts and soils. *In*: Mare Crisium: The View from Luna 24. Merrill RB, Papike JJ (eds) Pergamon, p 339-355
Ryder G, Schuraytz BC (2001) The chemical variation of the large Apollo 15 olivine-normative mare basalt rock samples. J Geophys Res 106(E1):1435-1451
Ryder G, Spudis PD (1987) Chemical composition and origin of Apollo 15 impact melts. Proc Lunar Planet Sci Conf 17, in J Geophys Res 92:E432-E446
Ryder G, Bogard DD, Garrison D (1991) Probable age of Autolycus and calibration of lunar stratigraphy. Geology 19: 143-146
Schaal RB, Hörz F (1977) Shock metamorphism of lunar and terrestrial basalts. Proc Lunar Sci Conf 8:1697- 1729
Schaal RB, Hörz F (1980) Experimental shock metamorphism of lunar soil. Proc Lunar Planet Sci Conf 11:1679-1695
Schaal RB, Hörz F, Thompson TD, Bauer JF (1979) Shock Metamorphism of granulated lunar basalt. Proc Lunar Planet Sci Conf 10:2547-2571

Schmidt RM (1977) A centrifuge cratering experiment: Development of a gravity-scaled yield parameter. *In*: Impact and Explosion Cratering. Roddy DJ, Pepin RP, Merrill RB (eds) Pergamon, p 1261-1278
Schmidt RM (1980) Meteor crater energy of formation - implications of centrifuge scaling. Proc Lunar Planet Sci Conf 11:2099-2128
Schmidt RM, Holsapple KA (1978) A gravity-scaled energy parameter relating impact and explosive crater size. EOS, Trans Amer Geophys Union 59:1121
Schmidt RM, Holsapple KA (1982) Estimates of crater size for large-body impact: Gravity-scaling results. *In*: Geological Implications of the Impacts of Large Asteroids and Comets on the Earth. GSA Spec Paper 190:93-102
Schmidt RM, Housen KR (1987) Some recent advances in the scaling of impact and explosion cratering. Int J Impact Engin 5:543-560
Schmitt RT (2000) Shock experiments with the H6 chondrite Kernouvé: Pressure calibration of microscopic shock effects. Meteorit Planet Sci 35:545-560
Schultz PH (1976) Moon Morphology. Univ Texas Press
Schultz PH (1988) Cratering on Mercury: A relook. *In*: Mercury. Vilas F, Chapman CR, Matthews MS (eds) University of Arizona Press, p 274-335
Schultz PH (1996) Effect of impact angle on vaporization. J Geophys Res 101(E9):21117-21136
Schultz PH, Gault DE (1975) Seismic effects from major basin formations on the moon and Mercury. Moon 12, 159-177
Schultz PH, Gault DE (1985) Clustered impacts: Experiments and implications. J Geophys Res 90:3701-3732
Schultz PH, Gault DE (1990) Prolonged global catastrophes from oblique impacts. *In*: Global Catastrophes in Earth History: An Interdisciplinary Conf on Impacts Volcanism and Mass Mortality. GSA Spec Paper 247:239-261
Schultz PH, Merrill RB (eds) (1981) Multi-Ring-Basins. Proc Lunar Planet Sci Conf 12A. Pergamon
Schultz PH, Spudis PH (1983) The beginning and end of lunar mare volcanism. Nature 302:233-236
Schultz PH, Mustard JF (2004) Impact melts and glasses on Mars. J Geophys Res 109(E01001) doi:10.1029/2002JE002025
Schultz PH, Orphal D, Miller B, Borden WF, Larson SA (1981) Multi-ring basin formation: Possible clues from impact cratering calculations. Proc Lunar Planet Sci Conf (Multiring Basins) 12A:181-195
Sharpton VL, Burke K, Camargo-Zanoguera A, Hall SA, Lee DS, Marin LE, Suarez-Reynoso G, Quezada-Muneton JM, Spudis PD, Urrutia-Fucugauchi J (1993) Chicxulub multi-ring impact basin size and other characteristics derived from gravity analysis. Science 261:1564-1567
Shoemaker EM (1962) Interpretation of lunar craters. *In*: Physics and Astronomy of the Moon. Kopal Z (ed) Academic Press, p 283-359
Shoemaker EM, Hackman RJ (1962) Stratigraphic basis for a lunar time scale. *In*: The Moon. Kopal Z, Mikhailov ZK (eds) Academic Press, p 289-300
Shoemaker EM, Weissman PR, Shoemaker CS (1994) The flux of periodic comets near earth. *In*: Hazards Due to Comets and Asteroids. Gehrels T (ed) Univ Arizona Press, p 313-336
Shuvalov VV (2002) Displacement of target material due to impact. Lunar Planet Sci XXXIII:1259
Silver LT (1971) U-Th-Pb isotope systems in Apollo 11 and 12 regolithic materials and a possible age for the Copernican impact. EOS, Trans Amer Geophys Union 52:534
Smith EI, Sanchez AG (1973) Fresh lunar craters: Morphology as a function of diameter a possible criterion for crater origin. Modern Geology 4:51-59
Snee LW, Ahrens TJ (1975) Shock-induced deformation features in terrestrial peridot and lunar dunite. Proc Lunar Sci Conf 6:833-842
Snyder GA, Borg LE, Nyquist LE, Taylor LA (2000) Chronology and isotopic constraints on lunar evolution. *In:* The Origin of the Earth and the Moon. Univ Arizona Press, p 361-395
Soderblom LA (1970) A model for small-impact erosion applied to the lunar surface. J Geol Res 75:2655-2661
Soderblom LA, Lebofsky LA (1972) Technique for rapid determination of relative ages of lunar areas from orbital photography. J Geophys Res 77:279-296
Spangler RR, Warasila R, Delano LW (1984) ^{40}Ar-^{39}Ar ages for the Apollo 15 green and yellow volcanic glasses. Proc Lunar Planet Sci Conf 14:B487-B497
Spray JG, Thompson LM (1995) Friction melt distribution in terrestrial multi-ring impact basins. Nature 373:130-132
Spudis PD (1978) Composition and origin of the Apennine Bench Formation. Proc Lunar Planet Sci Conf 9:3379-3394
Spudis PD (1993) The Geology of Multi-ring Impact Basins: The Moon and Other Planets. Cambridge University Press
Spudis PD, Ryder G (1981) Apollo 17 impact melts and their relation to the Serenitatis basin Multi-ring basins. Proc Lunar Planet Sci Conf 12:133-148
Spudis PD, Hawke BR, Lucey PG (1984) Composition of Orientale Basin deposits and implications for the lunar basin-forming process. Proc Lunar Planet Sci Conf 15, In J Geophys Res 89:C197-C210
Spudis PD, Ryder G, Taylor GJ, McCormick KA, Keil K, Grieve RAF (1991) Sorces of mineral fragments in impact melts 15445 and 15455: Towards an origin of Low-K Frau Mauro basalt. Proc Lunar Planet Sci Conf 21:151-165

Stadermann FJ, Heusser E, Jessberger EK, Lingner S, Stöffler D (1991) The case for a younger Imbrium basin: New ^{40}Ar-^{39}Ar ages of Apollo 14 rocks. Geochim Cosmochim Acta 55:2339-2349

Stähle V (1972) Impact glasses from the suevite of the Nördlinger Ries. Earth Planet Sci Lett 17:275-293

Staid MI, Pieters CM (2001) Mineralogy of the last lunar basalts: Results from Clementine. J Geophys Res 106(E11): 27,887-27,900

Staid MI, Pieters CM, Head JW III (1996) Mare Tranquillitatis Basalt emplacement history and relation to lunar samples. J Geophys Res (Planets) 101:23,213-23,228

Staudacher T, Jessberger EK, Dominik B, Kirsten T, Schaeffer OA (1982) ^{40}Ar - ^{39}Ar ages of rocks and glasses from the Nördlinger Ries crater and the temperature history of impact breccias. J Geophys 51:1-11

Steiger RH, Jäger E (1977) Subcommision on Geochronology: Convention on the use of decay constants in geo- and cosmochronology. Earth Planet Sci Lett 36:359-362

Stephan T, Jessberger E (1992) Isotope systematics and shock-wave metamorphism III K-Ar in experimentally and naturally shocked rocks; the Haughton impact structure, Canada. Geochim Cosmochim Acta 56:1591-1605

Stöffler D (1972) Deformation and transformation of rock-forming minerals by natural and experimental shock processes. I. Behavior of minerals under shock compression. Fortschr Mineral 49:5477-5488

Stöffler D (1974) Deformation and transformation of rock forming minerals by natural and experimental shock processes. II. Physical properties of shocked minerals. Fortschr Mineral 51:256-289

Stöffler D (1984) Glasses formed by hypervelocity impact. Journal Non-Cryst Solids 67:465- 502

Stöffler D, Hornemann U (1972) Quartz and feldspar glasses produced by natural and experimental shock. Meteoritics (**7**):371-394

Stöffler D, Reimold WU (1978) Experimental shock metamorphism of dunite. Proc Lunar Planet Sci Conf 9:2805-2824

Stöffler D, Langenhorst F (1994) Shock metamorphism of quartz in nature and experiment: I. Basic observation and theory. Meteoritics 29:155-181

Stöffler D, Grieve RAF (1994) Classification and nomenclature of impact metamorphic rocks: a proposal to the IUGS Subcommission on the Systematics of Metamorphic Rocks. Lunar Planet Sci XXV:1347

Stöffler D, Grieve RAF (1996) IUGS classification and nomenclature of impact metamorphic rocks: Towards a final proposal. International Symposium on the Role of Impact Processes in the Geological and Biological Evolution of Planet Earth, Postojna, Slovenia, 27.9.-2.10.1996, Abstract

Stöffler D, Ryder G (2001) Stratigraphy and isotope ages of lunar geologic units: Chronological standard for the inner solar system. *In*: Chronology and Evolution of Mars. Kallenbach R, Geiss J, Hartmann WK (eds) Kluwer, p 9-54

Stöffler D, Grieve RAF (2006) Towards a unified nomenclature of metamorphic petrology: 11. Impactites - A proposal on behalf of the IUGS Subcommission on the Systematics of Metamorphic Rocks. IUGS Blackwell Publishers (in press)

Stöffler D, Gault DE, Wedekind J, Polkowski G (1975) Experimental hypervelocity impact into quartz sand Distribution and shock metamorphism of ejecta. J Geophys Res 80:4062-4077

Stöffler D, Knöll HD, Maerz U. (1979) Terrestrial and lunar impact breccias and the classification of the lunar highland rocks. Proc Lunar Planet Sci Conf 10:639-675

Stöffler D, Knöll HD, Marvin UB, Simonds CH, Warren PH (1980) Recommended classification and nomenclature of lunar highland rocks - a committee report. Proceedings of the Lunar and Planetary Institute compiler Conf on the Lunar Highlands Crust, Houston, Texas 1979. Geochim Cosmochim Acta suppl 12:51-70

Stöffler D, Ostertag R, Reimold WU, Borchardt R, Malley J, Rehfeldt A (1981) Distribution and provenance of lunar highland rock types at North Ray Crater Apollo 16. Proc Lunar Planet Sci Conf 12:185-207

Stöffler D, Bischoff A, Borchardt R, Burghele A, Deutsch A, Jessberger EK, Ostertag R, Palme H, Spettel B, Reimold WU, Wacker K, Wänke H (1985) Composition and evolution of the lunar crust in the Descartes Highlands Apollo 16. Proc Lunar Planet Sci Conf 15, In J Geophys Res 89:C449-C506

Stöffler D, Ostertag R, Jammes C, Pfannschmidt G, Sen Gupta PR, Simon SB, Papike JJ, Beauchamp RH (1986) Shock metamorphism and petrography of the Shergotty achondrite. Geochim Cosmochim Acta 50:889-903

Stöffler D, Bischoff L, Oskierski W, Wiest B (1988a) Structural deformation, breccia formation, and shock metamorphism in the basement of complex terrestrial impact craters: implications for the cratering process. *In*: Deep drilling in crystalline bedrock. Volume 1. Boden A, Eriksson KG (eds) Springer-Verlag, p 277-297

Stöffler D, Bischoff A, Buchwald V, Rubin AE (1988b) Shock effects in meteorites. *In*: Meteorites and the early solar system. Kerridge JF, Matthews MS (eds) University of Arizona Press, p 165-202

Stöffler D, Bobe KD, Jessberger EK, Lingner S, Palme H, Spettel B, Stadermann F, Wänke H (1989) Fra Mauro Formation Apollo 14. IV. Synopsis and synthesis of consortium studies. *In*: Workshop on Moon in Transition Apollo 14 KREEP and evolved lunar rocks. Taylor GJ, Warren PH (eds) LPI Tech Rpt 89-03:145-148

Stöffler D, Keil K, Scott RD (1991) Shock metamorphism of ordinary chondrites. Geochim Cosmochim Acta 55: 3845- 3867

Stöffler D, Deutsch A, Avermann M, Bischoff L, Brockmeyer P, Buhl D, Lakomy R, Müller-Mohr V (1994) The formation of the Sudbury structure, Canada: Toward a unified impact model. GSA Spec Pap 293:303-318

Stöffler D, Artemieva NA, Pierazzo E (2002) Modeling the Ries-Steinheim impact event and the formation of the moldavite strewn field. Meteorit Planet Sci 37:1893-1907

Strom RG, Neukum G (1988) The cratering record on Mercury and the origin of impacting objects. *In*: Mercury. Vilas F, Chapman CR, Matthews MS (eds) University of Arizona Press, p 336-373
Strom RG, Croft SK, Barlow NG (1992) The Martian impact cratering record. *In*: Mars. Kieffer HH, Jakosky BM, Snyder C, Matthews MS (eds) Univ Arizona Press, p 383-423
Stuart JS (2001) A near-Earth asteroid population estimate from the LINEAR survey. Science 294:1691-1693
Sugita S, Schultz PH (1999) Spectroscopic characterization of hypervelocity jetting: Comparison with a standard theory. J Geophys Res 104(E12):30825-30845
Swindle TD, Spudis PD, Taylor GJ, Korotev RL, Nichols RH Jr, Olinger CT (1991) Searching for Crisium basin ejecta: Chemistry and ages of Luna 20 impact melts. Proc Lunar Planet Sci Conf 21:167-181
Tagle RA, Erzinger J, Hecht L, Schmitt RT, Stöffler D, Claeys P (2004) Platinum group elements in impactites of the ICDP Chicxulub drill core Yaxcopoil-1: Are there traces of the projectile? Meteorit Planet Sci 39:1009-1016
Taylor SR (1975) Lunar Science: A post-Apollo View. Pergamon
Taylor SR (1982) Planetary Science: A Lunar Perspective. Lunar and Planetary Institute
Taylor LA, Onorato PIK, Uhlmann DR, Coish RA (1978) Subophitic basalts from Mare Crisium: Cooling rates. *In*: Mare Crisium: The View from Luna 24. Merrill RB, Papike JJ (eds) Pergamon, p 473-482
Tera F, Wasserburg GJ (1976) Lunar ball games and other sports. Lunar Planet Sci VII:858-860
Tera F, Papanastassiou DA, Wasserburg GJ (1974) Isotopic evidence for a terminal lunar cataclysm. Earth Planet Sci Lett 22:1-21
Therriault AM, Fowler AD, Grieve RAF (2002) The Sudbury Igneous Complex: A differentiated impact melt sheet. Econ Geol 97:1521-1540
Thompson SL, Lauson HS (1972) Improvements in the Chart-D radiation hydrodynamic code. III. Revised analytical equation of state. Tech Rep SC-RR-710714 Sandia Nat Labs
Tompkins S, Pieters CM (1999) Mineralogy of the lunar crust: results from Clementine. Meteorit Planet Sci 34:25-41
Turner G (1977) Potassium-argon chronology of the Moon. Phys Chem Earth 10:145-195
Ulrich GE, Hodges CA, Muehlberger WR (eds) (1981) Geology of the Apollo 16 area central lunar highlands. USGS Professional Paper 1048
Vinogradov AP (1971) Preliminary data on lunar ground brought to Earth by automatic probe "Luna 16". Proc Lunar Sci Conf 2:1-16
Vinogradov AP (1973) Preliminary data on lunar soil collected by the Luna 20 unmanned spacecraft. Geochim Cosmochim Acta 37:721-729
Wacker K, Müller N, Jessberger EK (1983) ^{40}Ar-^{39}Ar dating of North Ray Crater ejecta II. Meteoritics 18:201
Warner RD, Taylor GJ, Conrad GH, Northrup HR, Barker S, Keil K, Ma MS, Schmitt R (1979) Apollo 17 high-Ti mare basalts: New bulk compositional data, magma types and petrogenesis. Proc Lunar Planet Sci Conf 10:225-247
Wieczorek MA, Phillips RJ (1999) Lunar multiring basins and the cratering process. Icarus 139: 246–259
Wieczorek MA, Zuber MT (2001) A Serenitatis origin for the Imbrian grooves and South Pole-Aitken thorium anomaly. J Geophys Res 106:27,853-27,864
Weiss BP, Kirschvink JL, Baudenbacher FJ, Vali H, Peters NT, Macdonald FA, Wilkswo JP (2000) A low temperature transfer of ALH 84001 from Mars to Earth. Science 290:791-795
Whitehead J, Grieve RAF, Spray J (2002) Mineralogy and petrology of melt rocks from the Popigai impact structure, Russia. Meteorit Planet Sci 37:623-648
Wilhelms DE (1980) Stratigraphy of part of the lunar near side. USGS Professional Paper 1046-A A1-A71
Wilhelms DE (1984) The Moon. *In*: The Geology of the Terrestrial Planets. NASA SP-469:107-205
Wilhelms DE, McCauley JF, Trask NJ (1987) The Geologic History of the Moon. US Geol Survey Prof Paper 1348
Williams KK, Zuber MT (1998) Measurement and analysis of lunar basin depths from Clementine altimetry. Icarus 131:107-122
Wolfe EW, Lucchitta BK, Reed VS, Ulrich GE, Sanchez AG (1975) Geology of the Taurus-Littrow valley floor. Proc Lunar Sci Conf 6th, Pergamon Press, p. 2463-2482.
Wolfe EW, Bailey NG, Lucchitta BK, Muehlberger WR, Scott DH, Sutton RL, Wilshire HG (1981) The geologic investigation of the Taurus-Littrow valley Apollo 17 landing site. USGS Professional Paper 1080
Wünnemann K, Ivanov BA (2003) Numerical modelling of the impact crater depth–diameter dependence in an acoustically fluidized target. Planet Space Sci 51:831-845
Wood CA, Andersson L (1978) New morphometric data for fresh lunar craters. Proc Lunar Planet Sci Conf 9th, Pergamon Press, p 3669-3689
Xie X, Chen M, Dai C, El Goresy A, Gillet P (2001) A comparative study of naturally and experimentally shocked chondrites. Earth Planet Sci Lett 187:345-356
Zahnle K, Mac Low M-M (1994) The collision of Jupiter and Comet Shoemaker-Levy 9. Icarus 108:1-17
Zukas JA (2004) Introduction to Hydrocodes. Elsevier